Using Finite Element Modeling to Gain Insights into the Mechanics of Wound Healing in *Drosophila*

by

Steven Kim

A thesis
presented to the University of Waterloo
in fulfillment of the
thesis requirement for the degree of
Master of Applied Science
in
Civil Engineering

Waterloo, Ontario, Canada, 2013

I hereby declare that I am the sole author of this thesis. This is a true copy of the thesis, including any required final revisions, as accepted by my examiners.

I understand that my thesis may be made electronically available to the public.

Steven Kim

Abstract

Although it is not difficult to observe the healing of induced wounds in animal embryos, mapping the forces that drive lesion closure has proved challenging. Laser microsurgery, Atomic Force Microscopy (AFM) and other techniques can provide local information at fixed times, but all are invasive and some disrupt further development. Video Force Microscopy (VFM) has been able to map driving forces during ventral furrow formation in *Drosophila* (fruit fly), but challenges arose when it was applied under the assumption that the only driving forces are intracellular pressures and forces (including purse string action) along cell edges. Other possible forces of relevance include far-field stresses and in-plane cellular contractions. Mapping the forces that drive wound closure is an important problem, and so far it has remained unsolved.

To investigate the process of dorsal closure, this study used a cell-based finite element (FE) model to identify the mechanical signatures of a wide variety of possible driving forces. Geometric parameters were developed to characterize the associated cell shapes and tissue motions and to quantitatively compare FE simulations with each other and with experimental data. It was discovered that edge tensions and pressures were not sufficient to drive wound healing. Wound healing can only be achieved when far-field boundary motions, edge tensions and apical area tensions act together.

This thesis shows that a suitable FE model can provide information about the forces that drive wound healing, and its simulations take us one step closer to understanding the mechanics of wound healing. It also contributes to our general understanding of the forces that drive morphogenetic movements and ultimately helps us to better understand cell-based processes important for human quality of life.

Acknowledgements

First and foremost, I would like to thank my supervisor, Prof. G. Wayne Brodland, who has tirelessly been supportive from the start to the end, and without his expertise, would have not been able to reach completion. During the years I was under his supervision, I have learned and been inspired by his ability and wisdom to approach and solve a wide range of problems.

I would also like to thank my colleagues, Ben Brodland, Ahmad Ehsandar, and Caleb Horst, for helping me whenever I was in need and making my experience here enjoyable. Special thanks to my colleague Jim Veldhuis, who has provided outstanding technical support and helped me become a better Squash player.

Thanks to our research collaborator Prof. M. Shane Hutson for all the experimental data that he has provided along with his various insights into the problem.

Sincere thanks to my family and friends who have supported me all my life through prayer and encouragement. You guys have been a blessing in my life, especially the Lim family. Taein, you have been my friend and brother since childhood, thanks you for everything. To my sisters Ruth and Esther, thanks for your unconditional love and support.

Finally, thanks to the people who took time to read and edit my treatise: Jessica Jong, Hannah Yoo, Caroline Cho, Le-Yen Lam, Prof. Adil Al-Mayah, and of course, Prof. Brodland.

This work was funded in part by a NSERC and NIH grant to Prof. Brodland.

Table of Contents

List of Figures

List of Tables

Chapter 1
Introduction

One of the most fascinating phenomena in nature is the ability of biological systems to heal and recover from injuries that range from the cellular to skeletal scale. The ability to heal is crucial to survival. In an epithelial injury, the cells surrounding the wound undergo significant changes and rearrangements so as to reseal the damaged area. Much research has been done during the last several decades to understand the morphogenetic movements of the wound healing processes in different animals and insects (Brock et al., 1996; Galko & Krasnow, 2004; Hutson et al., 2003; Jacinto & Martin, 2001; Kiehart et al., 2000; Ramet et al., 2002; Wang et al., 2009; Wood et al., 2002). However, identifying the forces that drive lesion closure has proved to be a challenge.

For many years, researchers have been trying to map the forces that drive morphogenetic movements such as wound healing and embryogenesis. Although progress has been made, biological tissues are fragile and the forces generated are of the order of micro- or pico-Newtons, and physical measurements are difficult to make.

One technique that can be used to determine the forces that drive wound healing involves ablating parts of one or more cells using a laser micro-scalpel (Hutson et al., 2003; Kiehart et al., 2000). Laser microsurgery has been refined over many years to the point where a single cell, membrane, or even a single cytoskeletal component can be ablated in a controlled manner. The Hutson group from Vanderbilt University in Tennessee, who is one of our collaborators, uses this technique to study morphogenetic movements in *Drosophila* (fruit fly) embryos and the experimental data presented here are from his lab. Although advancements were made in understanding morphogenetic movements through this technique, it has a number of drawbacks. When a laser insertion is made, it causes significant damage to the cells. The biological system is changed, and so stress from recoil information can be obtained only at a single location and instant in time. Despite the drawback to this technique, measurements acquired using this technique in conjunction with biological morphology studies have led researches to identify a number of possible driving forces responsible for wound healing including actomyosin cables, lamellipodia, area contractions, and purse string tensions (Jacinto & Martin, 2001; Martin & Lewis, 1992; Ramet et al., 2002; Wood et al., 2002).

An important question to ask regarding this problem is: “Why is it important to be able to map these forces?” A good answer is that it will provide a deeper understanding of how tissues move and rearrange. At a fundamental level, it offers the possibility to manipulate motion through controlling the driving forces at its source. Whether the motion is mechanical or chemically induced, having the ability to control the driving factors will allow the manipulation of cell movements for experimental or therapeutic ends.

Likewise, through genetic engineering, certain genes may be enhanced or suppressed to control the cell structures and proteins that contribute to morphogenetic movements. In the case of embryogenesis, there are many birth defects that arise from incomplete or incorrect morphogenetic movements. Common birth defects such as spina bifida and cleft palate arise from incomplete morphogenetic movements. For example, the failure in the closure of the neural tube will result in spina bifida. This birth defect could be prevented if the driving forces that cause the neural tube to close functioned normally (Brodland et al., 2010a; Stark, 1977). A better understanding of the forces that drive wound healing, in particular, could help improve the recovery of patients suffering from injuries by shortening recovery time and preventing scarring. Thus, information about driving forces could advance the biomedical industry and enhance patient quality of life.

Mapping the forces of morphogenetic movement was an unsolved problem until a biomechanical research group at the University of Waterloo under the supervision of Professor Wayne Brodland developed a technique called Video Force Microscopy (VFM) (Cranston, 2009), the first technique able to map the forces that drive morphogenetic movements, VFM is a computational method that uses engineering principles, Finite Element Modeling (FEM) and inverse methods. It is common in FEM to consider the force as an in input and the displacement as an output. In contrast, VFM uses the displacement history as its input and calculates the driving forces responsible for the observed motions as the output. Here in our lab, cell-based Finite Element (FE) models have been developed and are used to track changes in motion, thereby computing the edge tensions and pressures in the cells that induce shape changes and rearrangements of cells (Brodland, 2002; Brodland et al., 2007). This technique not only overcomes the drawbacks of the laser insertion technique, but also advances the way morphogenetic movements are studied. VFM was used to map the forces that drive ventral furrow formation in *Drosophila melanogaster* embryos (Brodland et al., 2010b; Conte et al., 2012).

When a version of VFM in which edge tensions and pressures alone were assumed to act was first applied to wound healing, the edge tensions and pressures results were not convincing. Could other mechanical forces be at work? The objective of this study is to determine the driving forces responsible for wound healing in *Drosophila* embryos during the dorsal closure stage through finite element modeling. A wide range of possible driving forces will be considered and mechanical and geometric tools used to assess the computational results.

Chapter 2
Background

This chapter provides background information on the biology of wound healing and morphogenesis in *Drosophila* embryos. It also provides background information relevant to the modeling of biological cells, including forward modeling and simulations, inversion techniques, and biological experiments.

2.1 Wound Healing

2.1.1 Uncovering the Secrets of Wound Healing

For many years, researchers have been trying to answer the question, "How does wound healing occur?" and that question has remained largely unanswered. When a wound is introduced, cells rearrange and reduce the wound hole until it is completely sealed. Young infants are prone to recover from a wound much faster and in completion than full grown adults (Redd et al., 2004). Continual research in the therapeutic work has been progressing to improve healing for patients recovering from injuries. There are many theories suggesting how cells rearrange and wound healing may occur but it has clearly been a challenge to pin point its driving forces and how this process occurs (Brodland, 2002; Harris, 1976; Redd et al., 2004). One of the challenges is the lack of experimental techniques for studying lesion closure. In many cases, studies are conducted on insects and small mammals, and they may not necessarily reflect the morphogenetic response of humans. Although there are many challenges, researchers have managed to advance our understanding in wound healing and morphogenetic movements (Hutson et al., 2003; Jacinto & Martin, 2001; Kiehart et al., 2000; Wood et al., 2002).

2.1.2 Wound Healing and the Drosophila Embryo

Drosophila (fruit fly) embryos are widely used for studying wound healing and morphogenetic movements (Belacortu & Paricio, 2011; Galko & Krasnow, 2004). A *Drosophila* has a short cycle time from the formation of an egg to becoming a full grown fruit fly and is easily accessible as it grows. Dorsal closure, an important process in embryo development, has been an excellent model for studying healing and cell movements. Dorsal closure can be considered the last process in morphogenetic development in a *Drosophila* embryo (Campos-Ortéga & Hartenstein, 1997). During this process, the epidermal cells

overlap the amnioserosa cells until the two leading edges meet. Figure 2.1 shows the 3 step process of dorsal closure.

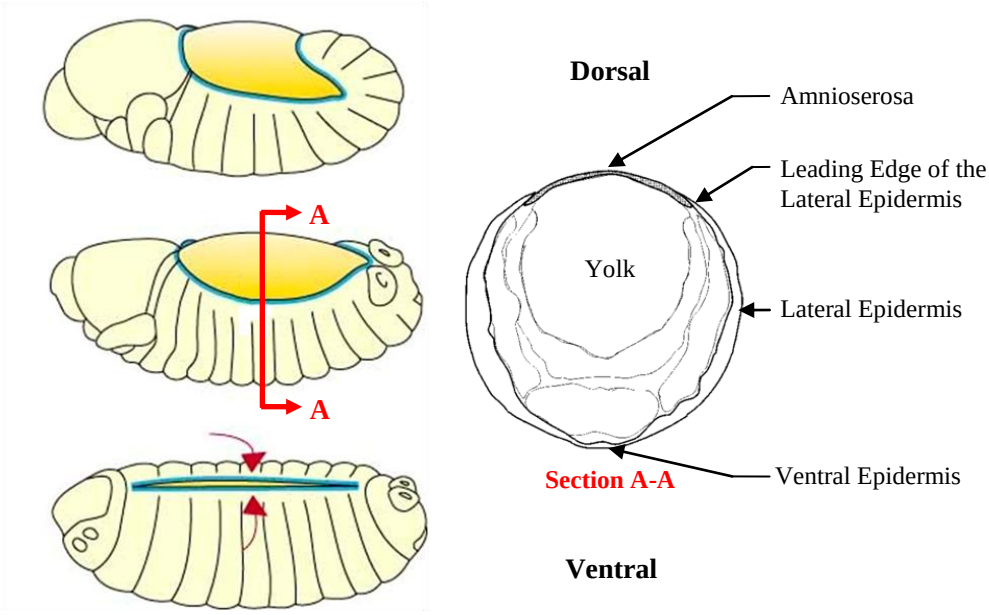

Figure 2.1 – *Drosophila* embryo. The figure on the left shows the process through which dorsal closure occurs. The figure on the right illustrates a typical cross section. Image courtesy of Dr Martinez-Arias, Cambridge, UK. (Kiehart et al., 2000)

Intensive studies have been conducted to understand the biomechanics of dorsal closure. One of the most common techniques used to study this phenomenon, besides genetic perturbations, was through the use of micro laser surgery. Micro laser surgery has been refined over many years to the point where a single cell, membrane, or even a single cytoskeletal component can be ablated in a controlled manner. By ablating a cell edge, the stress at that location may be acquired through relating material properties and recoiling of neighboring cells.

Using this technique, it was shown that there are four major biological processes that may be responsible for dorsal closure and are shown in Figure 2.2 (Hutson et al., 2003; Kiehart et al., 2000; Peralta et al., 2008).

1. Contractile force of the actomyosin-rich purse string
2. Contractile force of the cortical actomyosin networks of the amnioserosa cells
3. Resistant forces that arise from stretching of the lateral epidermis
4. Zipping at each canthus

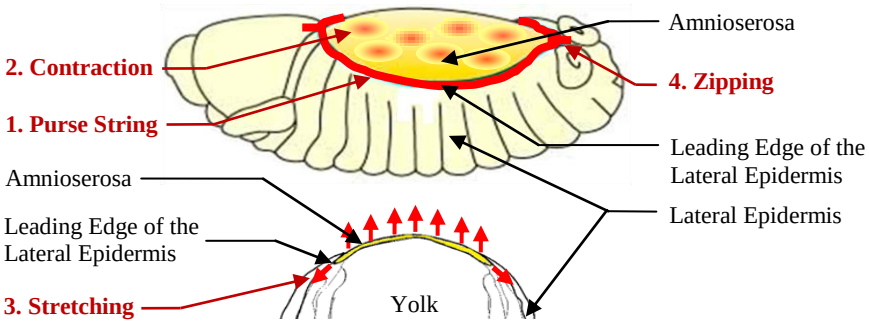

Figure 2.2 – Forces acting on a *Drosophila* embryo

While other forces contribute to dorsal closure, the stretching of the lateral epidermis resists dorsal closure and is counter balanced with isotropic tensions acting on the amnioserosa. Laser perturbations introduce only a small delay in the closing process of the amnioserosa while the presence of amnioserosa is crucial in closure and zipping of the epidermis (Hutson et al., 2003; Scuderi & Letsou, 2005).

Although *Drosophila* embryos are an excellent model for analyzing wound healing, traditional laser ablation techniques have been shown to have challenges of their own. Traditional laser micro surgery cause significant damage to the cells and provide stress data at a single location and instance in time. Despite the drawbacks of micro laser surgery technique, studies have shown that lesion closure may still be achieved through actin cable and dynamic protrusions (Anon et al., 2012; Wood et al., 2002).

Jacinto et al. (2002) use micro laser ablation techniques to study the wound healing process in *Drosophila* embryos during dorsal closure. They noted that wound closure is achieved by changes in cell shape and rearrangements while actin cable and dynamic protrusions are the driving forces (Jacinto et al., 2002). Previous study have shown that the protein *GTPases Rho* is responsible for the formation of actin cable and *Cdc42* is responsible for the formation of filopodia (Wood et al., 2002). Through genetic perturbations of *GTPases Rho* and *Cdc42*, it was suggested that at the wound sight, actin cable formed around the perimeter of the wound to act as a purse string, causing the hole to close in. *Rho* mutant embryos were not able to assemble actin cable at the site of the wound, but were still able to close the wound, suggesting that purse string contraction was not the only driving force in wound closure. When *Cdc42* was modulated, wound closure was still achieved however, it took twice as long and the hole was not fully repaired. The modulation of *Cdc42* suggested that dynamic filopodial/lamellipodial protrusions were responsible to knitting the wound while other factors could have been responsible for lesion closure (Jacinto et al., 2002).

Interestingly enough, lesion closure was achieved with modulating either actin cable or dynamic protrusion, but there still remained a possibility that neither may have been the driving force to which wound closure was achieved. Whether the conclusions obtained through various experiments may be correct, there is an emerging need for studying wound closure using non-traditional techniques to provide a different perspective and insight to this problem. Furthermore, understanding these changes in shape and healing abilities during embryogenesis is significant into providing insight to healthy and normal embryonic development.

2.2 Tissue Mechanics Modeling and Experimentation

The use of computer modeling has been increasing, especially in the bioengineering field. In the past, computer aided design (CAD) and computer simulations have been carried out on mechanical systems and materials but in recent years, researchers have been utilizing computer modeling and simulations in the bioengineering field. Many discoveries made in cell mechanics and morphogenesis would not have possible without the use of computer technology (Brodland et al., 2010a; Brodland et al., 2010b; Chen & Brodland, 2008). Before we apply modeling techniques to embryonic development and wound healing, cell modeling and existing models will be introduced.

2.2.1 The Anatomy of a Cell

A cell can be considered to be the fundamental building block in all biological beings. There are many different components that form the cell. Figure 2.3 is an example of a cell model showing a few of its main parts. The cell membrane is a flexible bilayer composed primarily of phospholipids. At the surface of the cell membrane, there are various molecules that control transportation through the membrane while other molecules are responsible for cell adhesion. The cell's membrane is known to be under tension.

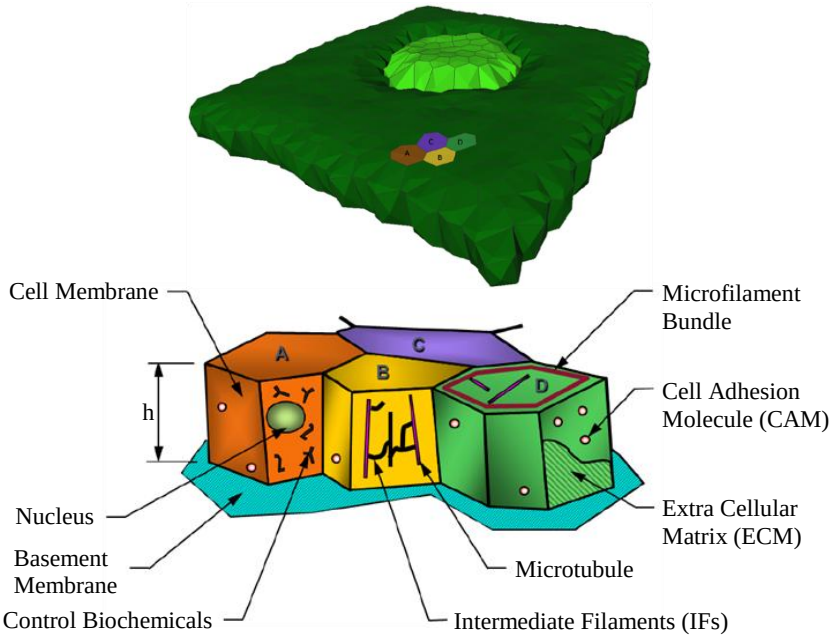

Figure 2.3 – Cell structure and components

Inside the membrane, are the cytoplasm and cytoskeleton, where the cytoplasm is a clear gel containing various proteins and the cytoskeleton gives structure to the cells (Ethier & Simmons, 2007). The cytoskeleton is composed of microfilaments, intermediate filaments and microtubules (Cowin &

Doty, 2006). Microfilaments are flexible and relatively strong, which give structural integrity to the cell while resisting buckling, and are composed of actin. Intermediate filaments are protein fibers that brace the microfilaments and microtubules, giving mechanical strength and also supporting organelles within the cell. The largest cytoskeleton structures are microtubules, which are hollow cylindrical tubes that aid in the transportation of nutrients and play a key role in mitosis (cell division). At the core of the cell is the nucleus. The nucleus contains DNA, RNA, and chromosomes and it controls cell activity by regulating gene expression.

2.2.2 Quantification of Cell Properties

There are many reasons to why it is necessary to understand the mechanical properties of the cells. Designing biocompatible materials, modeling biological tissues, tissue engineering and many other applications, all depend on understanding the mechanical behavior of cells and tissue. However, taking measurements on cells is not an easy task because the forces generated are of the order of micro- or pico-Newtons. Despite the difficulty of the protocol, researchers have managed to develop techniques to obtain the mechanical properties of cells.

One of the techniques used to measure cell properties is micropipette aspiration (Ethier & Simmons, 2007; Mitchison & Swann, 1954). This is one of the first devices used to measure mechanical properties of cells. A glass pipette is placed on the surface of the tissue and a negative pressure is created, allowing the cell to bulge into the glass pipette as shown in Figure 2.4. From the deformed geometry of the cell, the mechanical properties of the cell can be obtained based on the applied pressure. Laplace's Law can also be used to relate the pressure, membrane curvature and tension by Eq. (2.1), where γ is the surface tension, ΔP is the pressure gradient and ρ is the radius of curvature (Morris & Homann, 2001).

$$\gamma = \frac{\Delta P \times \rho}{2} \tag{2.1}$$

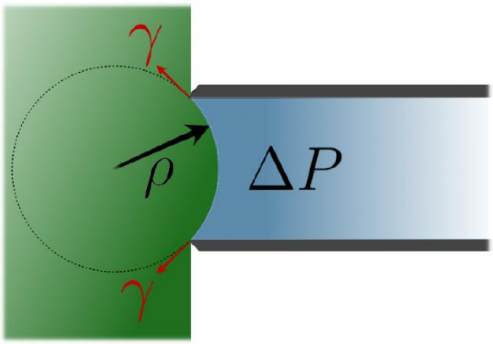

Figure 2.4 – Micropipette aspiration (Cranston, 2009)

In addition to the cell edge tensions, the adhesive strength of the cell can be measured using a second pipette. As the first pipette holds the cell in place the second pipette is used to pull them apart.

Atomic force microscopy (AFM) is another method used to obtain cell properties. In this method, a flexible beam with a probe attached to its tip is used to deform the surface of the cell. Using a laser, the position of the beam is determined and by approximating the beam as a linear spring, the force is calculated using Eq. (2.2), where E is the stiffness of the cell, α is the half-angle of the conical probe tip, F is the applied force, δ is the displacement, and v is the Poisson's ratio (Ethier & Simmons, 2007).

$$\delta^2 = \frac{\pi}{2}\frac{F\left(1-\nu^2\right)}{E\tan\alpha} \tag{2.2}$$

Another method used for measuring properties of cell is optical tweezers. Optical tweezers use a pair of laser beams to manipulate a bead that is manually inserted inside the cell. Through the exploitation of the photons' momentum, the bead can be displaced in a controlled manner. Beads may also be manipulated using magnetism rather than laser beams. In either case, the force on the bead is calculated using empirical calibration because it cannot be calculated directly. By using Eq. (2.3), the bead is calibrated in a known medium and the forces are calculated using Stoke's Law, where F is the drag force, μ is the fluid viscosity, r is the radius of the bead, and v is the velocity (Dai et al., 1997).

$$F = 6\pi\mu rv \tag{2.3}$$

In most cases, the cell of interest needs to be in isolation to conduct these tests due to the nature of the test devices and method protocol. These tests are not only invasive, but would be difficult to conduct on biological tissues that are in a dynamic environment such as morphogenesis or wound healing. Although it may be difficult to use these methods for our purpose and study, the results obtained from these experiments are essential to tissue modeling and finite element models that exist today.

2.2.3 Tissue Rearrangement and Differentiation

Biological cells have the ability to rearrange and differentiate during embryonic development, morphogenetic processes, cell sorting, and wound healing. Although chemical or genetics may trigger the outcome of the cells' movement, studies have shown that cell sorting and differentiation are essentially mechanical (Arrkas, 1994; Beloussov, 1998; Cowin & Doty, 2006; Nuri Akkaş, 1994).

Wilson (1907) was the first person to observe cell sorting in multicellular organisms (Arrkas, 1994). In the case of embryonic vertebrates, it was determined that cells dissociated and mixed randomly, suggesting that cells themselves produced the driving force necessary to differentiate and rearrange (Wilson, 1907). Later on, morphogenetic experiments were conducted with different types of cells by Townes and Holtfreter (1955). They observed that the grouping of cells tended to have the same final configuration despite different starting configurations (Townes & Holtfreter, 1955). They suggested that cell engulfment, invagination and sorting had the same or similar driving mechanism (Arrkas, 1994). Besides the scientist mentioned previously, extensive research has been conducted in cell sorting and differentiation and all evidence suggest that it is a self driven and mechanical in nature (Steinberg, 1962; Steinberg, 1970).

There have been two hypotheses to describe how cellular self-rearrangements are driven: the Streingerg's Differential Adhesion Hypothesis (DAH) and Brodland's Differential Interfacial Tension Hypothesis (DITH) (Brodland, 2002; Harris, 1976). DAH suggests that cell sorting behaves like immiscible liquids. In other words, depending on the adhesion molecular force, cells will engulf or be engulfed by cells that have different adhesion molecular forces (Steinberg, 1970). However, the DAH theory has been deemed unviable in recent years. The DITH is an alternate theory that suggests that cell self-rearrangements are driven by differences in interfacial tensions (Arrkas, 1994; Brodland, 2002; Harris, 1976). The interfacial tensions are the consequence of membrane contraction, actin forces and adhesion systems.

If cells are in equilibrium, the interfacial tensions will determine the geometry of the triple junctions. In a perfectly annealed cell patch, the triple junction of three cells will form 120 degrees angle with one another if all boundaries carry the same effective tension. Studies have suggested that the principle stress direction is correlated with cell geometry (Beloussov, 1998; Goodwin & Trainor, 1985; Hutson et al., 2009; Hutson et al., 2009; Odell et al., 1981; Steinberg, 1978; Thompson, 1942). When analyzing tissue mechanics, many three dimensional (3D) problems can be simplified into a two dimensional (2D) problem because generally speaking, tissues are composed of planar aggregates and 2D models have been shown to be sufficient for these problems (Brodland et al., 2006).

2.3 Finite Element Modeling

As the research field of tissue modeling and testing advanced, mathematical models of cell behavior using a one dimensional (1D) equivalent mechanical circuit were developed. The 1D cell models were based on viscoelastic material comprised of Maxwell, Kelvin and Maxwell-Kelvin models (Ethier & Simmons, 2007). These models were later used in conjunction with the DITH to develop 2D cell models. Other models include tensegrity cell structure, lattice, and cellular automata model which were essential to the development of the finite element (FE) models of cells and tissues (Coughlin & Stamenovic, 1997; Ingber, 1993; Ingber, 1997). Computational models of cells were developed as early as 1981 by Odell et al. In more recent years, Davidson et al. (1995) developed a FE model to simulate the gastrulation process in sea urchin. Through finite element modeling and experiments, Davidson was able to test the feasibility of several potential driving mechanisms (Davidson et al., 1999). In 2006, a cell-based constitutive model was developed by Brodland et al. which related tissue deformations, in-plane stresses, topological evolution of cellular fabric, mitosis, and cell rearrangement. This was the first of its kind for studying embryonic development using finite element modeling. Other finite element models were developed by Brodland et al. and provided a new avenue in studying morphogenesis and embryonic development (Brodland & Chen, 2000; Brodland et al., 2007; Chen & Brodland, 2008; Clausi & Brodland, 1993; Hutson et al., 2008).

2.3.1 Finite Element Model

A finite element model, called *Simba*, was used as the basis of our finite element analysis. *Simba* is a custom written *C++* simulator developed in our lab over the last 20 years. Similar to other finite element analysis software, an input geometry is read by the code and the algorithm calculates resulting displacements from the applied forces, mechanical properties, and constraints over a series of successive time steps. The details of the finite element model and analysis are explained in the following subsections. Figure 2.5 shows an example of a 2D finite element model of a collection of biological cells. The cells appear as contiguous polygons which are assumed to be connected with each other at their vertices or nodes. Their mechanical properties derive from their in-plane areas and their edges.

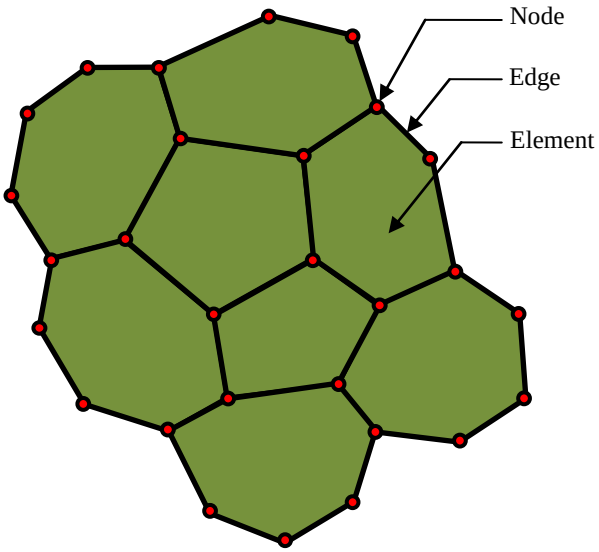

Figure 2.5 – Cell 2D finite element model

Nodes:

In a 2D model each node has two degrees of freedom (DOF), with displacement in the x- and y-directions, only. In most cases, nodes form a double or triple junction, where two or three cells meet. However, it is possible for a node to form a quad junction which commonly occurs during cell neighbor changes. These neighbor changes are frequent events and have an important role in morphogenesis and cell rearrangement. A neighbor change occurs in three major steps, as demonstrated in Figure 2.6. Two cells, labeled B and D, begin with a short horizontal contacting edge. As this edge shortens to zero length and a new vertical edge forms, cells B and D become separated and cells A and C come into contact. Although neighbor exchanges are a common occurrence in most tissues, they are rare in the amnioserosa during dorsal closure.

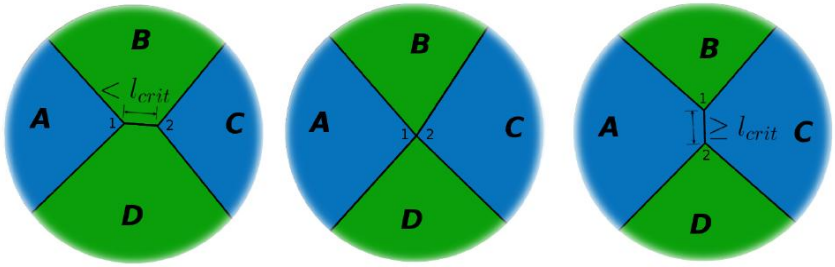

Figure 2.6 – Neighbour change (Cranston, 2009)

Edges:

Edges are straight line segments that represent the interface between adjacent cells or a cell and the surrounding medium, and they always connect two nodes. According to the DITH, a net tension force acts along each edge, a force which arises from various sub-cellular components. The net force that arises from intra-cellular forces can be represented as γ_{AB} for an edge that is between cell A and B. Figure 2.7 depicts the structural components that contribute to the net interfacial tension in Eq. (2.4) (Brodland & Chen, 2000).

$$\gamma_{AB} = F_A^{Cyto} + F_B^{Cyto} + F_A^{Mem} + F_B^{Mem} - F_{AB}^{Adh} + F_{AB}^{Other} \tag{2.4}$$

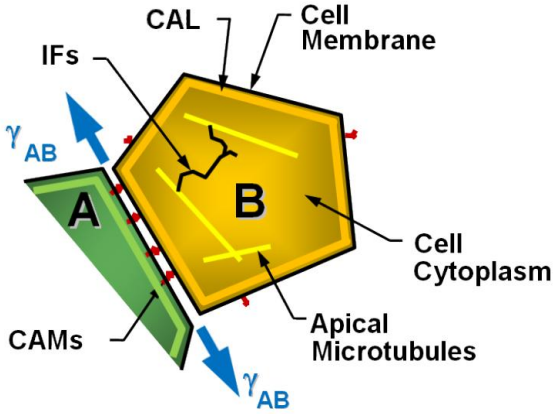

Figure 2.7 – Contribution to interfacial tensions (Cranston, 2009)

The term F_A^{Cyto} represents the forces that arise from the cytoplasm and its embedded intermediate filaments. The term F_A^{Mem} represents the membrane tension acting along the particular interface and also includes the tensions arising from the cortical actin layer (CAL). Forces from cell adhesion molecules (CAM) are represented by F_A^{Adh} and they lower the interfacial tension. Other forces, which have not been mentioned above, may contribute to the net interfacial tensions acting along the cell edge and is represented by F_A^{Other} .

Elements:

The cytoplasm in biological cells can be modeled as a massless, viscous, incompressible fluid since strain rates are typically in the order of $10^{-6}/s$ during tissue remodeling (Clausi & Brodland, 1993; Hutson et al., 2009). This allows the cells to be modeled as a viscous material using dashpots. Dashpots are models that resist motion where its resulting forces are dependent on the velocity. There are three different vicous models available in the Cell2D element class, viscous triangles, radial/circumferential dashpots, and orthogonal dashpots (Figure 2.8).

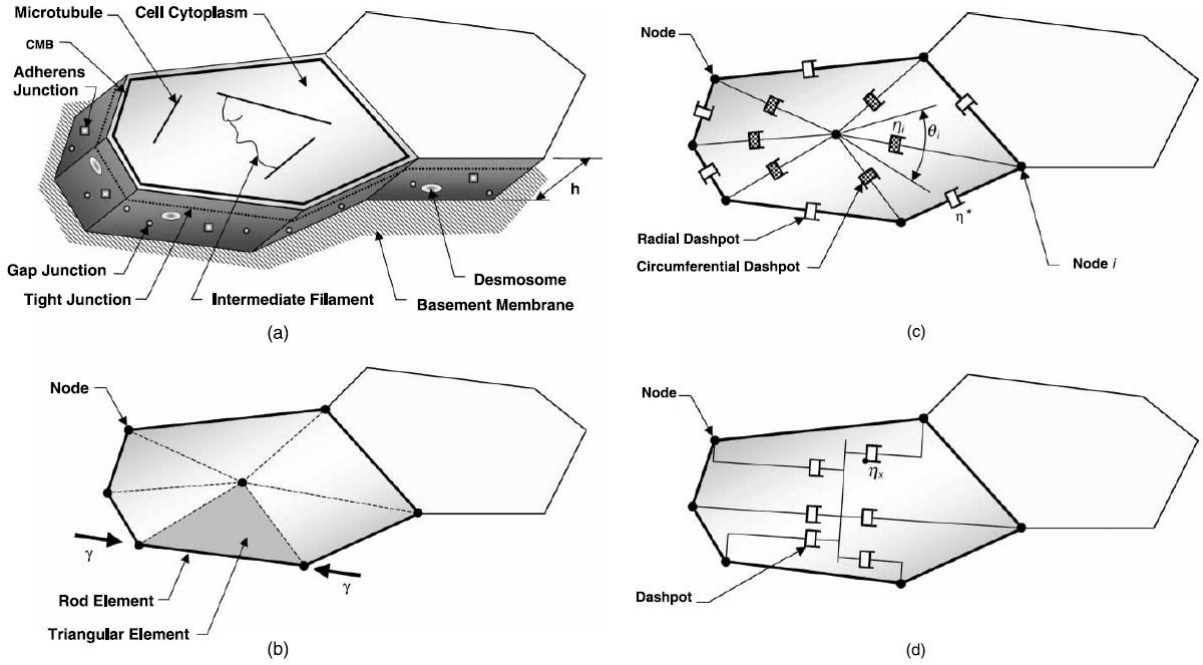

Figure 2.8 – (a) The components in cells. (b) A viscous triangle viscous model. (c) Radial and circumferential dashpot model. (d) Orthogonal dashpot model. (Brodland et al., 2007)

The viscous triangle model breaks a cell into multiple triangular elements with a center point. The radial/circumferential dashpot model has dashpots along the radial and circumferential direction. The orthogonal dashpot model allows each dashpot to be connected to one node and a common ground. Figure 2.8 (d) only displays the dashpots along the major axis for clarity whereas in the model, there are dashpots along the major and minor axis of the cell. A comparative study was conducted to analyze the different approaches to model cells and the orthogonal dashpot was deemed more viable (Brodland et al., 2007). As a result, the orthogonal dashpot model will be used for our study with the stiffness of the dashpot defined by Eq. (2.5) (Brodland et al., 2007).

$$\mu_A = \frac{4\,g\,\pi\mu\,hB}{nA} \tag{2.5}$$

where g is the form factor = 0.682, μ is the viscosity, n is the number of nodes in cell, h is the cell thickness, A and B are the major and minor (length) axes of the cells, respectively.

2.3.2 FE Model Solution

An object in motion can be governed by a general dynamics equation as shown in Eq. (2.6), where the first term accounts for the inertia forces, the second term accounts for the viscous forces, and the third term accounts for the elastic forces. In the case of morphogenesis and embryo development, the inertia forces may be ignored because the scale and accelerations are small. As a result, the general equation of motion can be reduced to a first order equation. In the case of biological cells, cells have a viscous behavior rather than an elastic behavior and this allows the elastic forces to be neglected. Thus, the general equation of motion is reduced to Eq. (2.7), where C is the damping matrix, Δt is the time increment, u is the displacement, and F is the equivalent joint force vector.

$$M\ddot{u} + C\dot{u} + Ku = f_m + f_c + f_k = F \tag{2.6}$$

$$C\left(\frac{1}{\Delta t}u\right) = F \tag{2.7}$$

The nodal displacements are solved for a given increment of time from the simplified equation of the general equation of motion. The problem is geometrically nonlinear and is solved incrementally. The resulting solution gives vectors of nodal displacements and Lagrange multiplier values for each time step.

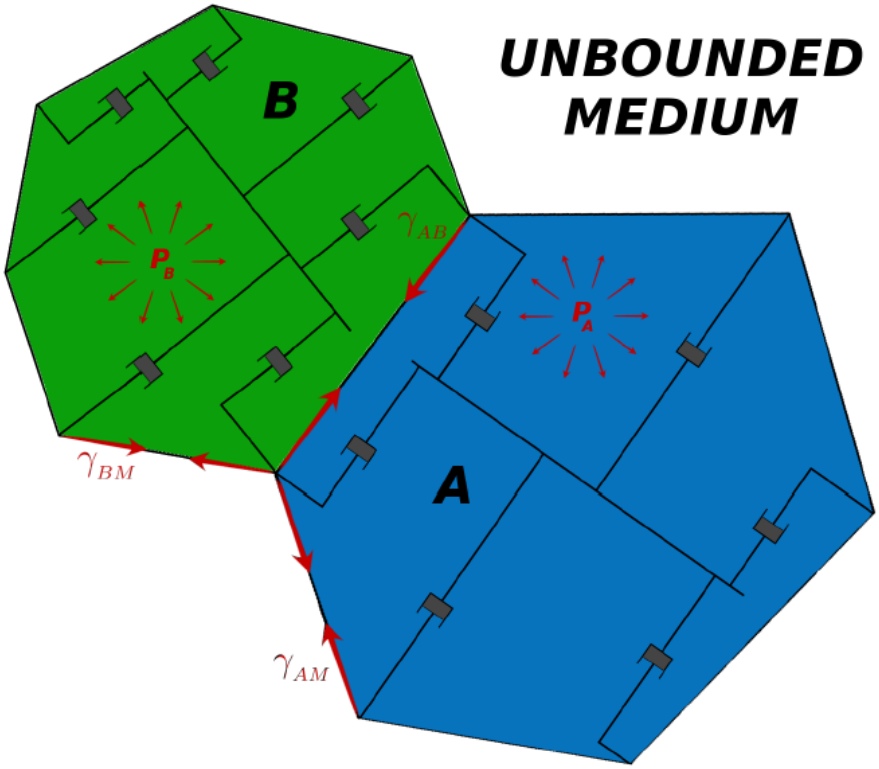

Figure 2.9 – The differential tension finite element model (Cranston, 2009)

2.4 VFM Inverse Approach

In traditional finite element modeling, the driving forces are applied and the model outputs the displacements. Here, we use an inverse formulation in which driving forces are determined from tissue displacements. The first generation of this inverse technique was developed by P. Graham Cranston in 2009 as part of his thesis (Cranston, 2009). This software package was called *Scar*.

2.4.1 Inverting the FE Model

In forward FE methods, Eq. (2.7) is used to solve for the nodal displacements. However, in VFM, Eq. (2.7) is first solved for the forces at each node and then for the edge tensions and pressures, as described below. In any FE model, boundary conditions and constraints must be specified. Without proper constraints and conditions, the system will not be statically determinant (Lay, 2003). In the model demonstrated in Figure 2.10, the cell patch is constrained by a pin joint at one node and a spring joint at another. The pin joint constrains two DOF while the spring, assigned a low stiffness, adds a third. Nodal forces are assumed to arise only from viscous forces, pressures and cell edge tensions.

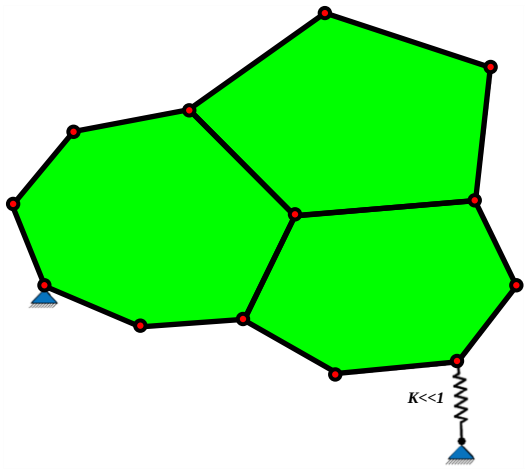

Figure 2.10 – Constraining the input model for inversion (Cranston, 2009)

With the system well constrained, the nodal forces can be calculated using Eq. (2.7). The resulting nodal forces can be decomposed to forces generated from subcellular structures through the geometric matrix, a matrix that relates nodal forces to subcellular forces based on the cell's structure.

Force Generators:

Some of the subcellular forces acting on a typical cell are shown in Figure 2.11. There are two forces that contribute to nodal forces, edge tensions and pressure forces. It is assumed that all edges are under tension

and is the case for node 26. The edge tensions surrounding node 26 are shown in red and it is assumed that the tensions differ in magnitude.

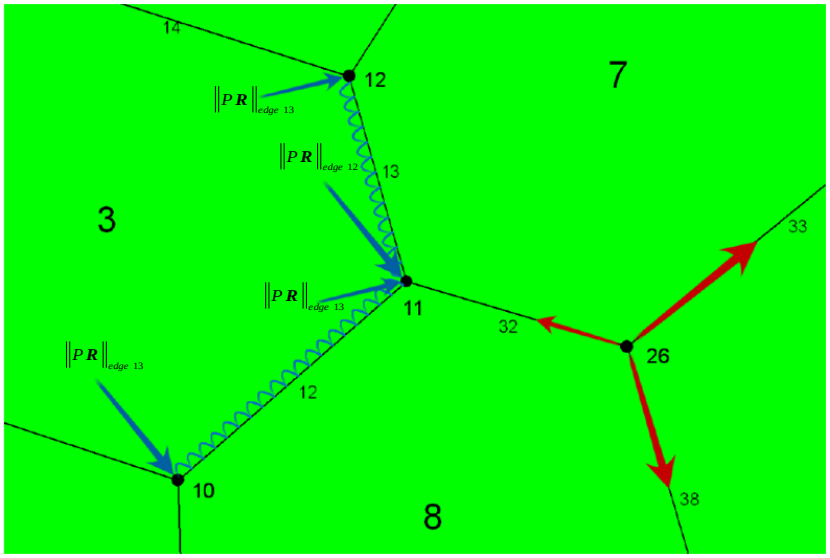

Figure 2.11 – Translation of forces acting on nodes (Cranston, 2009)

The nodal force contribution from the cell pressure is shown along edges 12 and 13. The pressure load acts normal to the surface and is modeled as a distributed load. The pressure load can arise from in-plane loads generated along the apical and basal membranes and volume constancy of the cell. The intracellular pressure is represented as a negative load. The distributed pressure load can be represented as two point load, equal in magnitude, acting on both ends perpendicular to the edge. The magnitude of these forces can be calculated from Eq. (2.8), where P is the pressure and l is the length of the edge.

$$\|P\,\boldsymbol{R}\| = \frac{Pl}{2} \tag{2.8}$$

Assembling the Geometric Matrix:

Equivalent joint loads are calculated using Eq. (2.9), where **G** is a geometric matrix, **F** is a vector of nodal forces, and **T** is a vector of unknown tensions and pressures. Details of the equations are given below, but briefly, the first term relates edge tensions to nodal forces and the second term relates pressures to nodal forces.

$$\mathbf{GT} = \mathbf{F} \tag{2.9}$$

$$[\mathbf{G}_T]\{\mathbf{T}_T\} + [\mathbf{G}_P]\{\mathbf{T}_P\} = [\mathbf{G}_T \mid \mathbf{G}_P]\left\{\begin{matrix}\mathbf{T}_T \\ \hline \mathbf{T}_P\end{matrix}\right\} = \mathbf{F} \tag{2.10}$$

Tensions:

The geometric matrix $\mathbf{G}_T$ relates the edge tension $\mathbf{T}_T$ to the forces exerted at the nodes on which they impinge. For a given edge (of length *l*), the componential forms of Δx and Δy for the x and y components of the edge are used, respectively. Figure 2.12 and Eq. (2.11) demonstrates how the edge tension geometric matrix is assembled from the associated components (direction cosines). For details, see Cranston (2009).

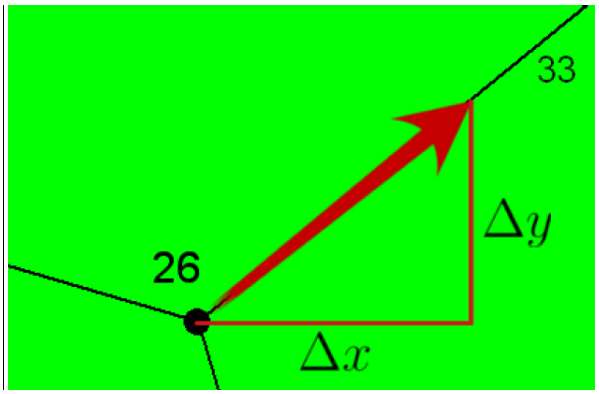

Figure 2.12 – Development of edge tension geometric matrix (Cranston, 2009)

$$\begin{bmatrix} G_{T_{1,1}} & \cdots & & \\ \vdots & \ddots & & \\ & & G_{T_{53,33}} = \Delta x / l & \\ & & G_{T_{54,33}} = \Delta y / l & \\ & & & \ddots \end{bmatrix} \begin{Bmatrix} \\ \vdots \\ T_{T_{33}} \\ \vdots \end{Bmatrix} = \begin{Bmatrix} \\ \vdots \\ F_{T_{53}} \\ F_{T_{54}} \\ \vdots \end{Bmatrix} \tag{2.11}$$

The rows of **GT** correspond to the degree of freedom (DOF) of the model and the columns to the edge tensions. In the example above, Node 26 corresponds to the 53rd and 54th DOF and the matrix shows how edge tension $T_{T_{33}}$ contributes to the calculated forces.

Pressures:

The geometric matrix $\mathbf{G}_P$ relates the pressure in a cell to the forces exerted at its perimeter nodes. For each side, the effect is equivalent to a distributed load normal to the edge. To represent the force in Cartesian coordinates, binormal vectors are employed as shown in Figure 2.13.

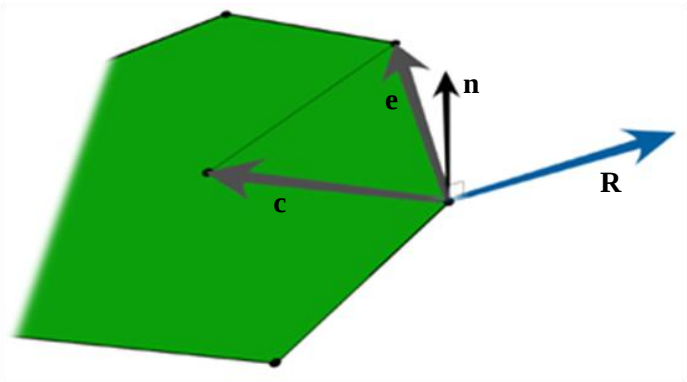

Figure 2.13 – Development of pressure geometric matrix (Cranston, 2009)

Two vectors are defined where vector $\boldsymbol{c}$ extends from the node to the center of the cell, and vector $\boldsymbol{e}$ extends along the edge on which the pressure is acting. By taking the cross product of the two vectors in Eq. (2.12), a new vector $\boldsymbol{n}$ (normal to the cell plane) is defined. Taking the second cross product with vector $\boldsymbol{e}$ and vector $\boldsymbol{n}$ in Eq. (2.13), vector $\boldsymbol{R}'$ pointing perpendicular to the cell edge is created. Vector $\boldsymbol{R}'$ is then scaled to give $\boldsymbol{R}$, such that the resultant force on the node is $_{P}\boldsymbol{R}$ determined from Eq. (2.8). The resulting $\boldsymbol{R}$ is determined from Eq. (2.14), where l is the length of the edge the pressure is being applied.

$$\boldsymbol{n} = \boldsymbol{e} \times \boldsymbol{c} \tag{2.12}$$

$$\boldsymbol{R}' = \boldsymbol{e} \times \boldsymbol{n} \tag{2.13}$$

$$\boldsymbol{R} = \frac{l}{2} \frac{\boldsymbol{e} \times (\boldsymbol{e} \times \boldsymbol{c})}{\left\| \boldsymbol{e} \times (\boldsymbol{e} \times \boldsymbol{c}) \right\|} \tag{2.14}$$

The resultant vector $\boldsymbol{R}$ is defined in $\Re^3$, having 3 components x, y, and z. However, the two dimensional nature of the problem allows the z-component to always be zero; while the x and y components are incorporated in the $\mathbf{G}_P$ geometric matrix. Equation 2.15 demonstrates the placement of these components for Cell 3 at Node 11 from Figure 2.11. The $G_{P_{23,3}}$ has two terms, $R_x^{(12)}$ and $R_x^{(13)}$ where the symbol R_x refers to the x component of vector $\boldsymbol{R}$ and includes the contribution of the distributed pressure from edge 12 and 13.

$$\begin{bmatrix} G_{P_{1,1}} & \cdots & & \\ \vdots & \ddots & & \\ & & G_{P_{23,3}} = R_x^{(12)} + R_x^{(13)} & \\ & & G_{P_{24,3}} = R_y^{(12)} + R_y^{(13)} & \\ & & & \ddots \end{bmatrix} \begin{Bmatrix} T_{P_1} \\ \vdots \\ T_{P_3} \\ \vdots \end{Bmatrix} = \begin{Bmatrix} F_{P_1} \\ \vdots \\ F_{P_{23}} \\ F_{P_{24}} \\ \vdots \end{Bmatrix} \tag{2.15}$$

Solution:

With the tension and pressure geometric matrix assembled, the unknown edge tensions and pressures in the system of equations can be solved by equating Eq. (2.7) and Eq. (2.9). Generally speaking, a system of equations can either be underdetermined, overdetermined, or hold a unique solution. If a system is underdetermined, it will have an infinite number of solutions whereas, an overdetermined system will have no unique solution. A patch of cells surrounded by medium generally has more equations than unknowns and tends to be an overdetermined system.

There are many different methods to find an approximate solution for an overdetermined system. The most common method is known as the least square method and it determines the solution with the lowest residual (RMS) error **r**. A suitable set of equations is formed by premultiplying the left and right side of Eq. (2.17) by **GT** (Nash, 1990).

$$\mathbf{r} = \mathbf{GT} - \mathbf{F} \tag{2.16}$$

$$\mathbf{G}^T\mathbf{GT} = \mathbf{G}^T\mathbf{F} \tag{2.17}$$

2.4.2 Applying VFM to Synthetic Data

Extensive tests and simulations were conducted to verify the inversion algorithm. Many synthetic patches of cells were generated using *Simba*'s 2D Voronoi Generator and these were run in the standard forward direction so that the time course was obtained. The data from this forward model was then used as the input for the *Scar* algorithm, so it could calculate the edge tensions and pressures through the mathematical algorithm described in the previous section. Different configuration and load experiments were conducted and the inversion algorithm was able to accurately depict the driving forces.

2.4.3 VFM on Live Data for Ventral Furrow Formation

Ventral furrow formation (see Figure 2.14) is an important morphogenetic process in *Drosophila*, and it occurs over a period of approximately twenty minutes. This process is relatively simple and well understood by researchers although a lack of quantitative and numerical analysis still exists (Leptin, 1999). VFM, however, allowed the edge tensions and pressures that drive this process to be mapped.

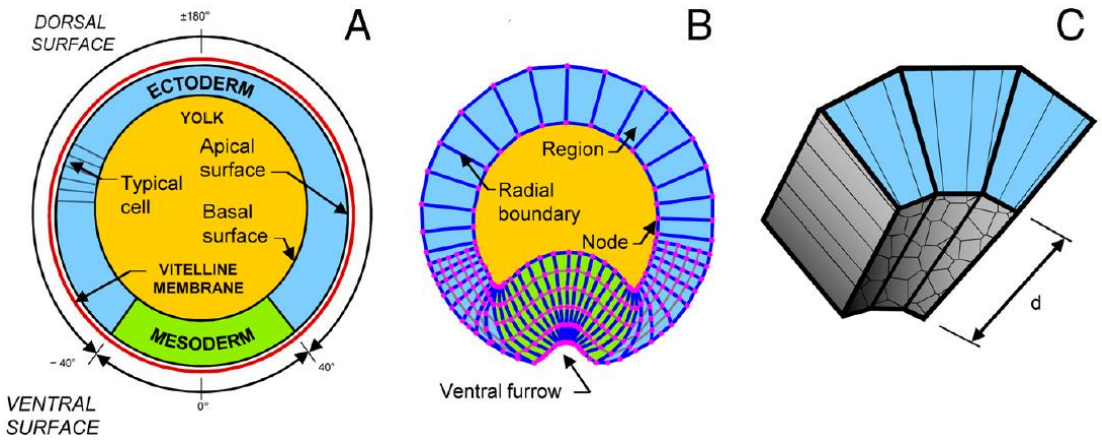

Figure 2.14 – Ventral furrow invagination (Brodland et al., 2010b)

The first step in conducting VFM on experimental data is to collect images of the embryo at regular intervals during the development process. The cell edges are made visible through florescent markers (Kaltschmidt et al., 2002). A sample of a typical image with florescent-dyed embryo is shown in Figure 2.15. Individual cells are then demarcated using the watershed technique (Beucher & Meyer, 1992).

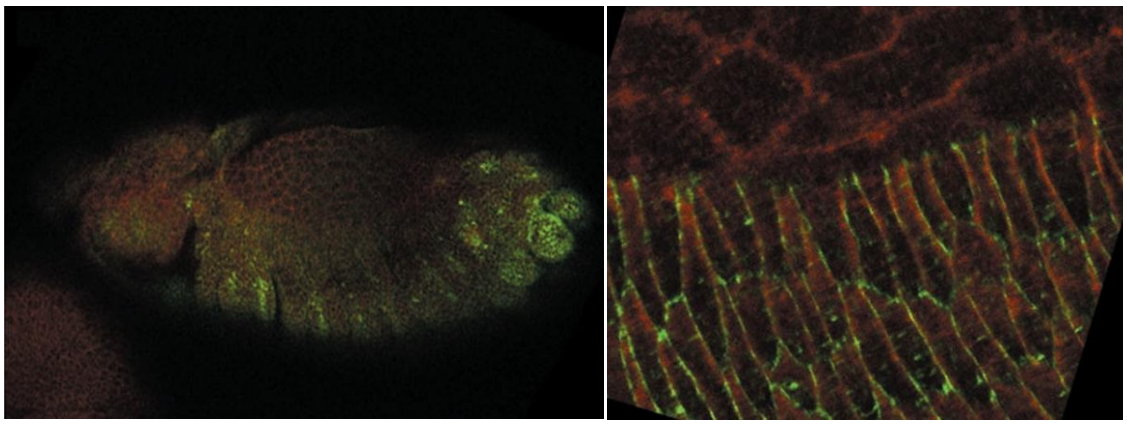

a) b)

Figure 2.15 – Sample image of a florescent dyed embryo. a) The whole *Drosophila* embryo dyed in florescent markers. b) Image capturing a section of the embryo. The upper half of the image shows the amnioserosa cells and the bottom half of the image shows the epidermis cells. (Kaltschmidt et al., 2002)

The cellularized images were then digitized and used as input for VFM. VFM showed that a strong tension acted along the apical surface of the dorsal-most cells, while the inside surface of the upper cells (the ectoderm) was also under tension. Figure 2.16 shows the tensions as a function of angular position and time. The edge tensions yielded a parabolic profile as a function of angular position where the maximum edge tension occurred at the base of the cross section or the angular position of zero degrees (Brodland et al., 2010b; Conte et al., 2012).

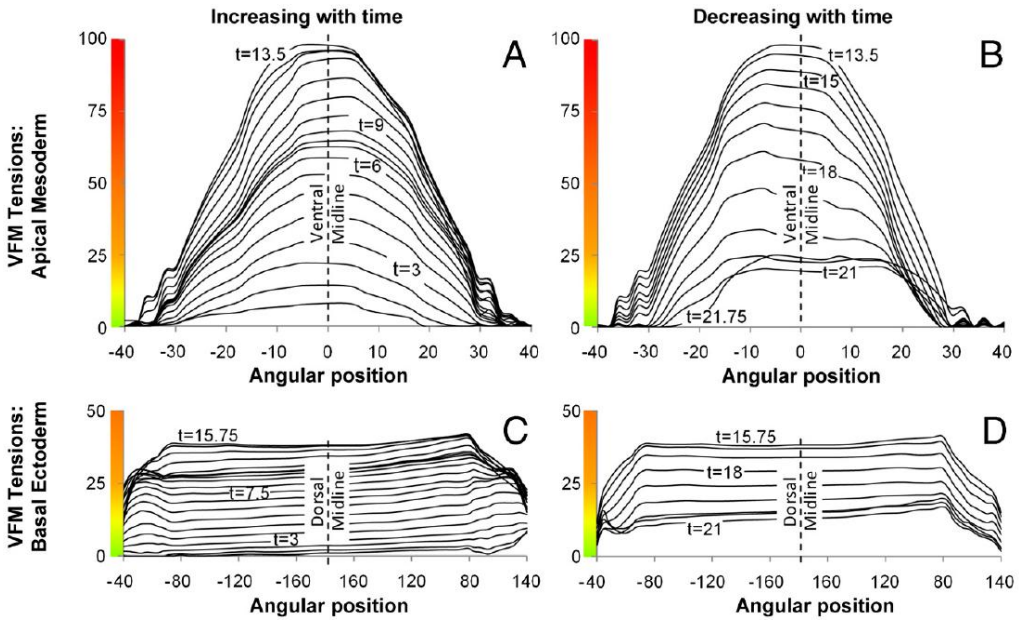

Figure 2.16 – VFM results of ventral furrow invagination (Brodland et al., 2010b)

This study was able to demonstrate the potential of using VFM to study embryogenesis. Mutant phenotype embryos were also studied. *Bnt* was used to test the contribution of surrounding forces, *arm* was used to determine the role of cell-cell adhesion, and *cta/t48* was used to test the contribution of apical constriction. The potential of VFM as a tool to study morphogenetic problem was well demonstrated and was of great interest to analyze other morphogenetic processes (Conte et al., 2012).

2.4.5 VFM Applied to Wound Healing

Wound healing in *Drosophila* embryos is another well known morphogenetic process. When a wound is introduced, the surrounding cells undergo significant movements and shape changes as the healing progresses. Figure 2.17 is a sample of one of many wound healing experiments conducted in Professor Hutson's lab, where a laser point wound was initiated and the healing progress was captured using a confocal microscope.

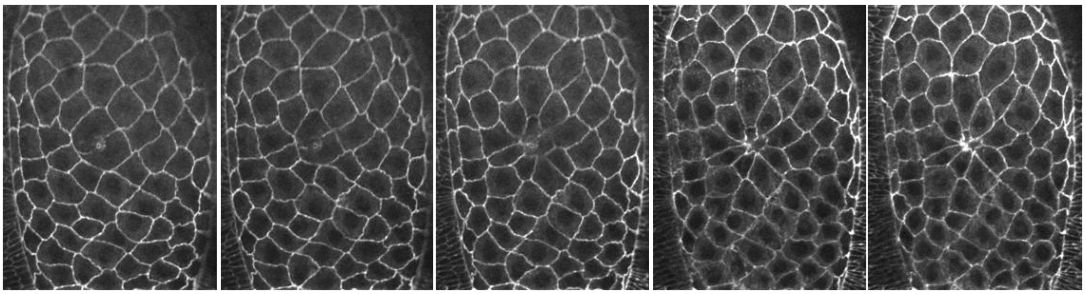

Figure 2.17 – Point wound experimental data healing process

The Figure 2.17 shows a sample of 5 frames out of the 50 frames that were collected. For this particular experiment, the healing process was captured over a time duration of 840 seconds. The obtained images were digitized and transformed into a FE file configured for VFM, shown in Figure 2.18.

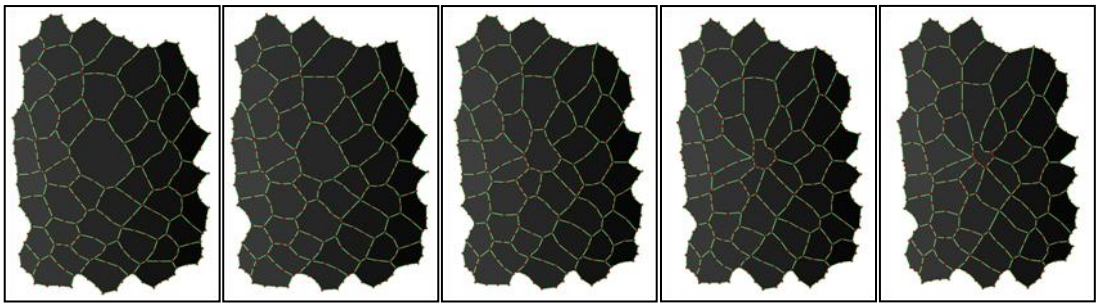

Figure 2.18 – Digitized point wound experimental data healing process

When VFM was applied, the inversion results were difficult to interpret. This raised the questions about why VFM worked for ventral furrow formation but not wound healing. Perhaps wound healing is driven by more than just edge tensions and pressures. A primary goal of this thesis is to addresses this important issue.

Chapter 3
Methods

This chapter describes the development of quantitative measures that can be used to characterize the geometries of cells near a wound so that the results of simulations can be compared with each other and with experimental data. Experimental data were obtained from our collaborator, Prof. Hutson.

3.1 Data Requisition and Configuration for Forward Simulation

The dorsal closure stage of development is of high interest to many research groups as a model for morphogenetic changes as well as healing. Different types of wound shapes can be introduced to the cell patch as shown in Figure 3.1.

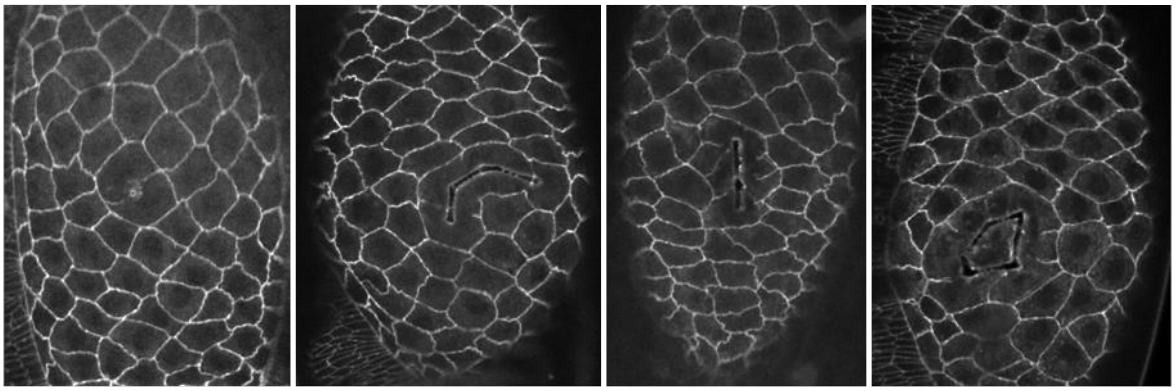

Figure 3.1 – Different wound ablation experiments. Point wound, C-wound, line wound and circular wounds are shown from left to right, respectively.

Time-laps movies from each kind of wound were digitized and converted to a Cell2D FE *Simba* file using a watershed algorithm developed in our lab by PhD candidate, Ahmad Ehsandar. Dashpots were used to model the viscosity of the cytoplasm in the cells. The visible cells were enclosed in a rectangular box and the gap between the cell patch and the box (see Figure 3.2) filled with additional model cells. The rectangular shape of the enclosure facilitates application of far-field stresses and constraints.

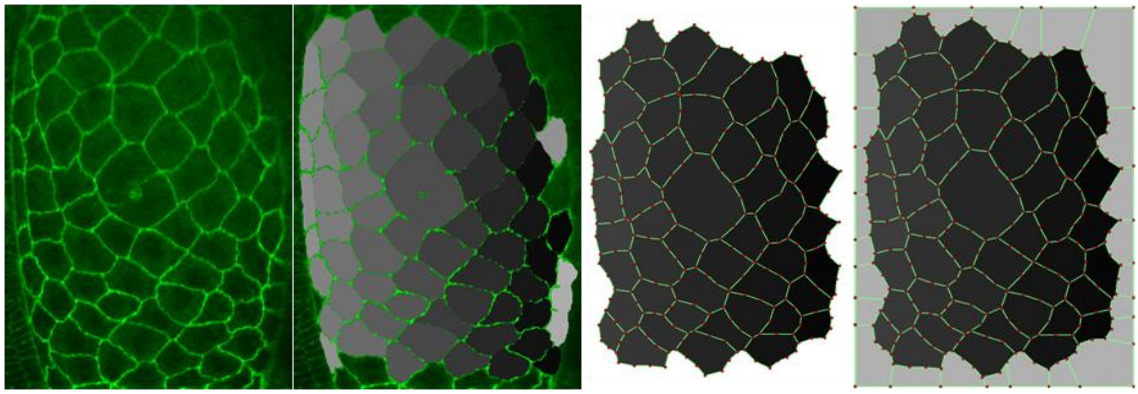

Figure 3.2 – The digitization process

Prior to introducing a wound to the patch, the forces in the amnioserosa cells are under equilibrium. Because the far-field stresses and apical tensions are in balance, creating a wound upsets the balance of the forces. The wound expansion at the time of ablation is known as the recoil phenomena and is shown in Figure 3.3 (Hutson et al., 2009). For purposes of this study, the starting geometry is two to three frames after ablation of the cells because the wound expands (recoils) for approximately 30 seconds before healing begins. The healing process may take 30 times longer.

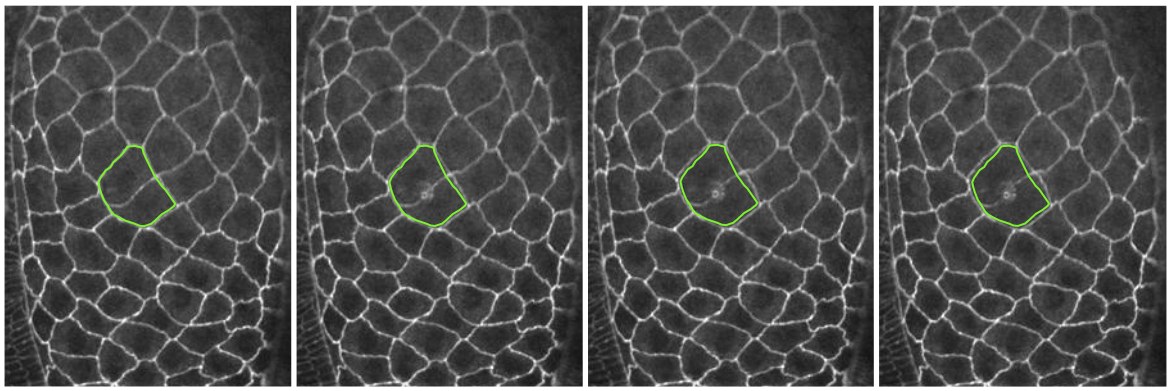

Figure 3.3 – The recoil phenomenon of point wound

3.2 Development of Quantitative Measures

Here, we develop a set of quantitative measures to describe the geometric characteristics of the cells in a patch. The quantitative measures are nondimensional so that they are independent of image scale. To better identify and classify cells, we introduce the following terms:

Wound

The “wound cell” is one or more physical cells that have been severely damaged as a result of the laser incision. They can no longer contain pressure. At any moment, the wound area is nondimensionalized to its initial area.

Ring 1

The cells directly bordering the wound cell are labeled as ring 1 cells. This group of cells changes significantly in shape and size throughout the healing process. Their combined area is nondimensionalized against their initial area.

Ring 2

Ring 2 cells border ring 1 cells and they are also prone to significant changes. The area of the ring 2 cells are nondimensionalized to their initial area.

Light

As shown in Figure 3.2 and 3.4, the cells artificially created to form a rectangular enclosure around the cell patch are labeled as light (as opposed to dark) cells. These cells are not of interest from an analysis standpoint but they play an important role in transmitting any external forces and constraints applied at the boundaries into the cell patch.

Normal

Cells which are three cells or more away from the wound are labeled as normal cells. These cells are monitored to capture any changes that occur in the patch further away from the location of laser incision.

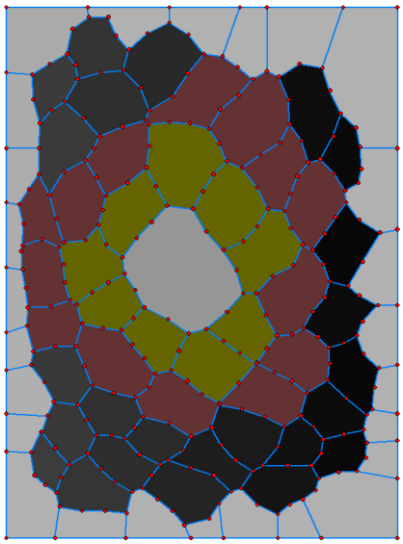

Figure 3.4 – Point wound cell type identifications

Having defined a number of cell types, we next develop a set of geometric parameters to allow quantitative comparison between simulations and experiments.

3.2.1 Volume and Area

Although the amnioserosa cells are 3D, they can be simplified into 2D because they form planar aggregates (Brodland et al., 2007). Area changes are important to wound healing, as shown in Figure 3.5. It is not clear whether cell volume is lost or whether cell height changes to accommodate the area change.

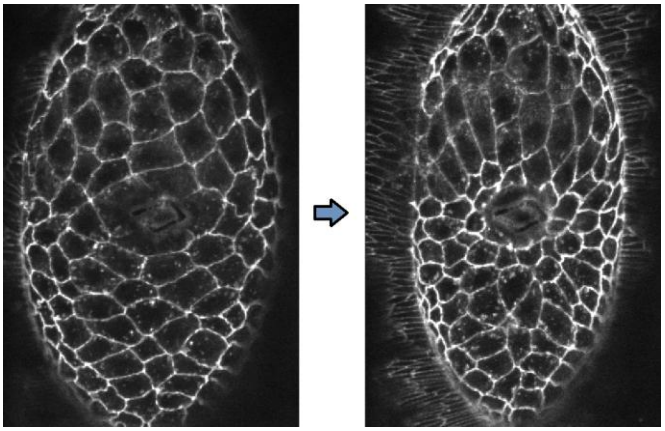

Figure 3.5 – Area change

3.2.2 Circularity

The first shape measure is called circularity and it characterizes how closely a cell shape resembles a circle. Circularity is defined as the ratio where A and P are the area and perimeter of the cell, respectively. Perfectly round cells will have a circularity of one, whereas cells which deviate from a circle will have a value closer to zero (see Figure 3.6).

$$Circularity = \frac{4\pi A}{P^2} \tag{3.1}$$

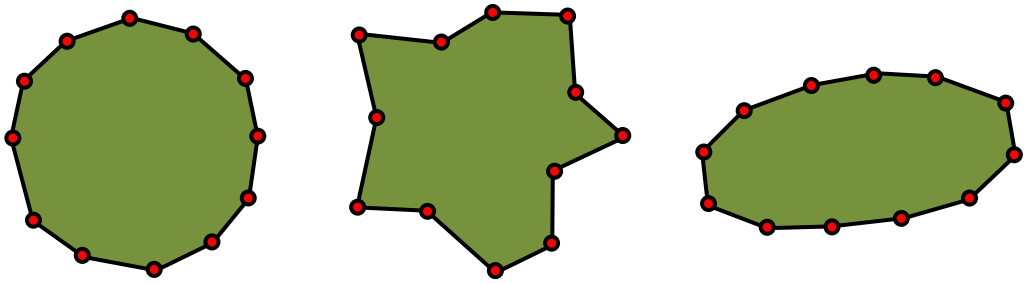

a) circularity ≈ 0.95 b) circularity ≈ 0.60 c) circularity ≈ 0.82

Figure 3.6 – a) Circular shaped cell that yields a high circularity value. b) Jagged shaped cell yields a low circularity value. c) Oval shaped cell yields a low circularity value.

Circularity is likely associated with relative cell pressure since as the pressure inside a cell increases, it has a tendency to round up in shape. In contrast, an unpressurized cell is more likely to have a lower circularity. The circularity of a hexagonal cell is $\pi\sqrt{3}/6 \approx 0.91$ and values for some other representative geometries are shown in Figure 3.6.

3.2.3 Wedgeness

Cells bordering the wound often develop a distinctive elongated wedge shape (similar to the shape of a pie slice) where the cells points toward the center of the wound as shown in Figure 3.7. To characterize this type of geometry, we define a wedgeness parameter where E1 is the length of the edge bordering the wound, E2 is the opposite edge length parallel to E1, and PL is the perpendicular length between edges E1 and E2. These quantities are demonstrated in Figure 3.8.

$$Wedgeness = (1 - E1/E2)(1 - E1/PL) \quad (3.2)$$

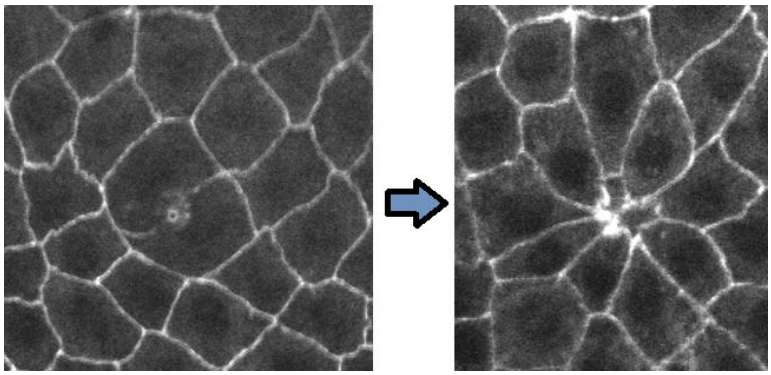

Figure 3.7 – Cells become wedged shaped as healing proceeds

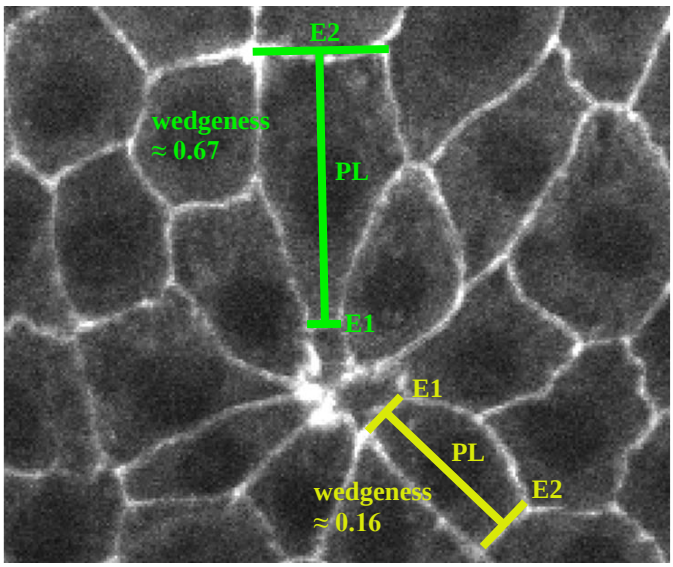

Figure 3.8 – Demonstration of wedgeness parameters on a cell

The first term, (1 – E1/E2), quantifies the ratio of the two lengths of the wound edge and the opposite edge parallel to the wound, whereas the second term, (1 – E1/PL), captures how long the cell is wedged. Rectangular shaped cells will yield a wedgeness value close to zero and pie shaped cells will yield a value closer to one (Figure 3.8).

3.2.4 Isoangularity

Isoangularity characterizes the ratios of the angles at a triple junction. The triple junction angles of an annealed cell patch with identical edge tensions tend uniformly toward an angle of 120 degrees. Introducing a variation in magnitude on one edge will form a force imbalance and cause all the junction angles to change. Figure 3.9 demonstrates how the angles at a junction will vary when a non-uniform tension is introduced. The mathematical definition of the isoangularity parameter is defined by Eq. (3.3).

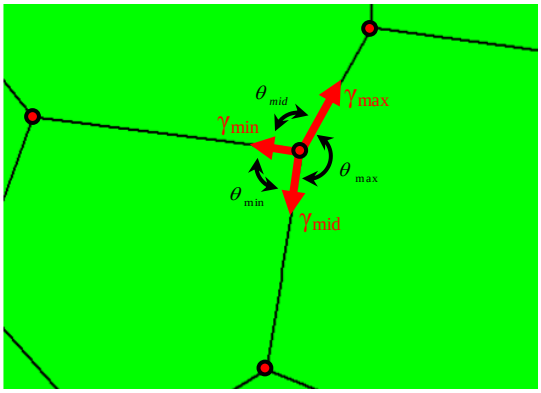

Figure 3.9 – Isoangularity of cells

$$I = \frac{\theta_{max} - \theta_{min}}{2\pi} \tag{3.3}$$

where θ_{max} is the largest and θ_{min} is the smallest angle at a triple junction. For isometric junctions, the isoangularity will tend to zero (See Figure 3.10).

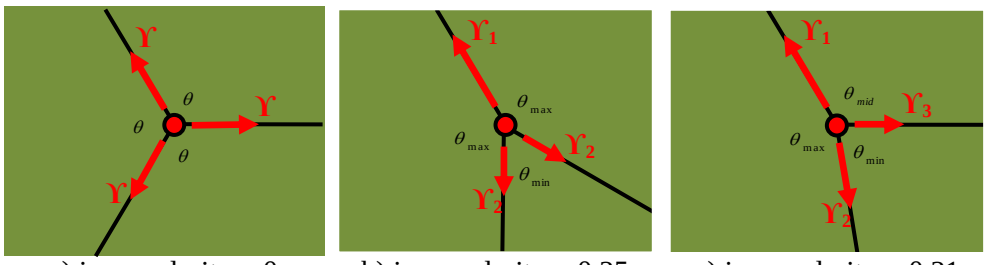

a) isoangularity ≈ 0 b) isoangularity ≈ 0.25 c) isoangularity ≈ 0.21

Figure 3.10 – Example of isoangularity

3.2.5 Crinularity

The Cell2D model has the ability to accommodate multiple nodal points along individual cell edges. Cell interfaces may appear straight or crinkled depending on the net effects of forces that are present in it. Edges that carry a high tension will tend to be straight. Crinularity characterizes the severity of how crinkled or wrinkled the cell edge is by taking the sum of all angular excursions θ_i along the path of the edge (Figure 3.11).

$$Crinularity \quad y = \frac{\sum Angles}{360} = \frac{\theta_1 + \theta_2 + \ldots + \theta_n}{360} \tag{3.4}$$

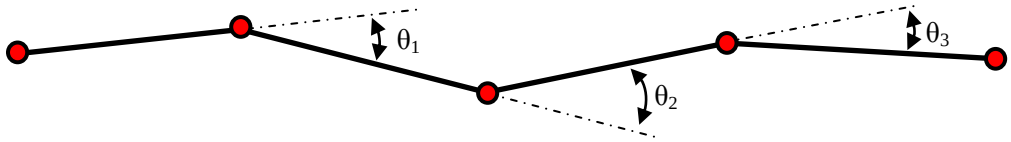

Figure 3.11 – Cell Crinularity

3.3 Development of Constraints and Conditions

In forward FE modeling, applying the appropriate forces and constraints are crucial to the outcome of the analysis. In this section, the constraints and boundary conditions used are defined.

3.3.1 Constraining the Patch

The cell patch must have 3 constraints that is able to prevent all 3 types of planar free body motions. In a typical model, the starting geometry is enclosed in a rectangular box (see §3.1), and throughout the analysis, the cell patch is constrained to maintain a rectangle enclosure. While the bottom left corner is restricted from translation motion, the left edge of the patch is restricted from horizontal motion, and the bottom edge of the patch is restricted from vertical motion (Figure 3.12). In this way, the patch is constrained from translation and rotation

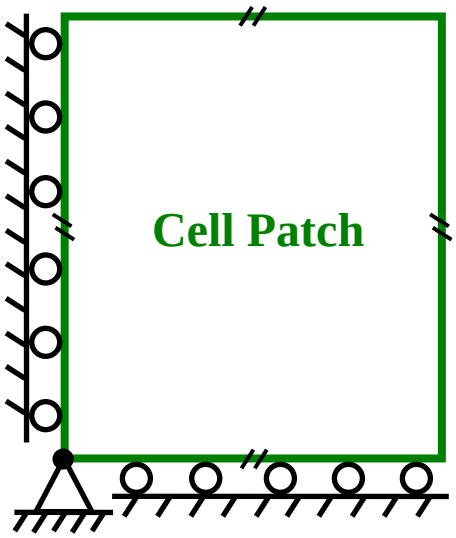

Figure 3.12 – Constraining the cell patch

3.3.2 Wound Cell

Following ablation, the wound cell is exposed to the medium and is assumed to carry zero pressure. It is also assumed to have zero viscosity.

3.3.3 Volume Constraint and Pressure

In the model, cell volume can be specified in two ways – a volume constraint and an elastic volume dependent on pressure. When a cell undergoes deformation, the volume constraint restricts the deformation so that the volume remains constant. The volume constraint is specified in the element control section in the finite element file.

```
ECCell1Nrml    PlaneStrain    0    0    1    VolumeConstraint    -1
```

Volume pressure is different from a volume constraint, because its volume can change according to its internal pressure. When a volume pressure is specified for a cell, it can carry a pressure and is given by Eq. (3.5).

$$pressure = \left(\frac{V_0 - V}{V_0} \right) \times Volume \quad Pressure \tag{3.5}$$

where V_0 is the initial volume and V is the current volume. The volume pressure coefficient is also specified in the element control section in the finite element file. In the example shown, the magnitude of the volume pressure is 10*dyne/pixel*^{2}.

```
ECCell1   PlaneStrain   0   0   1   VolumePressure   10
```

3.3.4 Velocity Boundary Condition

The velocity boundary condition moves the boundary of a patch at a specified velocity. Experimental data shows the leading edges of the amnioserosa closing at a constant speed during dorsal closure and wound healing, as shown in Figure 3.13 (Hutson et al., 2003).

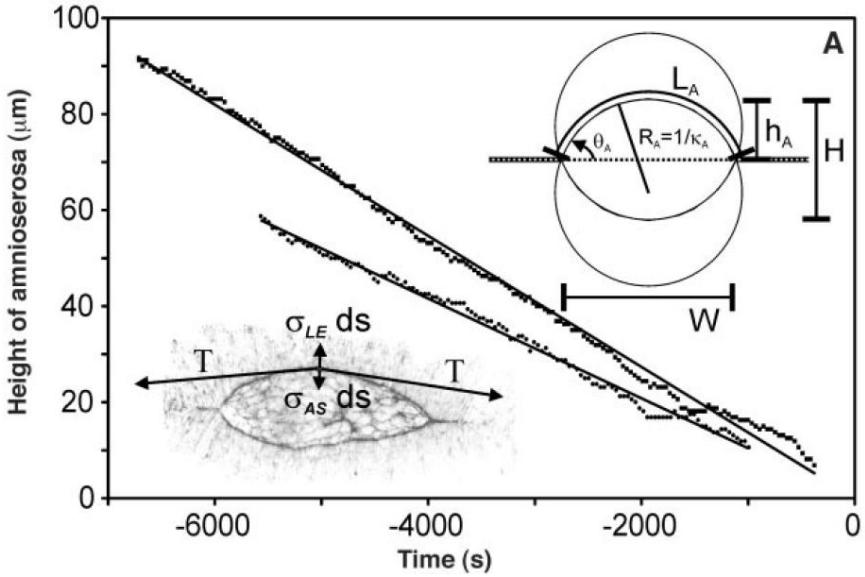

Figure 3.13 – Displacement of the leading edges in amnioserosa (Hutson et al., 2003)

The velocity boundary condition is applied by specifying a node, at the top right corner of the patch, to move at a certain velocity.

```
6   Corner   26   VX   -0.0435   VY   -0.021
```

Since the cell patch is constrained to remain a rectangular shape, specifying a velocity boundary condition to the corner node will force the top and right edge to move, respectively, as shown in Figure 3.14.

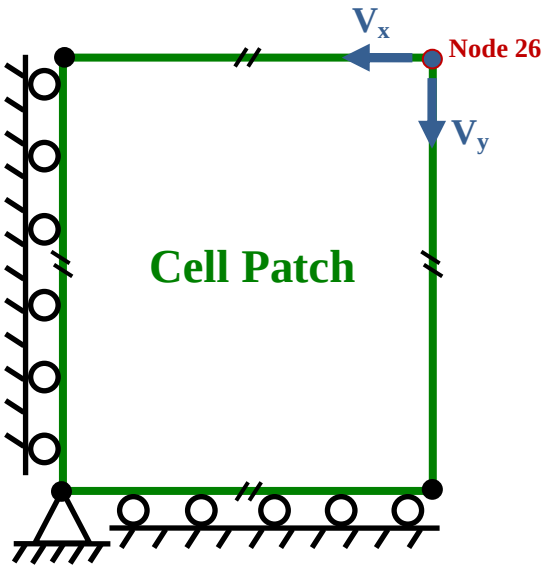

Figure 3.14 – Cell patch with velocity boundary condition

3.3.5 Cell-to-Cell Permeability

The cell-to-cell permeability constant specifies how fluid can flow from one cell to its neighbor when a pressure gradient exists (Spring & Ericson, 1982). A cell with a high pressure will lose fluid to its neighboring low pressure cells if the membrane permeability is not zero. The total volume of all the cells will remain constant. The amount of fluid that can transfer through a cell membrane depends on the pressure gradient, edge length, thickness and incremental time step, which is given by Eq. (3.6). Increasing the permeability has the same effect as increasing the number of channels in a cell. Figure 3.15 demonstrates responses across membranes with high and low permeability constants.

$$Fluid\ \ Exchange\ \ Rate\ = (length\ ) \times (thickness\ \ ) \times (time\ \ increment\ \ ) \times (cell\ \ permeabili\ \ ty\ ) \tag{3.6}$$

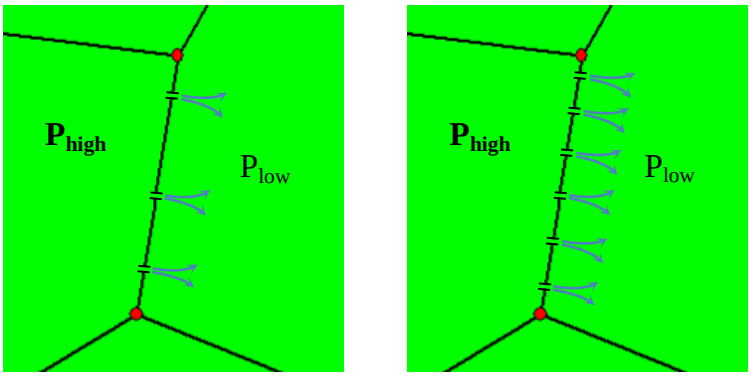

Low Permeability High Permeability

Figure 3.15 – Cell-to-cell permeability shown on cell edge

The cell-to-cell permeability is implemented in the element control section in the finite element file by specifying the permeability value for its corresponding interface between cell types, organized in a matrix form. The first matrix specifies the interfacial tensions (units are in *dyne*) and the second matrix specifies the permeability between the cell interfaces.

Normal	*Wound*	*Light*	*Ring1*	*Ring2*	*Medium*
0.1	*0.1*	*0.1*	*0.1*	*0.1*	*0*
	0.1	*0.1*	*0.1*	*0.1*	*0*
		0.1	*0.1*	*0.1*	*0*
			0.1	*0.1*	*0*
				0.1	*0*
					0

Permeability					
0.14	*0.14*	*0.0*	*0.14*	*0.14*	*0*
	0.14	*0.0*	*0.14*	*0.14*	*0*
		0.0	*0.0*	*0.0*	*0*
			0.14	*0.14*	*0*
				0.14	*0*
					0

In the example above, all the cells have a permeability value of 0.14, except for cell interfaces between light cells and the medium.

3.3.6 Apical Permeability

The apical permeability is similar to the cell-to-cell permeability, and it accommodates channels for the fluid to flow out through the apical surface of the cell into the adjacent medium. Figure 3.16 demonstrates the cell-to-cell and apical permeability for a given cell.

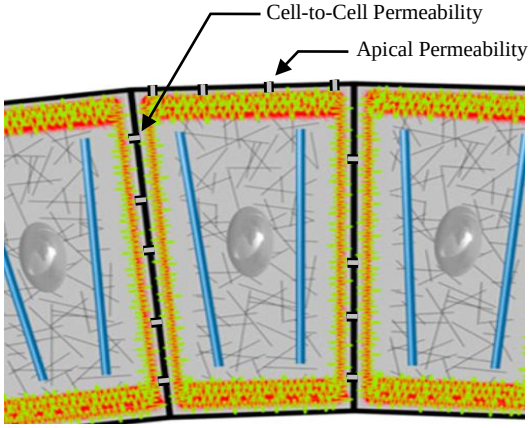

Figure 3.16 – Graphical depiction of apical and cell-to-cell permeability (Brodland et al., 2010b)

3.4 Development of Forces

There are a number of driving forces that contribute to the movement of cells during embryogenesis and wound healing. In this section, different type of forces that contributes to the movement of cells during the wound healing process are identified.

3.4.1 Far-Field Stress

The far-field stress is applied to the patch in a way similar to the displacement boundary condition (Figure 3.17). By applying a force (reaction) to the corner node, the force is transmitted to the edge of the cell patch.

6	*Corner*	*26*	*RX*	*32*	*2.0*	*RY*	*15*	*1.5*

In the example, a load of 2.0*dyne/pixel*^{2} is applied along the edge between node 26 and 32, while a load of 1.5*dyne/pixel*^{2} is applied along the edge between node 26 and 15. Since the entire cell patch is constrained to form a rectangle (see §3.3.1), applying a force to the corner node (node 26) will distribute the load along the entire edge of their respective x and y directions.

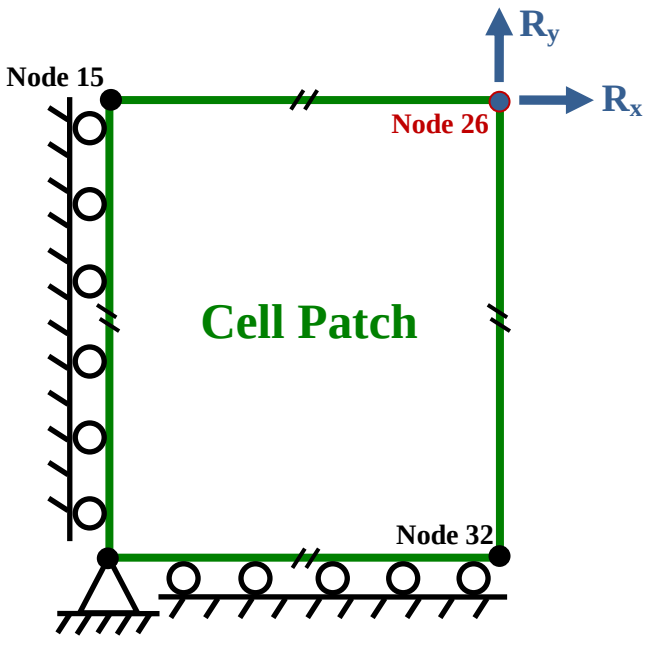

Figure 3.17 – Cell patch with far-field stress

3.4.2 Nodal-Based Local Area Contraction

In *Drosophila* embryos, the amnioserosa cells undergo contraction during dorsal closure. Although it has been a challenge to understand why and how cells contract, progress has been made in mapping the actin that generates the contractile forces (Jacinto et al., 2002; Kaltschmidt et al., 2002). The amnioserosa cells typically undergo four cycles of contraction during the time frame used in our analyses (see Figure 3.18).

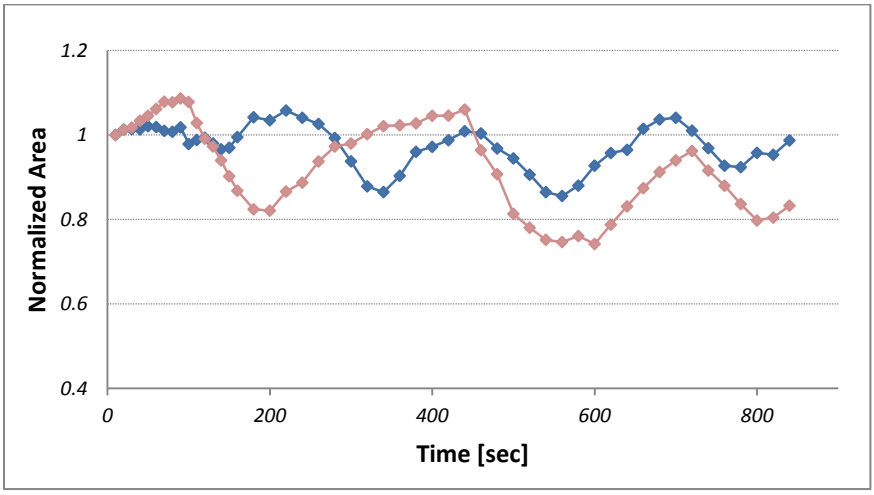

Figure 3.18 – Cell area profile during contraction

The nodal-based area contraction models the contraction in a cell, defined by 5 parameters that govern the contraction: contraction rate, strength, strength variation, duration, and duration variation. The contraction in a cell is initiated by including the contraction command and its parameters in the simulation control section in the finite element file and it must be used with the volume pressure condition.

```
Contraction    0.6    1    0.5    80    10
```

In the example above, the contraction rate = 0.6%, strength =1*dyne*, strength variation = 0.5*dyne*, duration = 80*sec*, and duration variation = 10*sec*. The rate of contraction measures the percentage of cells that are under contraction, where a value of one indicates all cells are under contraction and a value of zero indicates no cells are under contraction. The contraction is modeled by creating center node, which is randomly placed at half a radius range given by Eq. (3.7, 3.8, & 3.9), and is demonstrated in Figure 3.19.

$$Radius = \sqrt{\frac{Area}{\pi}} \tag{3.7}$$

$$Range = Radius \times 0.5 \tag{3.8}$$

$$Center\ \ Node = Cell\ \ Center + Random\ \ (\pm Range) \tag{3.9}$$

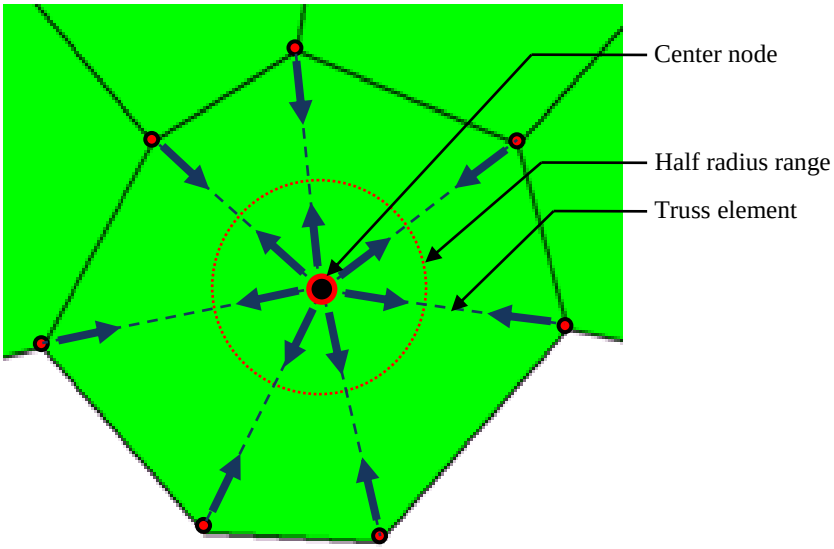

Figure 3.19 – Nodal-based local area contraction

Once the center node is defined, a radial tension is applied from the center node to all the nodes surrounding the cell. The tension depends on the specified strength and its duration, according to Eq. (3.10). The length in the equation refers to the distance between the center node and the corresponding node in the cell. The strength varies as a sinusoidal function of time, according to Eq. (3.11). However, only the positive value of the sinusoidal function is used.

$$Radial \quad Tension \quad = Strength \quad \times \frac{Length}{Radius} \tag{3.10}$$

$$Strength \quad Total \quad = Strength \quad \times \sin\left(\frac{Start \quad Time}{Duration}\right) \tag{3.11}$$

3.4.3 Pressure-Based Local Area Contraction

The pressure-based area contraction is implemented differently in comparison to the nodal-based area contraction. The nodal-based area contraction has the ability to contract non-uniformly, where the shape of the cell changes as it contracts. The pressure-based contraction does not change the shape of the cell as it contracts. The pressure-based contraction has a similar affect to scaling the size of the cell as shown in Figure 3.20.

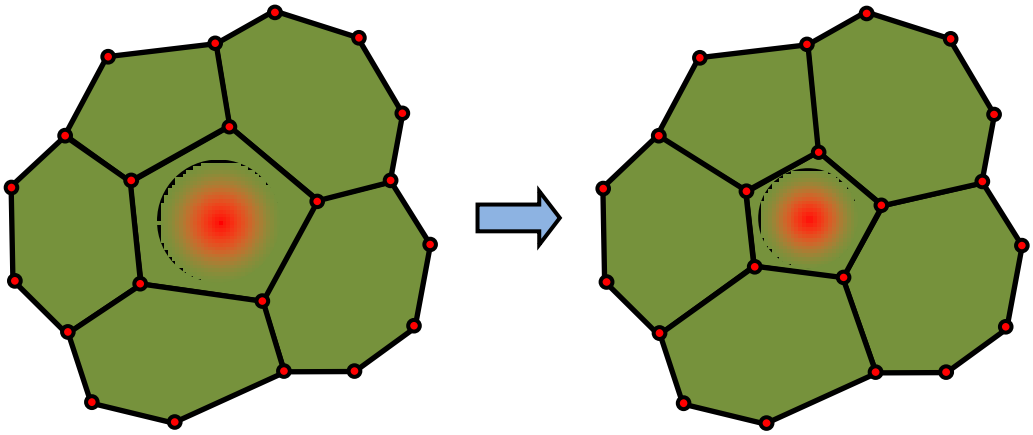

Figure 3.20 – Pressure-based local area contraction

The use of volume pressure instead of a volume constraint allows a contracted cell to expand. Otherwise, a contracted cell will have no means to return to its initial size. A high-volume pressure will resist the contraction, resulting in a low-area decrease during contraction, and vice versa. Hence, the volume pressure should be adjusted appropriately to resemble the experimental data.

3.4.4 Edge-to-Edge Interfacial Tensions

The Differential Interfacial Tension Hypothesis (DITH) is used to model the interfacial tension of cells (Brodland, 2002). The interfacial tension between two cells (arbitrarily identified as A and B) can be represented as a combination of forces acting in the cells, illustrated by Eq. (3.12) and Figure 3.21 (Brodland, 2002).

$$\gamma^{AB} = F^{A}_{Mem} + F^{B}_{Mem} + F^{A}_{MF} + F^{B}_{MF} - F^{AB}_{Adh} + F^{AB}_{Other} \tag{3.12}$$

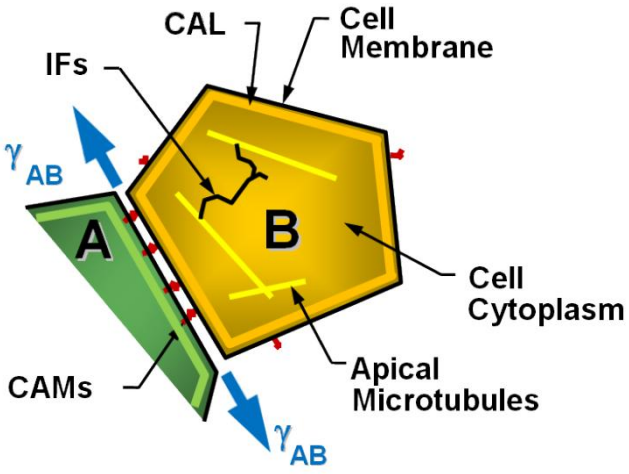

Figure 3.21 – Contribution to interfacial tensions (Cranston, 2009)

The magnitude of the interfacial edge tension can be specified according to the cell type. The magnitude of the interfacial tension is controlled by specifying its corresponding values in a matrix form in the element control section in the finite element file.

Normal	*Wound*	*Light*	*Ring1*	*Ring2*	*Medium*
0.1	*0.1*	*0.1*	*0.1*	*0.1*	*0.0*
	0.1	*0.1*	*0.1*	*0.1*	*0.0*
		0.1	*0.1*	*0.1*	*0.0*
			0.1	*0.1*	*0.0*
				0.1	*0.0*
					0.0

In the example above, all the cells bordering the medium have an interfacial tension of 0.0*dyne* and all other interfaces have a tension of 0.1*dyne*. The use of a matrix to specify interfacial tensions gives flexibility and control over the simulation.

3.4.5 Apical Tension

The apical tension is an area tension acting normal to the edges of the amnioserosa cells. It is equivalent to a negative pressure acting on a cell. The apical tension is applied to the cells in the simulation by specifying the desired tension value in the element control section in the finite element file.

```
ECCell1  PlaneStrain  0  0  1  VolumeConstraint  -1  ApicalPermeability  0.0024  ApicalTension  0.12
```

The apical tension must be used in conjunction with apical permeability and volume constraint conditions. The apical tension and permeability values can be specified for each cell type, giving flexibility and control over the simulation.

3.5 Configuration and Analysis File

3.5.1 Node Block

The node block in the finite element file is where the nodal points, x and y coordinates, are defined. The nodes form the grid or the mesh of the system. Nodes define the perimeters of the cells and are points where the mathematical equations are computed (refer to §2.3.1). Increasing the number of nodes will

better capture the geometry, but will increase the computational resource required for the mathematical calculations. Figure 3.22 demonstrates how increasing the number of nodes can better capture a cell's geometry. The file is structured so that it can be in the same format as the output file from any time step. Thus, any output file can be used as an input file for a successive series of steps. This feature is useful for scenarios where configuration or analysis parameters are changed manually.

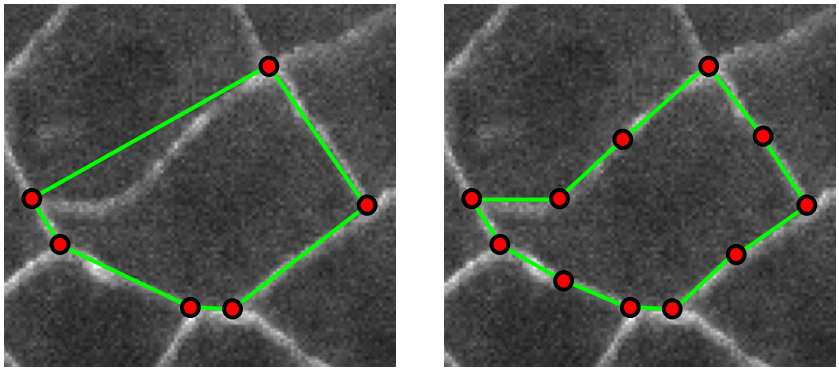

Figure 3.22 – Nodal points used to capture cell geometry

The finite element files are configured such that the first column lists the node identifier, the second and third column lists the x and y coordinates of the node, respectively. The fourth and fifth column lists the original x and y coordinates of the node. Following the nodal coordinates are a list of associated edges, where "-1" are space fillers. The following is a sample of the node block in the finite element file:

```
BEGIN_NODES
    5     276     -74     276     -74     Edge    12    13    410    -1
    6     225     -82     225     -82     Edge    20    229   411    -1
    ⋮      ⋮       ⋮       ⋮       ⋮       ⋮      ⋮     ⋮     ⋮      ⋮
    138   63      -386    63      -386    Edge    193   198   199    -1
```

3.5.2 Edge Block

An edge forms the boundary between two elements and is also the direction along which the interfacial tension acts. In the finite element file, the first column lists the edge identifier, while the subsequent two columns list the associated nodes that form the edge. The fourth and fifth columns list the cells that the edge is bordering. The subsequent columns describe the edge's age, color and orientation, where the default values are used. Age is used for time-varying features relevant to mitotic daughter cells and sinusoidally-contracting amnioserosa cells, and it has a value of zero in most initial-start files. The cell identifier of "10000001" refers to the medium, and it is an indication that the edge is bordering the medium. The following is a sample of the edge block in the finite element file:

```
BEGIN_EDGES
    12      156     5       10      90          Age 0   Color (255,0,0)   Orientation 0
    13      5       14      10      91          Age 0   Color (255,0,0)   Orientation 0
    ⋮       ⋮       ⋮       ⋮       ⋮           ⋮       ⋮                 ⋮
    451     327     300     80      10000001    Age 0   Color (255,0,0)   Orientation 0
```

3.5.3 Material Block

The material block in the finite element file defines the material types. There are a number of materials commonly used in finite element analysis, such as elastic, viscous, viscoelastic and truss material. The first column of the material block defines the type of material that is used, where viscous material (VI) is used for cell elements. Following the type of material is the value of the viscosity and Poisson's ratio. The following is a sample of the material block in the finite element file:

```
BEGIN_MATERIALS
VI1  1    0
VI2  0.1  0
```

The same material type can be specified multiple times by varying the index number followed by the material type. In the example above, there are two viscous materials defined, where "VI1" has a viscosity of one and "VI2" has a viscosity of zero.

3.5.4 Element Block

The element type is what gives character to a cell and its properties. Different cell element models were introduced in §2.3.1. In the element block, the first column lists the cell identifier. Following the cell identifier is the type of cell that is used. In *Simba*, there are different classes of cell element models, such as Brick, Cell, Cell2D, Cell3D and Truss elements. However, the Cell2D element model is used for our study. The third column references the material properties used for that cell. Following the material property is the element control block. The column carrying the parenthesis defines the colour of the cell for drawing purposes, and the following column identifies the cell type, described previously in §3.2. The columns following the cell type are the thickness and growth factor of the element, which are 1*pixel* and zero, respectively, throughout the study. The subsequent columns provide the cell's area and age. The second row of the element identifier provides the edges enclosing the cell, and is listed in the counter clockwise direction. The following is a sample of the element block in the finite element file:

```
BEGIN_ELEMENTS
10  Cell2D  VI1  ECCell1Nrml  (10,10,10)     Normal  1   0   InitialArea   0   Area0   Age  0
    Edges   13   230  231  24   39   224  225  12
```

3.5.5 Element Control Block

The element control block in the finite element file specifies the majority of the controls and constraints. The element control block is divided into three main sections, where the last two sections are used to control the interfacial tension and permeability. The following is a sample of the element control block in the finite element file:

```
BEGIN_ELEMENT_CONTROLS
I   ECCell1Nrml  PlaneStrain  0  0  1  VolumeConstraint  -1  ApicalPermeability  0  ApicalTension  0
II      Normal    Wound     Light     Ring1     Ring2     Medium
        0.01      0.01      0.01      0.01      0.01      0
                  0.01      0.01      0.1       0.01      0
                            0.01      0.01      0.01      0
                                      0.01      0.01      0
                                                0.01      0
                                                          0
III     Permeability
        1.0       1.0       0.0       1.0       1.0       0
                  1.0       0.0       1.0       1.0       0
                            0.0       0.0       0.0       0
                                      1.0       1.0       0
                                                1.0       0
                                                          0
    ECCell2Wnd  PlaneStrain  0  0  1  EdgeProperties  ECCell1Nrml
```

In section I, the name of the element control and its planar state of analysis is defined. There are two types of plane state, plane stress and plane strain. For stress and strain analysis, the use of plane stress or strain condition can simplify a 3D problem into a 2D problem. The plane stress condition refers to the state where the normal and shear stresses are zero to the plane of interest (ie, $\sigma_z=\tau_{xz}=\tau_{yz}=0$). As a result, the 3D stress tensor can be simplified to yield Eq. (3.13 & 3.14) (Logan, 2011).

$$\{\boldsymbol{\sigma}\} = [\boldsymbol{D}]\{\boldsymbol{\varepsilon}\} \tag{3.13}$$

$$[\boldsymbol{D}] = \frac{E}{1-\nu^2}\begin{bmatrix} 1 & \nu & 0 \\ \nu & 1 & 0 \\ 0 & 0 & \dfrac{1-\nu}{2} \end{bmatrix} \tag{3.14}$$

The plane strain condition refers to the state where the normal and its shear strains are zero to the x-y plane (ie, ε_z, Υ_{xz}, Υ_{yz}), where tensor **D** is defined by Eq. (3.15).

$$[\boldsymbol{D}] = \frac{E}{(1+\nu)(1-2\nu)} \begin{bmatrix} 1-\nu & \nu & 0 \\ \nu & 1-\nu & 0 \\ 0 & 0 & \frac{1-2\nu}{2} \end{bmatrix} \tag{3.15}$$

The in-plane deformations in the amnioserosa cells are significantly higher than deformations in the thickness direction. Therefore, the plane strain condition is used for the purpose of our study.

The columns following the plane state condition are parameters used in controlling neighbour changes in cells (refer to §2.3.1). The neighbour change controls are not used since it is a rare occurrence in the amnioserosa cells.

There are two types of cell volume conditions, volume constraint and volume pressure. In the example above, a volume constraint condition followed by the volume restoration constant is used. The volume restoration constant of "-1" is used for disabling the volume restoration control, and is not to be used for our study. To apply a volume pressure, the "VolumeConstraint" is replaced with "VolumePressure" and the "-1" is replaced with the magnitude of the pressure. Following the cell volume conditions are the apical tension and permeability descriptors. In the example above, the "ECCell2Wnd" is used for defining the element properties of the wound cell. Since the wound cell is an unconstrained medium, its volume condition was omitted. The application of interfacial tensions and permeability are referenced through declaring "EdgeProperties ECCell1Nrml"; it prevents redundancy in rewriting the matrix that controls the interfacial tensions and permeability.

3.5.6 Boundary Condition Block

The boundary condition block can be divided into four main sections. The first section ensures that patch is constrained to three DOF in different directions. In the first section, the first column indicates the boundary condition identifier, followed by the location and the node that is constrained. The subsequent columns describe the type of motion permitted. The "DX" and "DY" indicates the displacement in the x and y direction, respectively. To fix the bottom left corner of the patch, a displacement value of zero was assigned to "DX" and "DY". In the second boundary condition, the use of "NY" allows movement along the y-axis. Similarly, the third boundary condition constrains movement in the y-direction, while allowing movement along the x-axis.

The second section in the boundary condition block controls neighbor changes, but is not used for our study. The third section controls the velocity boundary condition (refer to §3.3.4). Through the implementation of "VX" and "VY", the velocity can be specified. Similarly, the far-field stress can be

applied by replacing “VX” and “VY” with “RX” and “RY” in addition to its respective far-field stress magnitudes. The last section (EdgeBottom, EdgeLeft, EdgeRight, and EdgeTop) constrains the patch to maintain a rectangular boundary. The following is an example of the boundary condition block in the finite element file:

```
                BEGIN_BOUNDARY_CONDITIONS
I: Patch        1   Corner     300   DX   0        DY   0
constraint      2   Corner     318   DX   0        NY
                3   Corner     304   NX   DY       0
II: Neighbor    4   Function   0     1    312      0    -1     318   0
changing        5   Function   1     0    304      -1   0      312   0
III: BC         6   Corner     312   VX   -0.0435  VY   -0.021
                EdgeBottom     EdgeN   300 301 302 303 304
IV: Rectangle   EdgeLeft       EdgeN   318 319 320 321 322 323 324 325 326 327 300
constraint      EdgeRight      EdgeN   304 305 306 307 308 309 310 311 312
                EdgeTop        EdgeN   312 313 314 315 316 317 318
```

3.5.7 Control and Output Block

The control block in the finite element file defines the global parameters in the forward simulation. There are a number of controls that require specification, such as the simulation duration, time increment, data requisition rates and outputs. The simulation duration is governed by the number of steps and the size of the step. The step size controls the period between one time step and the next. The total time of the simulation is the product of the number of steps and step size. The active step and active time keeps track of the current step and time for each finite element file.

Unlike other force applications, the local area contraction developed in §3.4.2 and §3.4.3 are implemented in the control block by specifying the “Contraction” followed by its control parameters. The contraction can be specified according to different cell types by including “SpecifyOnlyForCellType” followed by a list of cell types.

The output variables are specified in the control block. By specifying a list of variables in “OutputVariables”, the variable will be reported in the “BEGIN_OUTPUT_VARIABLES” section in the finite element file. There are a number of output variables, such as GeometricParameters, Area, Pressure, AvgPressure, NumCells and many other variables. The variables are also logged in a “.csv” file. The following is an example of the control and output block in the finite element file:

```
BEGIN_CONTROLS
StartingTime   0
NumberSteps   1000
StepSize   1
ActiveStep      0
ActiveTime      0
OutputEvery    5
OutputEveryData   5
ConstraintReduction      1     1     2     1     0.800000011920929
BlowUp   1000
Solver      UmfPack
StiffnessReduction   0
Contraction    0.2    2    0    1.8    0    SpecifyOnlyForCellType   Normal   Ring1   Ring2
KtoA       Traditional
RandomSeed   777
OutputVariables
ScreenOutput

BEGIN_OUTPUT_VARIABLES
```

The above sections define the finite element code that will be used to investigate the wound healing process in *Drosophila* embryos.

Chapter 4
Results and Discussions

In this Chapter we use the finite element engine described earlier to investigate the forces that drive healing of a range of wound geometries including wounds having a variety of different initial geometries.

4.1 Edge Tensions as a Driving Force

There is strong evidence that interfacial tensions play a significant role in morphogenetic processes, such as sorting, neurulation (Brodland & Chen, 2000; Brodland, 2002). For this reason, the nature of motions driven by interfacial tensions will be examined in this section to see if they match those that occur in the wound healing process.

4.1.1 Experimental Data Results

The point wound experimental data was analyzed and the healing process is shown in Figure 4.1. The healing process occurred over a time period of approximately 850 seconds and varied slightly from one experiment to the next. In all cases similar significant cell movements and changes in shape occurred as healing progressed.

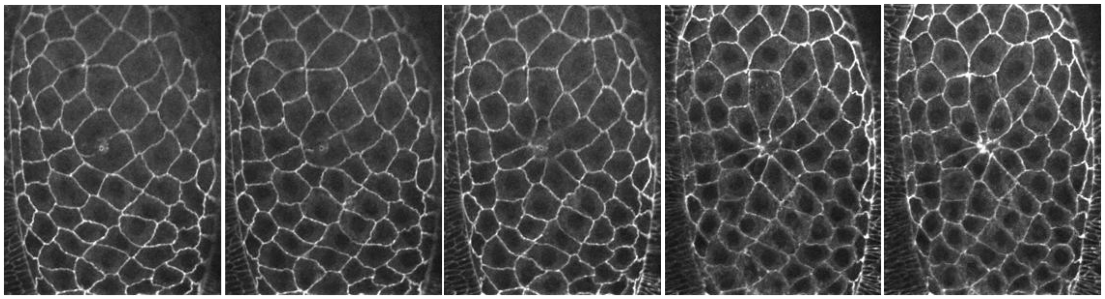

Figure 4.1 – Experimental data of point wound healing process

The width of the entire patch narrowed while its length remained relatively constant, resulting in the overall area of the patch decreasing. Narrowing occurs whether or not a wound exists. The wound cell had a non-circular geometry, the ring 1 cells tended to have a wedged geometry and the ring 2 cells elongated towards the wound. These characteristics can be quantified using the measures defined in Chapter 3 and are shown in Figure 4.2.

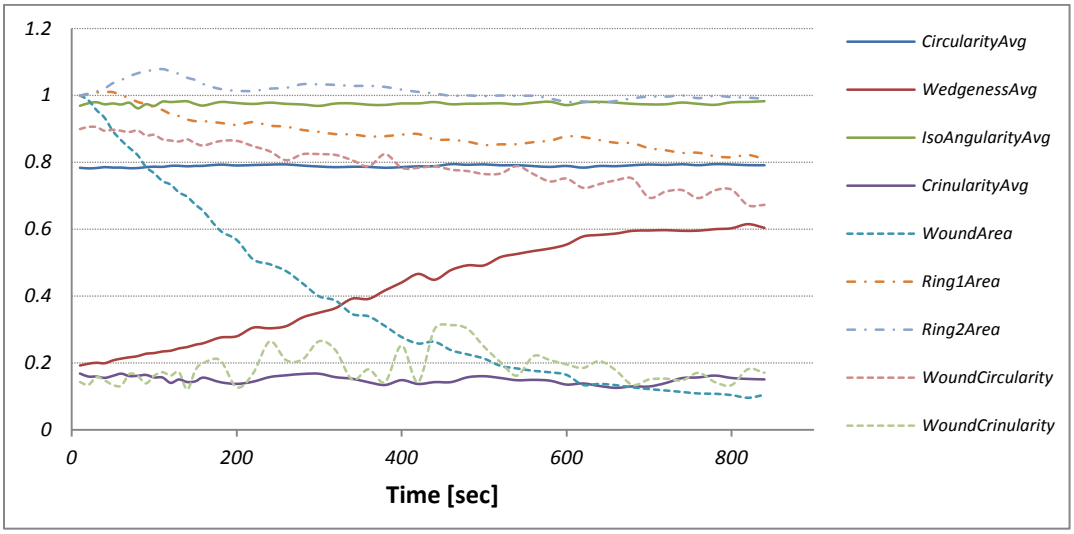

Figure 4.2 – Geometric parameters for point wound experimental data

Table 4.1 summarizes the parametric results, showing their initial and final values along with the percent change.

Table 4.1 – Geometric parameter results for point wound

Parametric Measure	Initial	Final	Percent Change [%]
Circularity Average	*0.7834*	*0.7913*	*1.0*
Wedgeness Average	*0.1922*	*0.6041*	*214.3*
Isoangularity Average	*0.9692*	*0.9830*	*1.4*
Crinularity Average	*0.1683*	*0.1508*	*-10.4*
Wound Area	*1.000*	*0.1052*	*-89.5*
Ring 1 Area	*1.000*	*0.8094*	*-19.1*
Ring 2 Area	*1.000*	*0.9897*	*-1.0*
Wound Circularity	*0.8992*	*0.6725*	*-25.2*
Wound Crinularity	*0.1430*	*0.1708*	*19.4*

4.1.2 Edge Tension Applied to All Edges

To understand how interfacial tensions contributed to the morphogenetic movements, edge tension of 0.5*dyne* were applied to a model patch of cells. For the simulation, a volume constant was applied to all of the cells, except for the wound cell. The forward simulation was conducted until equilibrium was reached and is shown in Figure 4.3. The time course of the geometric parameters is shown in Figure 4.4.

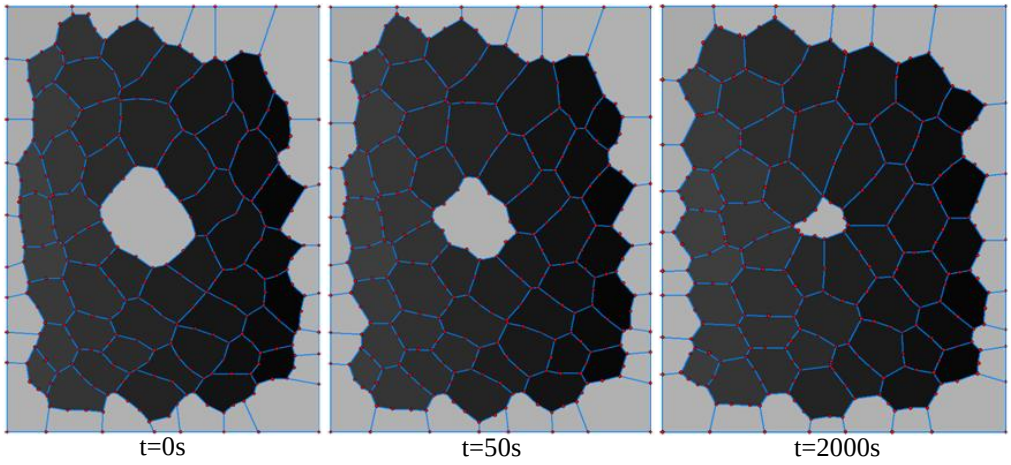

Figure 4.3 – Forward simulation of steady state with applied edge tensions

Most of the parametric measures reflected the experimental data measures with minor variations. The wound area and circularity decreased and the wedgeness increased, similar to the experimental data. Although the final values were not in agreement, their overall increasing and decreasing trends were similar. There were several differences when comparing the experimental data to the model simulation. One observation was that the shape of the cells tended to be circular. Also, Figure 4.4 showed a slight increase in the average isoangularity as the patch was annealed. The cell edges in the experimental data were crinkled in comparison to the annealed patch and this suggests that there were small or negligible edge tensions throughout the cell patch.

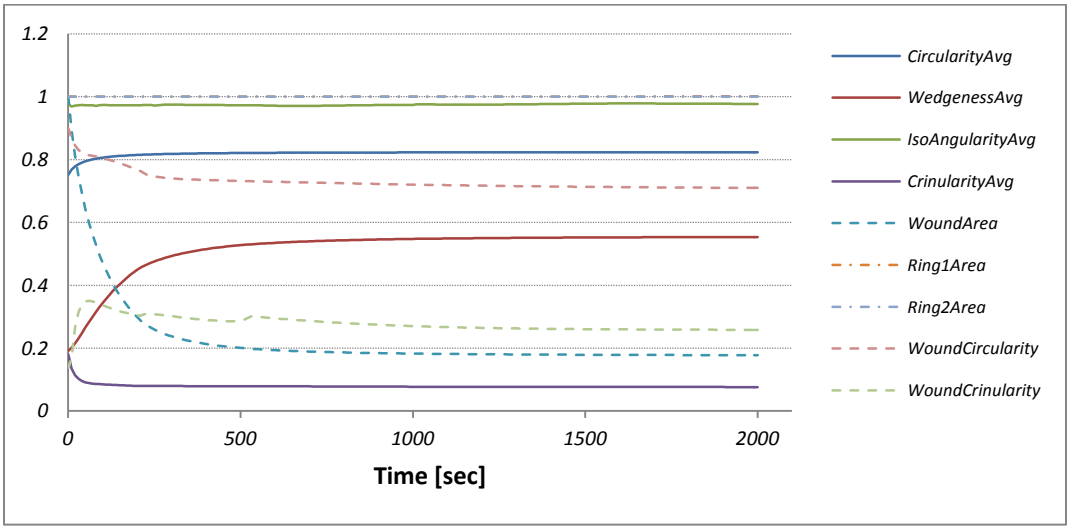

Figure 4.4 – Geometric parameters for a model tissue driven by edge tensions

Another distinction between the model patch and the experimental data was the difference in the individual cell sizes and the overall size of the patch. In the experimental data, there was a decreasing trend in the area of the cells. This suggested that the cells were losing volume. Despite the differences observed between the experimental and synthetic data, there were also similarities in terms of their parametric measures (see Table 4.2).

Table 4.2 – Geometric parameter comparison between experimental data and forward simulation (§4.1.2)

Parametric Measure	Steady State			Experimental Data
	Initial	Final	Percent Change [%]	Percent Change [%]
Circularity Average	*0.7834*	*0.8231*	*5.1*	*1.0*
Wedgeness Average	*0.1922*	*0.5537*	*188.1*	*214.3*
Isoangularity Average	*0.9692*	*0.9770*	*0.8*	*1.4*
Crinularity Average	*0.1683*	*0.0763*	*-54.7*	*-10.4*
Wound Area	*1.000*	*0.1776*	*-82.2*	*-89.5*
Ring 1 Area	*1.000*	*1.0008*	*0.1*	*-19.1*
Ring 2 Area	*1.000*	*0.9999*	*0.0*	*-1.0*
Wound Circularity	*0.8992*	*0.7098*	*-21.1*	*-25.2*
Wound Crinularity	*0.1430*	*0.2582*	*80.5*	*19.4*

Although the majority of the parametric measures were similar to the experimental data, there were noticeable discrepancies in the average crinularity, wound crinularity and the area of ring 1 cells. This suggests there were other forces present throughout the cell patch or that the edge tensions varied from one cell to another.

4.1.3 Purse String around Wound Cell

Studies have suggested that an actin purse string forms along the perimeter of the wound, producing high tonus forces and causing the wound to close. A forward simulation was conducted with the wound cell having a tonus force of 0.06*dyne*, and this situation was conducted for 850 seconds and is shown in Figure 4.5.

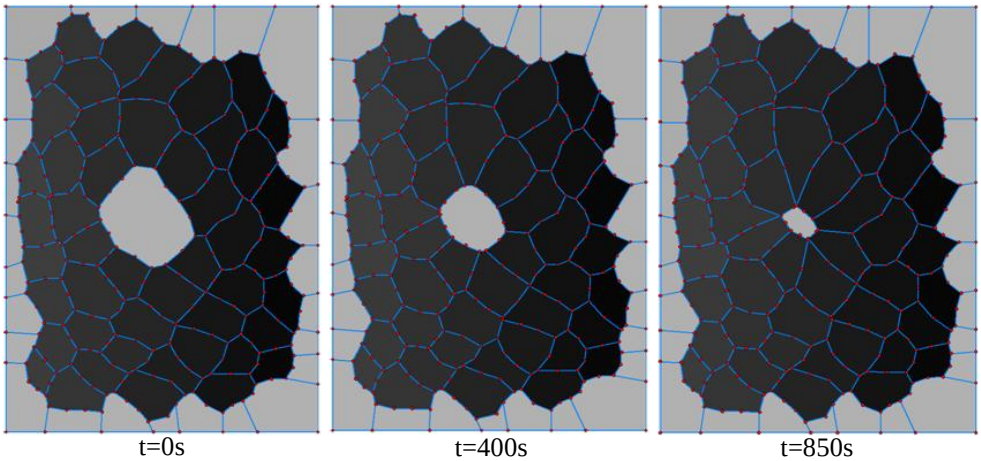

Figure 4.5 – Purse string around the wound cell

Lesion closure was greater when a purse string was applied around the wound. However, the cell sizes were noticeably smaller in the experimental data, suggesting that there was a lack of volume loss in the simulation. Despite having the same final wound area as the experimental data, the shape of the wound was circular in the simulation. There were also distinctions in the parametric measures as shown in Figure 4.6.

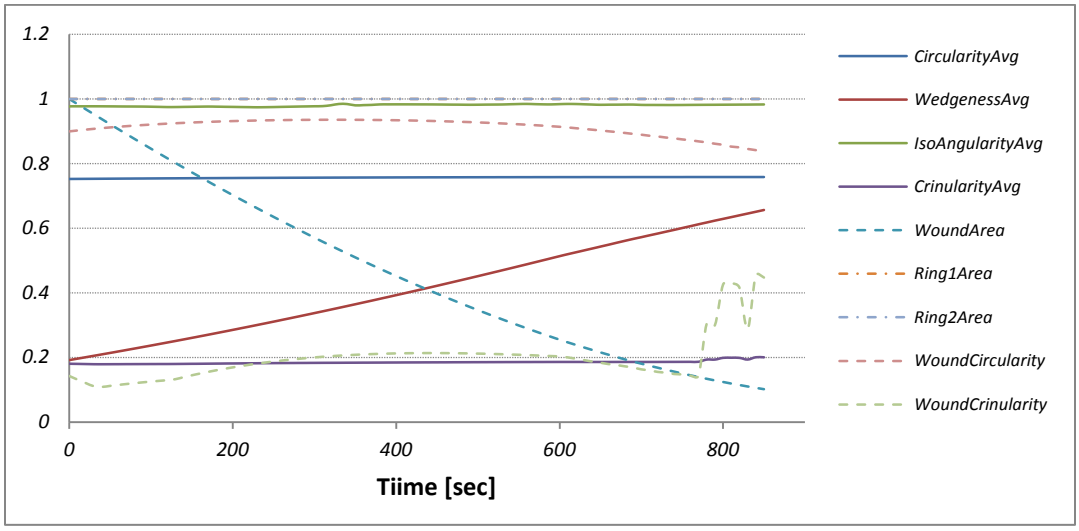

Figure 4.6 – Geometric parameters for a model tissue driven by a purse string around the wound cell

Towards the end of the simulation, the wound crinularity spiked. As the wound cell closed, the nodes overlapped and passed another node, which significantly increased the crinularity of the cell. This occurrence is not realistic, but is a numerical artifact. When observing the overall trend of the wound crinularity, the curve yielded a parabolic profile. Based on the Eq. (3.4), the crinularity of the cell increased as it deformed away from a straight line.

Applying a purse string around the wound closed the hole while increasing the wedgeness of ring 1 cells at a steady pace, similar to the experimental data. The data suggest that purse string contraction is a plausible driving force for lesion closure.

4.1.4 Purse String around Wound with Cell-to-Cell Permeability

We hypothesized that cell permeability might account for the differences between the model and experimental findings. In this study, the majority of the parameter results were similar to those in §4.1.3, however, the area profile for ring 1 cells was different compared to the experimental data. The area of ring 1 cells in the experimental data decreased as closure progressed. A simulation was conducted with cell-to-cell permeability set to a value of 10, except for the light (outside edge) cells. The simulation and the parametric measure results are shown in Figure 4.7 and Figure 4.8, respectively.

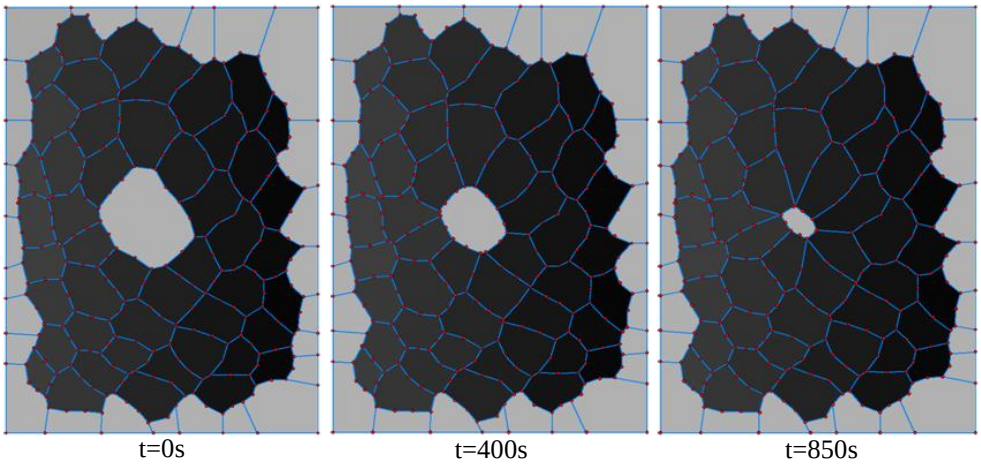

Figure 4.7 – Purse string around the wound cell with cell-to-cell permeability

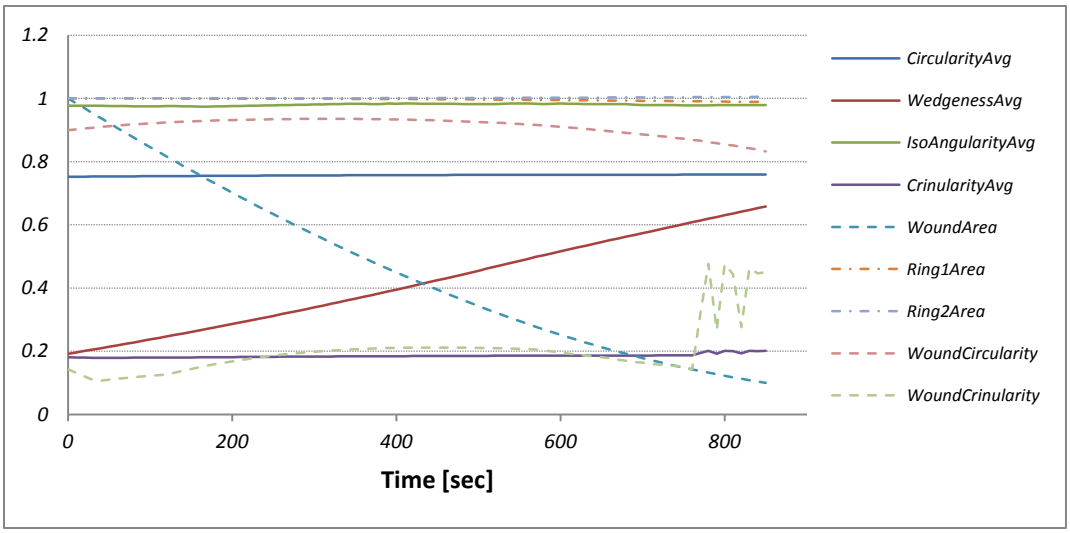

Figure 4.8 – Geometric parameters for a model tissue driven by a purse string around the wound cell with cell-to-cell permeability

The forward simulation results were similar to the simulation conducted in §4.1.3. The ring 1 cells lost very little fluid as a result of having cell-to-cell permeability, suggesting a purse string around the wound is not sufficient for ring 1 cells to lose their volume. To determine whether edge tensions alone can be used to reduce the volume in cells, a forward simulation with interfacial tensions throughout ring 1 cells was conducted. A purse string of 0.09*dyne* was applied to the wound cell, while the interfacial tension between ring 1 to ring 2 cells and ring 1 to ring 1 cells had an edge tension of 0.05*dyne*. The forward simulation and parametric results are shown in Figure 4.9 and Figure 4.10, respectively.

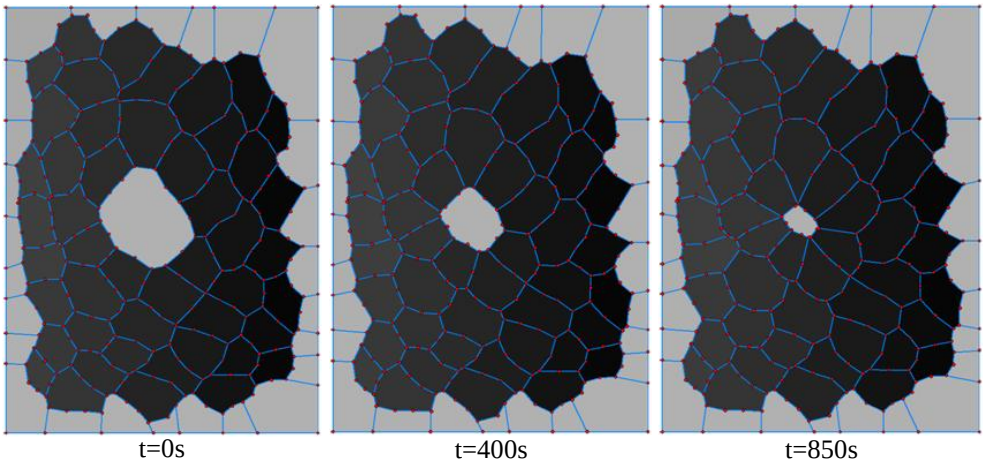

Figure 4.9 – Using edge tensions to simulate volume loss in ring 1 cells

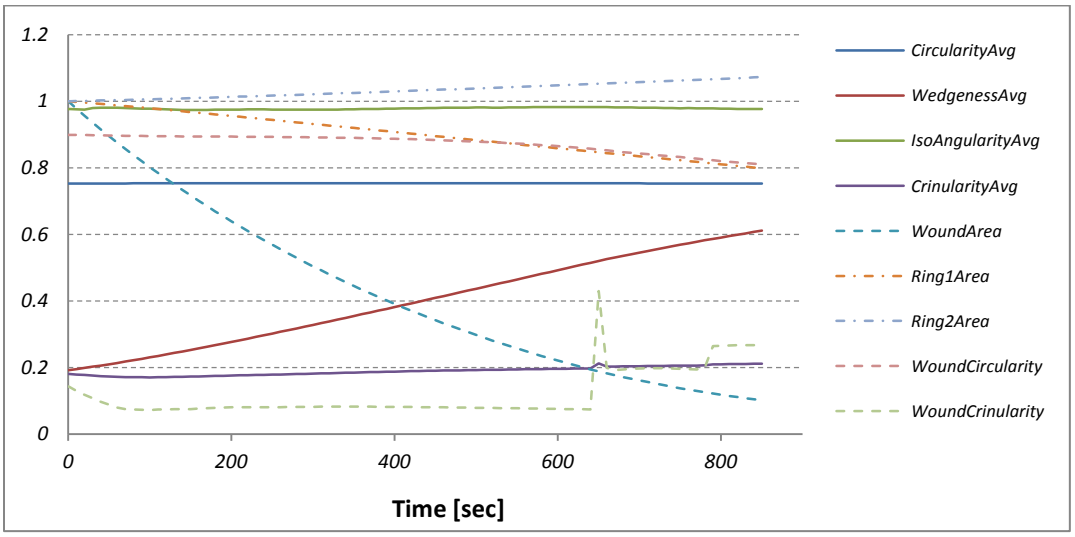

Figure 4.10 – Geometric parameters for a model tissue driven by edge tensions to simulate volume loss in ring 1 cells

Although the area of ring 1 cells decreased, the shape of the cells was different from the experimental data. The ring 1 cells were round in the simulation, whereas cells in the experimental data were noncircular. In the forward simulation, the ring 1 cells decreased in area, while ring 2 cells increased in area. Increasing the tonus force throughout ring 1 cells increased the pressure of the ring 1 cells, and created a pressure gradient between neighbouring cells. Consequently, the pressure difference forced the fluid to transfer from ring 1 cells to its neighbouring cells, wound cell and ring 2 cells. This suggests that other forces were responsible for decreasing the area of the cells and interfacial tensions alone do not produce wound healing. However, a purse string around the wound may still generate important driving forces.

4.2 Local Area Contractions as a Driving Force

In Chapter 3, two different types of cell contraction models were developed, the nodal-based and the pressure-based. In this section, both contraction models will be investigated.

4.2.1 Nodal-Based Contraction Parameter Determination

As the individual cells underwent contraction, cells that were closer to the wound lost more volume as healing progressed. Figure 4.11 depicts this process.

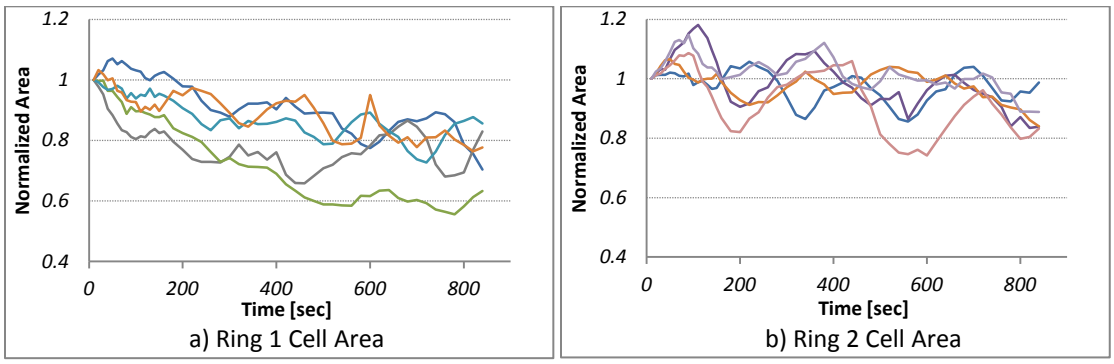

Figure 4.11 – a) Areas of a few ring 1 cells versus time. A decrease in area can be observed as healing progresses. b) Areas of a few ring 2 cells versus time. A very small decrease in area compared to ring 1 cells can be observed as healing progresses.

The cells underwent approximately four contraction cycles over the duration of the healing process. Having obtained the experimental data parameters, a forward simulation was conducted using the nodal-based contraction and a volume pressure of $10 dyne/pixel^2$. The contraction parameters were tuned to match the experimental data, giving contraction rate, strength and duration values of 0.6%, $0.15 dyne$ and $180 sec$, respectively. Figure 4.12 shows an example of cells undergoing contraction.

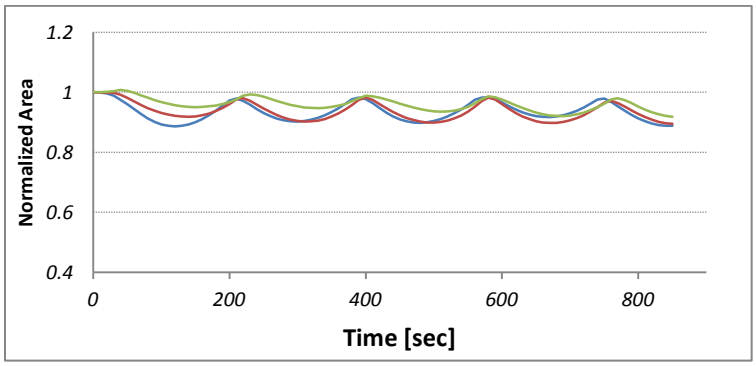

Figure 4.12 – Three samples of cell area undergoing nodal-based contraction

The contraction cycle and magnitude of cell in the simulation resembled the experimental data. However, cell contraction was not sufficient to drive the cells to lose their volume. There were also variations when comparing the forward simulation and experimental data. Figure 4.13 shows the cell patch at 500 seconds into the simulation.

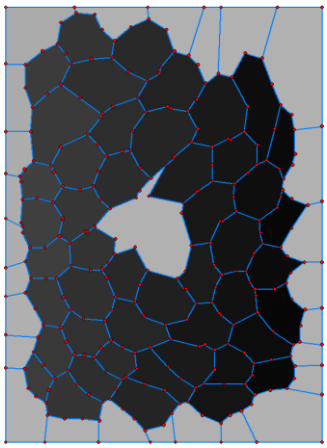

Figure 4.13 – Nodal-based contraction simulation

The cell shapes were distorted when the nodal-based contraction model was used. Since the wound cell did not have any resisting force or pressure, the cells bordering the wound were vulnerable to deformation. In addition, the cells became circular during the contraction and retained their circular shape even after the contraction was completed.

4.2.2 Nodal-Based Contraction as a Driving Force

To determine whether the nodal-based local area contraction could cause the wound cell to close, a forward simulation was conducted with cell contraction as the only driving force. The forward simulation and parametric results are shown in Figure 4.14 and Figure 4.15, respectively.

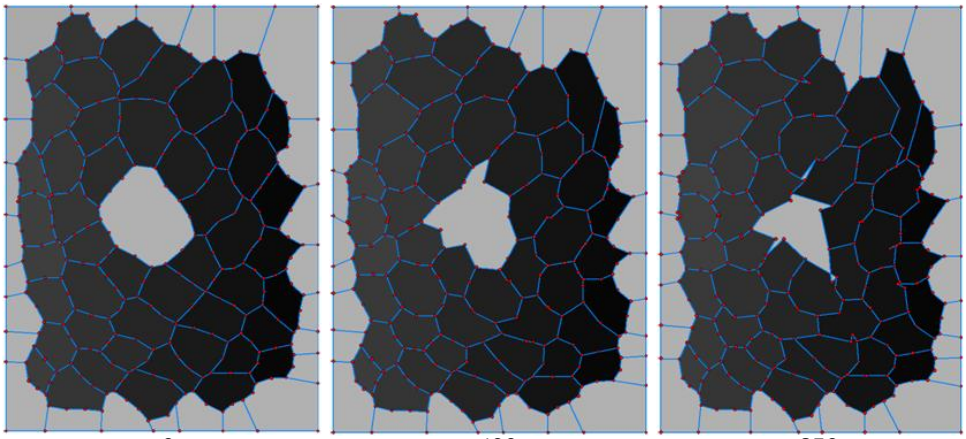

Figure 4.14 – Nodal-based contraction as a driving force simulation

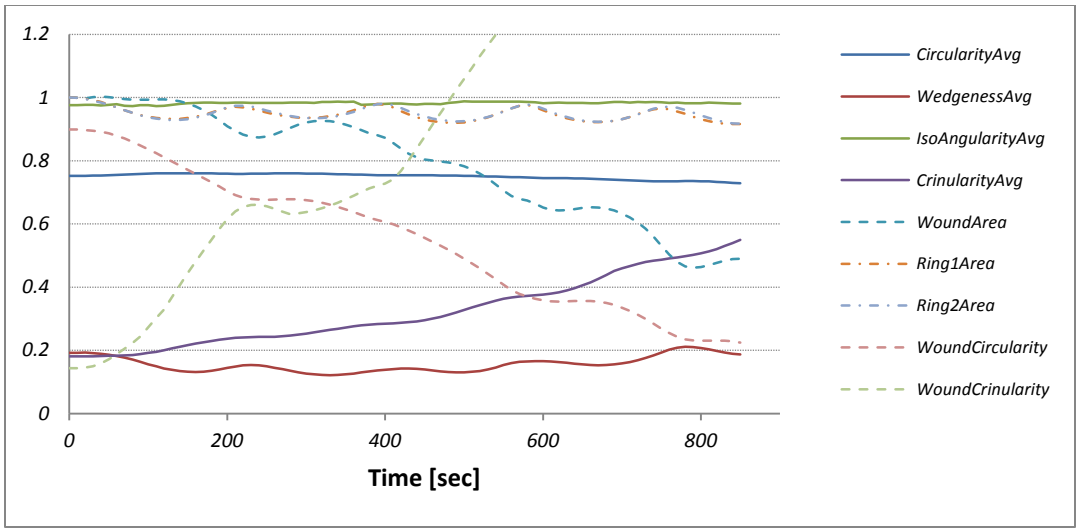

Figure 4.15 – Geometric parameters for a model tissue driven by nodal-based contraction

In the simulation, the circularity of the wound decreased, while the wound crinularity increased drastically. This suggested that a purse string around the wound was required for the wound to maintain its circular geometry. Further simulations indicated that the use of cell-to-cell permeability had no effects on the volume loss in ring 1 cells. The area changes in cells were dominated by pressure rather than the cell-to-cell permeability. In addition, the wedgeness of ring 1 cells did not increase because the contraction forced the cells to roundup, preventing the cells from forming a wedged shape. Overall, the nodal-based contraction model did not yield similar results to the experimental data.

4.2.3 Nodal-Based Contraction with Edge Tensions

The forward simulation conducted in §4.2.2 demonstrated that wound closure could not be achieved using only nodal-based contractions. Although the area of the wound cell decreased, it did not match the experimental data. Thus, the nodal-based contraction was used in conjunction with edge tensions to simulate wound closure.

A forward simulation was conducted with a purse string around the wound in addition to the cell contractions. The simulation demonstrated that wound closure can be accomplished while increasing the wedgeness of the cells. Unfortunately, other parametric measures were not reflective of the experimental data, such as the wound shape and the area of ring 1 cells. To reduce the area of ring 1 cells, an interfacial tension was applied throughout ring 1 cells. While the area of ring 1 cells was reduced, it was not reflective of the experimental data. The simulation and parametric results are shown in Figure 4.16 and Figure 4.17, respectfully.

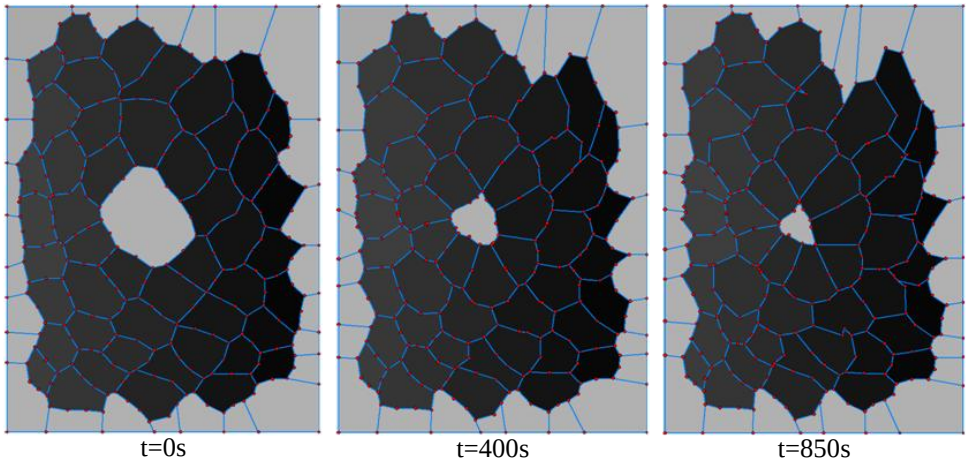

Figure 4.16 – Nodal-based contraction with edge tensions

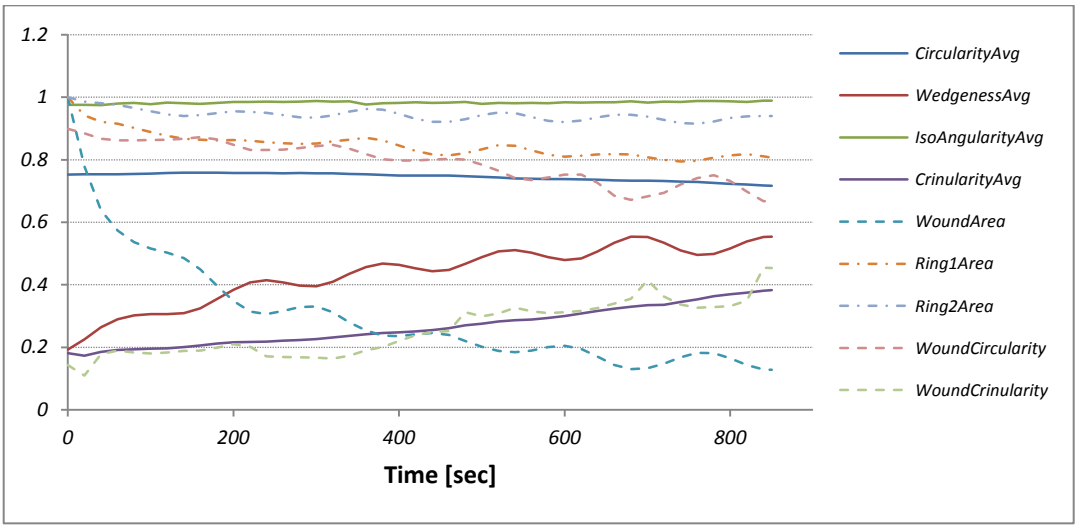

Figure 4.17 – Geometric parameters for a model tissue driven by nodal-based contraction and edge tensions

In §4.1.4, a similar study was conducted without the presence of contractions. When comparing the magnitude of the edge tensions required to achieving the same area for wound cell and ring 1 cells, only half was required for the patch that had nodal-based cell contractions. This suggested that the nodal-based contraction model encouraged lesion closure, allowing a smaller purse string to accomplish wound closure. Although most of the parametric measures were in agreement with the experimental data, the final configuration of the cells was not reflective of the experimental data. The cell contractions and edge tensions were not sufficient to capture the wound healing phenomena. Based on the simulations conducted thus far, the nodal-based cell contraction is deemed an unviable model; the shape of the cells was noticeably affected by the contraction and did not reflect the experimental data.

4.2.4 Pressure-Based Contraction Parameter Determination

Through an iterative process, pressure-based contraction control parameters resembling the experimental data were obtained. The contraction rate, strength and duration were determined to be 0.1%, 0.01*dyne/pixel*^{2} and 150*sec*, respectively. Figure 4.18 shows an example of cells undergoing pressure-based area contractions.

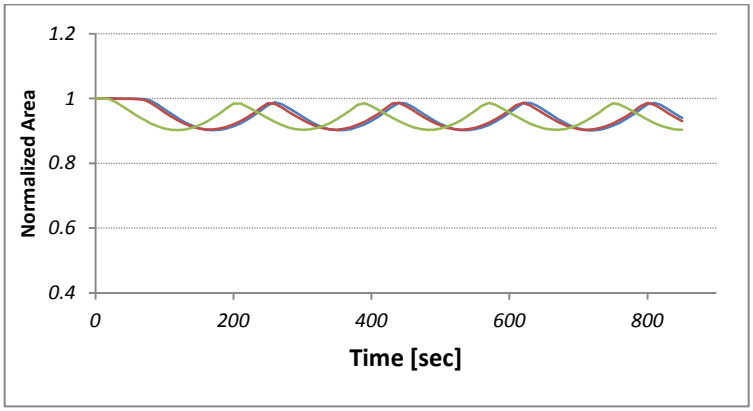

Figure 4.18 – Three samples of cell area undergoing pressure-based contraction

The area profile of the pressure-based contractions was similar to the nodal-based contraction results. The pressure-based contraction was not able to decrease the area of the cells, but proved robust in maintaining their shapes. Figure 4.19 shows the simulation results.

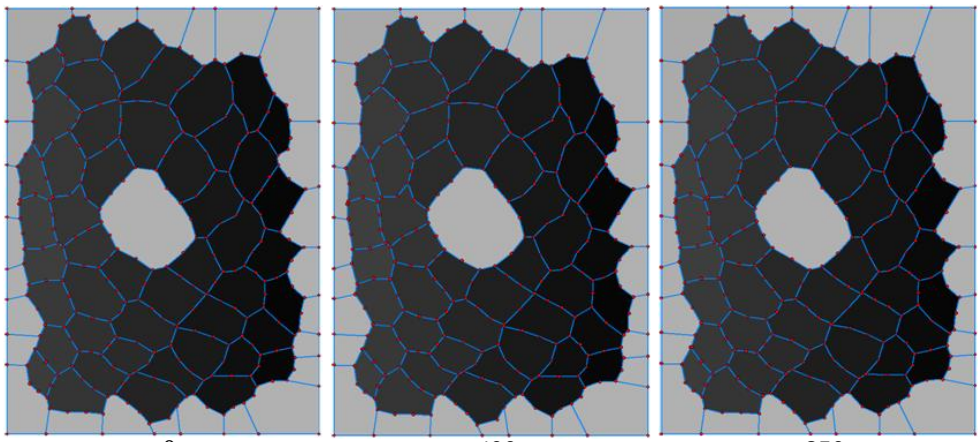

Figure 4.19 – Pressure-based contraction simulation

When comparing the simulation to the experimental data, the pressure-based contraction yielded similar results in terms of their cell shapes. The wound cell was able to maintain its distinctive shape while the surrounding cells contracted.

4.2.5 Pressure-Based Contraction as a Driving Force

The pressure-based local area contraction model proved to be more reliable in conducting forward simulations. The parametric measures of the pressure-based contraction simulation are shown in Figure 4.20.

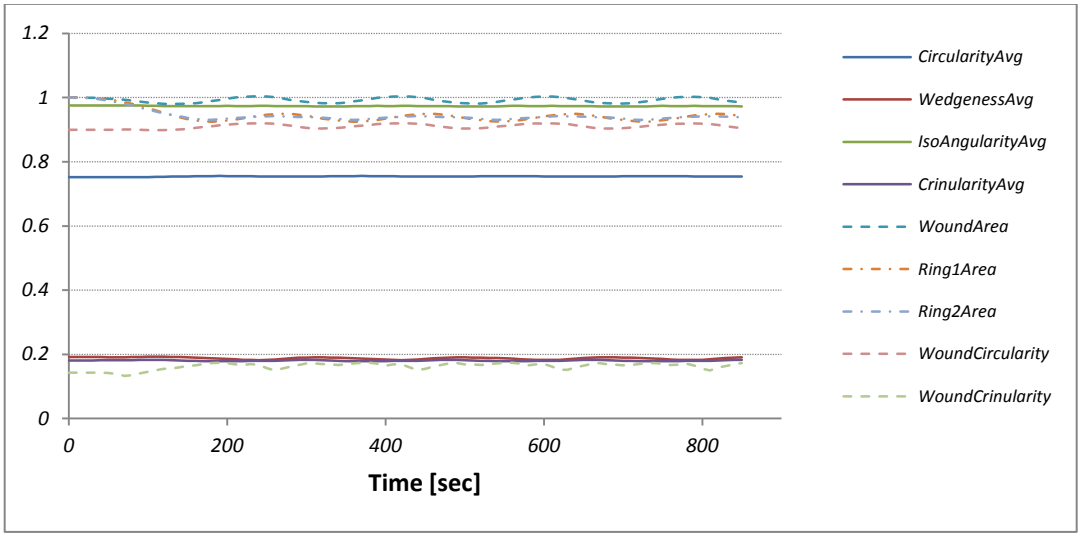

Figure 4.20 – Geometric parameters for a model tissue driven by pressure-based contraction. The parametric measures are not affected by local contractions.

The pressured based contraction simulation was unable to drive wound closure. In fact, there were little changes to the parametric measure results. The cells that were in contraction oscillated while maintaining a steady average value. When the pressure-based contraction was biased towards different cell types, it was still difficult to achieve lesion closure. The simulation and parametric results, causing ring 1 cells to contract, are shown in Figure 4.21 and 4.22, respectively.

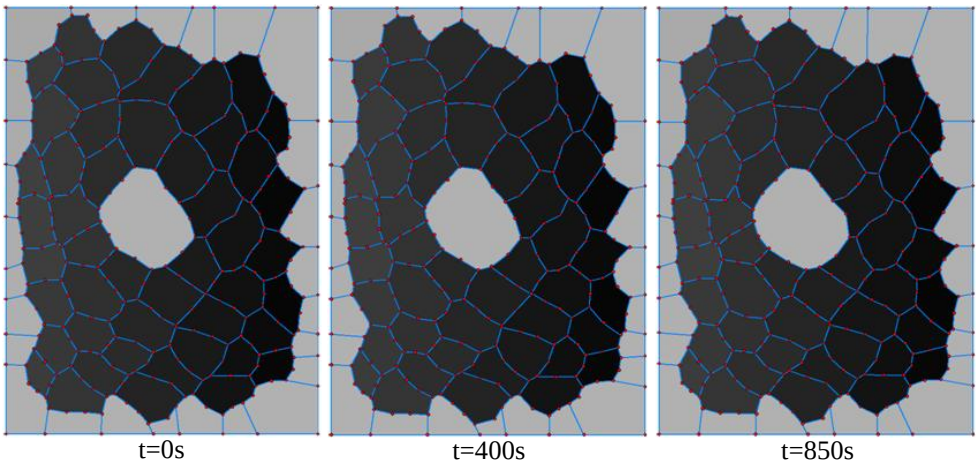

Figure 4.21 – Pressure-based contraction simulation

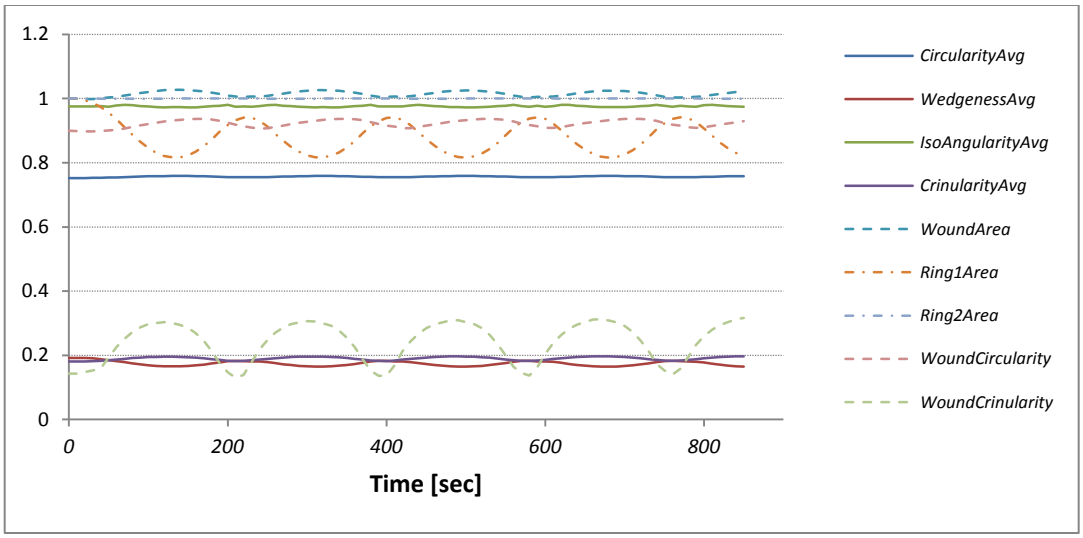

Figure 4.22 – Geometric parameters for a model tissue driven by a biased pressure-based contraction

Despite causing ring 1 cells to contract, the wound was not able to close. When analyzing the parametric results, the area of ring 1 cells reduced at the start of the simulation; once the pressure was stabilized, the contraction progressed. Other parametric measures did not change, but rather remained constant or in oscillation.

4.2.6 Pressure-Based Contraction with Edge Tensions

The pressure-based contraction was used in conjunction with a purse string around the wound to simulate lesion closure. A tonus force of 0.055*dyne* was applied around the wound and the simulation result is shown in Figure 4.23.

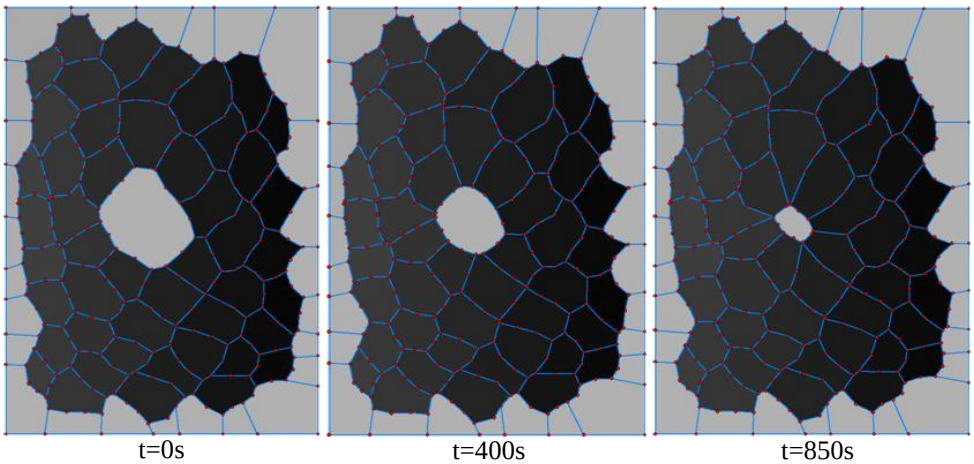

Figure 4.23 – Pressure-based contraction with edge tensions

The final configuration of the cell patch yielded results slightly different from the experimental data but proved to be the most comparable simulation thus far (see Table 4.3). The main difference between the forward simulation and the experimental data was that the experimental data held a distinctive "U" shaped wound whereas the forward simulation had an oval shaped wound. The parametric measure results are shown in Figure 4.24.

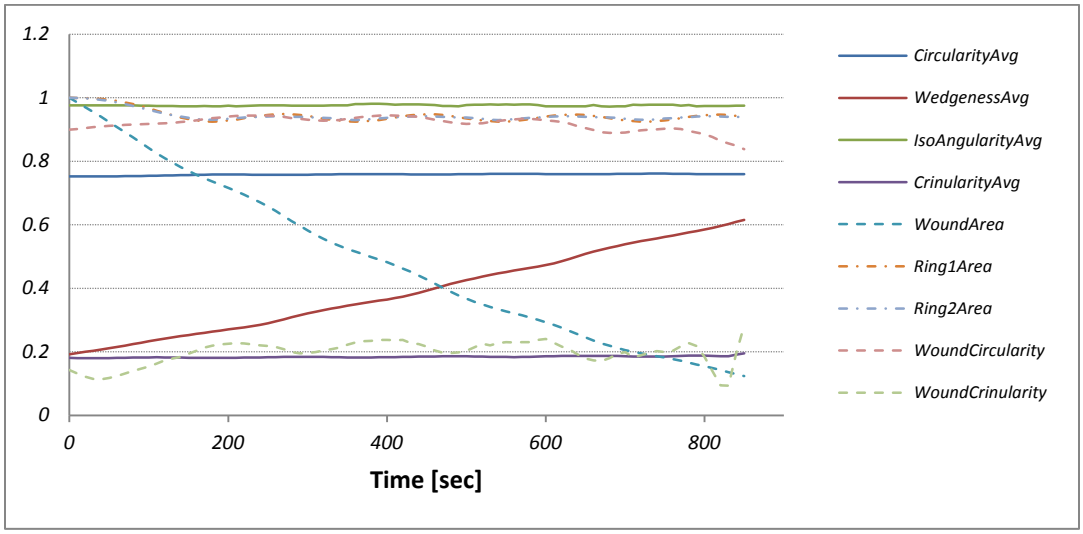

Figure 4.24 – Geometric parameters for a model tissue driven by pressure-based contraction and edge tensions

Table 4.3 – Geometric parameter comparison between experimental data and forward simulation (§4.2.6)

Parametric Measure	Simulation			Experimental Data
	Initial	Final	Percent Change [%]	Percent Change [%]
Circularity Average	*0.7834*	*0.7598*	*-3.1*	*1.0*
Wedgeness Average	*0.1922*	*0.6155*	*220.2*	*214.3*
Isoangularity Average	*0.9692*	*0.9748*	*0.6*	*1.4*
Crinularity Average	*0.1683*	*0.1953*	*16.0*	*-10.4*
Wound Area	*1.000*	*0.1238*	*-87.6*	*-89.5*
Ring 1 Area	*1.000*	*0.9400*	*-6.0*	*-19.1*
Ring 2 Area	*1.000*	*0.9386*	*-6.1*	*-1.0*
Wound Circularity	*0.8992*	*0.8381*	*-6.8*	*-25.2*
Wound Crinularity	*0.1430*	*0.2831*	*98.0*	*19.4*

The final value of the wedgeness and wound cell area were in close proximity with the experimental data, but there were differences in the slope curvatures. In the experimental data, the wound area and wedgeness leveled out towards the end of the healing process whereas the forward simulation showed a constant rate of change. This suggested that the patch was reaching equilibrium, or the forces were changing throughout the healing process. In attempt to model the decreasing trend in area of ring 1 cells, simulations were conducted having permeable cells and interfacial tensions throughout ring 1 cells. Unfortunately, the simulation results were similar to the nodal-based contraction, conducted in §4.2.3; it was difficult to reduce the area of ring 1 cells through edge tensions and permeability.

4.3 Far-Field Stress (FFS) as a Driving Force

Laser ablation experiments have suggested that the entire amnioserosa is under tension during the healing process. In this section, we add far-field stresses (FFS) as potential driving forces.

4.3.1 FFS as a Driving Force

The effect of the far-field stress was simulated by applying tensile stresses along the rectangular boundary of the patch. A far-field stress of 0.001*dyne/pixel*^{2} in the x and y direction was applied and the simulation and parametric results are shown in Figure 4.25 and Figure 4.26, respectively.

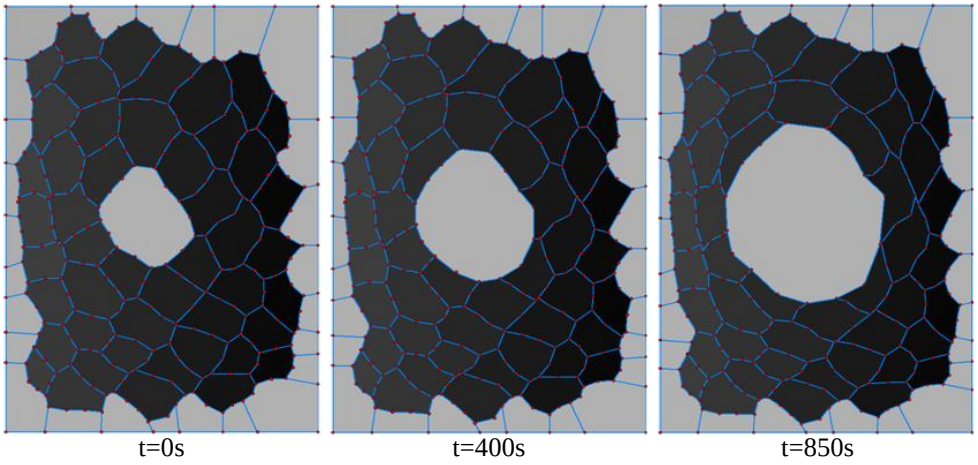

Figure 4.25 – FFS simulation

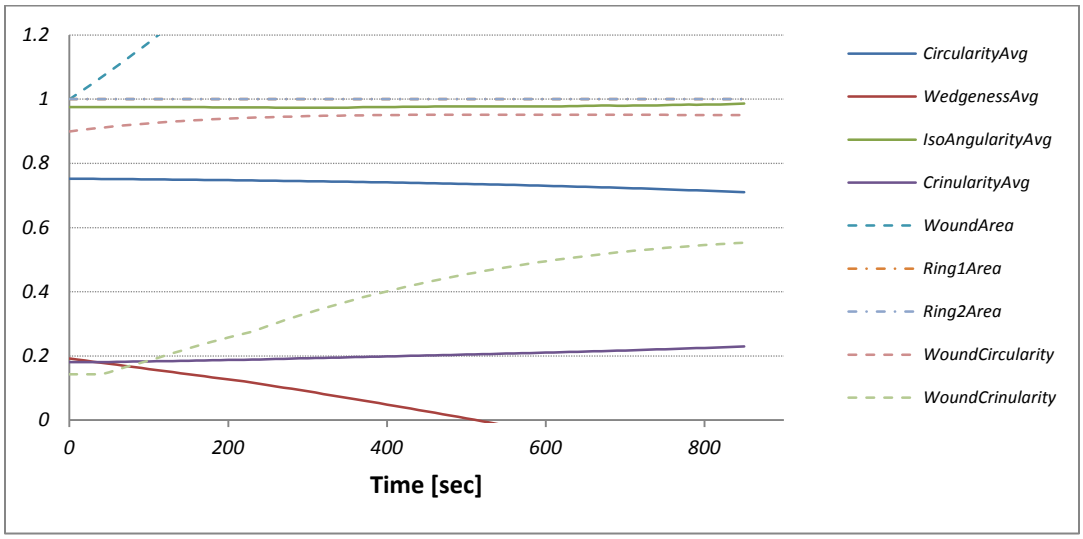

Figure 4.26 – Geometric parameters for a model tissue driven by FFS

Applying a far-field stress expanded the wound, since the wound was unconstrained in its volume. When the simulation was compared to the experimental data, the simulation captured the early stages (right after the point of ablation) of the recoiling phenomena and did not contribute to the healing process. In fact, it increased the wound area, confirming studies suggesting that it acts as a resisting force. To achieve wound closure, the far-field stress has to be overcome by other forces responsible for driving lesion closure.

4.3.2 FFS with Edge Tensions

A forward simulation was conducted with a purse string around the wound, while the far-field stress acted against wound closure. The purse string around the wound had to be large enough to overcome the far-field stress. A purse string force of 0.09*dyne* was applied to the wound cell and the simulation was conducted for 850 seconds. The simulation and parametric measure results are shown in Figure 4.27 and Figure 4.28, respectively.

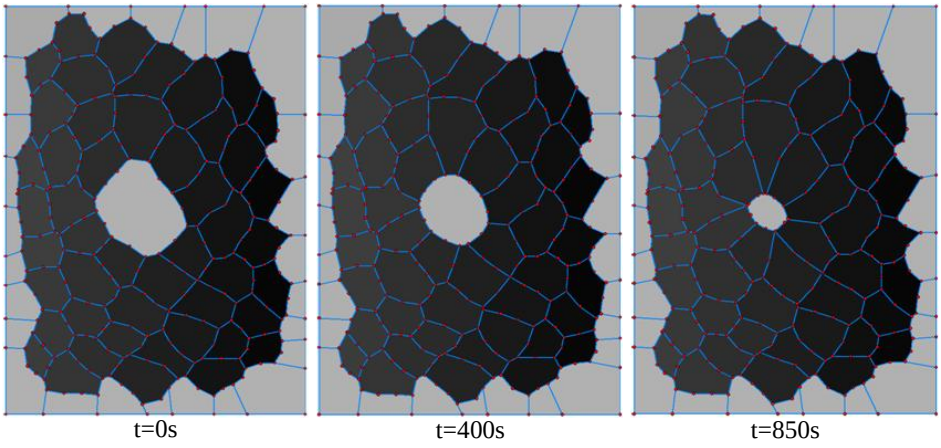

Figure 4.27 – Far-field stress with purse string

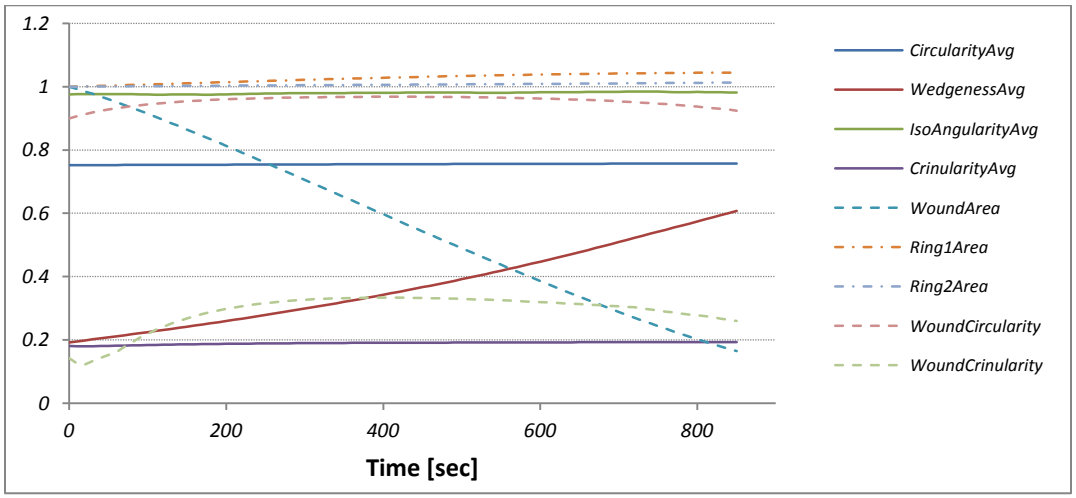

Figure 4.28 – Geometric parameters for a model tissue driven by FFS and a purse string

Despite the presence of a far-field stress, the wound was able to close, which was similar to the experimental data. However, other parametric measures, such as wound circularity, ring 1 area and ring 2 area differed from the experimental data. The purse string around the wound was strong and caused the wound cell to round up. The far-field is present in the amnioserosa throughout the healing process; other forces would be required to decrease the wound circularity, ring 1 area and ring 2 area.

4.4 Velocity Boundary Condition (BC) as a Driving Force

4.4.1 Velocity Boundary Condition (BC)

A forward simulation was conducted to determine the contribution of native dorsal closure to wound healing. A velocity of 0.034 and 0.0068*pixel/sec* was applied to the boundary for the x and y component, respectively, while other forces and constraints, such as edge tension, permeability and contraction were not applied to the patch. Figure 4.29 shows the simulation results.

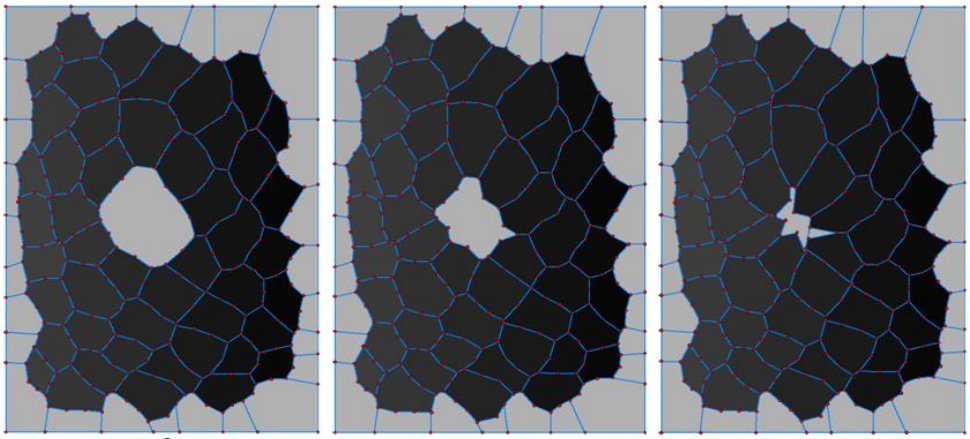

Figure 4.29 – Velocity BC simulation

The simulation showed that the native dorsal closure was able to drive wound closure. Although the area of the wound decreased, other parametric measures, shown in Figure 4.30, were not in agreement with the experimental data.

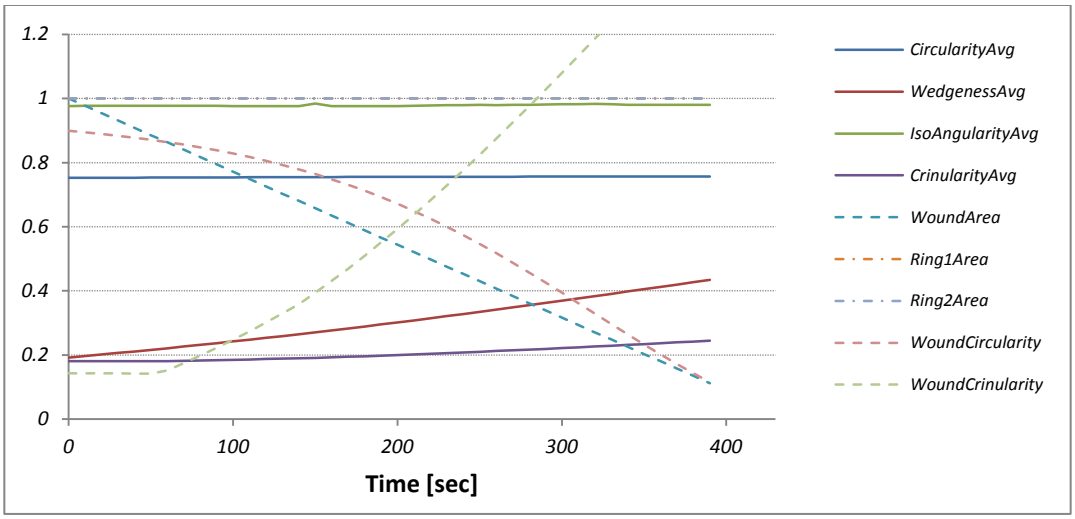

Figure 4.30 – Geometric parameters for a model tissue driven by velocity BC

The forward simulation was setup to run for 850 seconds, but wound closure was achieved at 400 seconds into the simulation. In the experimental data, the cells were losing sufficient amount of fluid, which allowed the wound to decrease over the duration of 850 seconds. Hence, other forces and constraints would be required to prolong the closure of the wound. Although there were differences in the simulation to the experimental data, the native dorsal closure of the amnioserosa cells proved to be sufficient in driving wound closure.

4.4.2 Velocity Boundary Condition (BC) with Edge Tensions

To more closely mimic dorsal closure, a simulation was conducted with permeable cells and a purse string around the wound. A tonus force of 0.03*dyne* was applied around the wound to reduce the crinularity of the wound, while a cell-to-cell permeability of 10 was applied to all the cells. Figure 4.31 shows the simulation results.

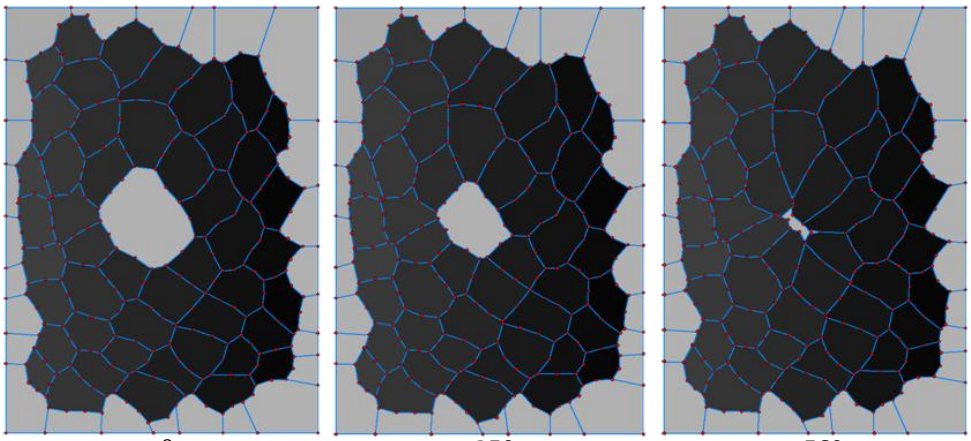

Figure 4.31 – Velocity BC with edge tensions at 560 seconds

The forward simulation was able to run longer with the presence of a purse string around the wound cell, in addition to the cells being permeable. When comparing the parametric measures, shown in Figure 4.32, the characteristics of the wound and the area of ring 1 cells did not match the experimental data.

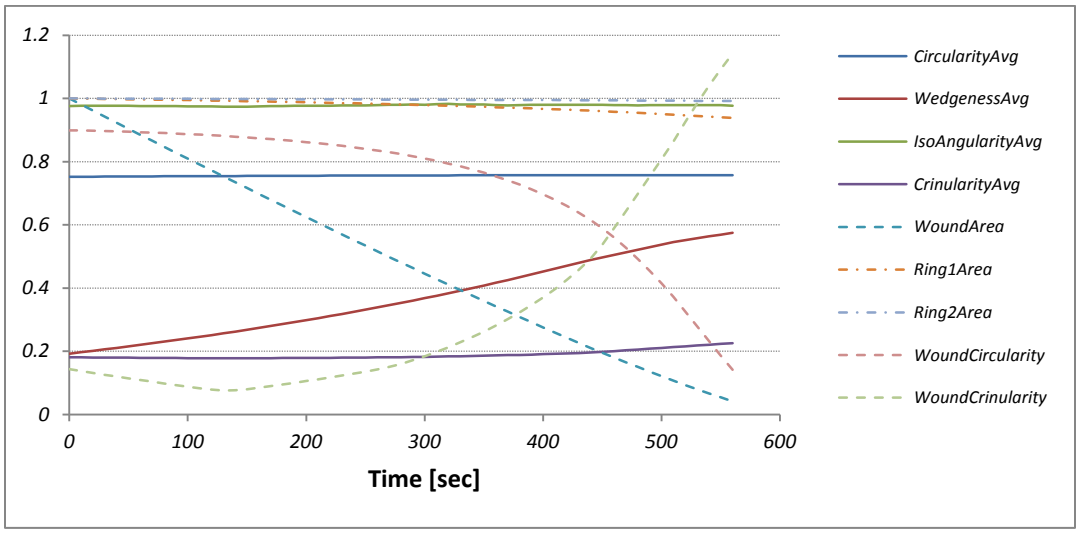

Figure 4.32 – Geometric parameters for a model tissue driven by velocity BC and edge tensions

Although the area of ring 1 cells decreased, an additional 15% reduction is required to resemble the experimental data. It was becoming evident that other forces were responsible for the cells to lose their volume. The velocity boundary condition required more than edge tensions and permeability to resemble the experimental data.

4.4.3 Velocity Boundary Condition (BC) with Edge Tensions and Contractions

Previous cell contraction simulations demonstrated the nodal-based contraction as an unviable contraction model. As a result, a simulation was conducted using the pressure-based contraction with the velocity boundary condition. Through an iterative approach, lesion closure resembling the experimental data was simulated. The simulation ran for 850 seconds and is shown in Figure 4.33. The following control parameters were used for the simulation:

Edge tension around wound = 0.045dyne
Volume Pressure = 10dyne/pixel^2
Velocity BC in x = 0.034pixel/sec
Velocity BC in y = 0.0068pixel/sec
Contraction Rate = 0.1%
Contraction Strength =0.01dyne/pixel^2
Contraction Duration = 150sec

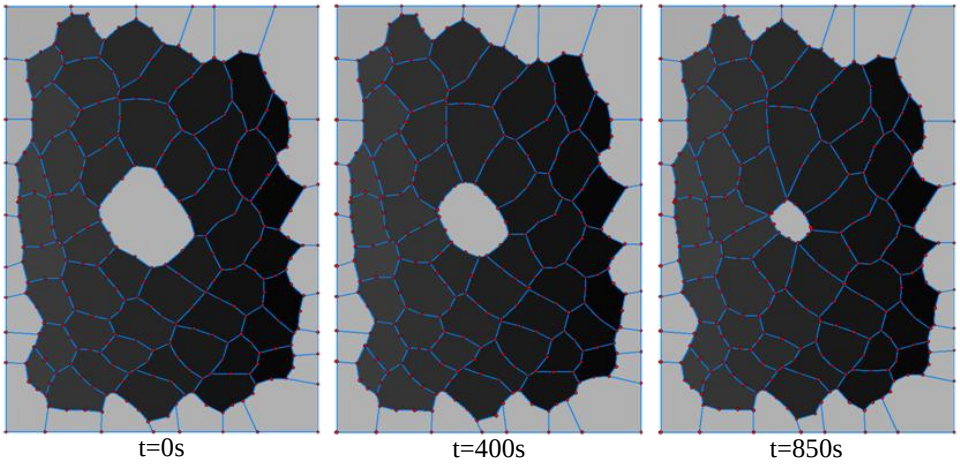

Figure 4.33 –Velocity BC with edge tensions and pressure-based contraction

The simulation yielded similar results to §4.2.6, where the pressure-based contractions were used in conjunction with edge tensions. The velocity boundary condition had a minor effect on the parametric measures, shown in Figure 4.34. Comparing the wound circularity and crinularity between the simulations revealed that the overall trends were similar despite the small differences in the deformed shape of the wound cell.

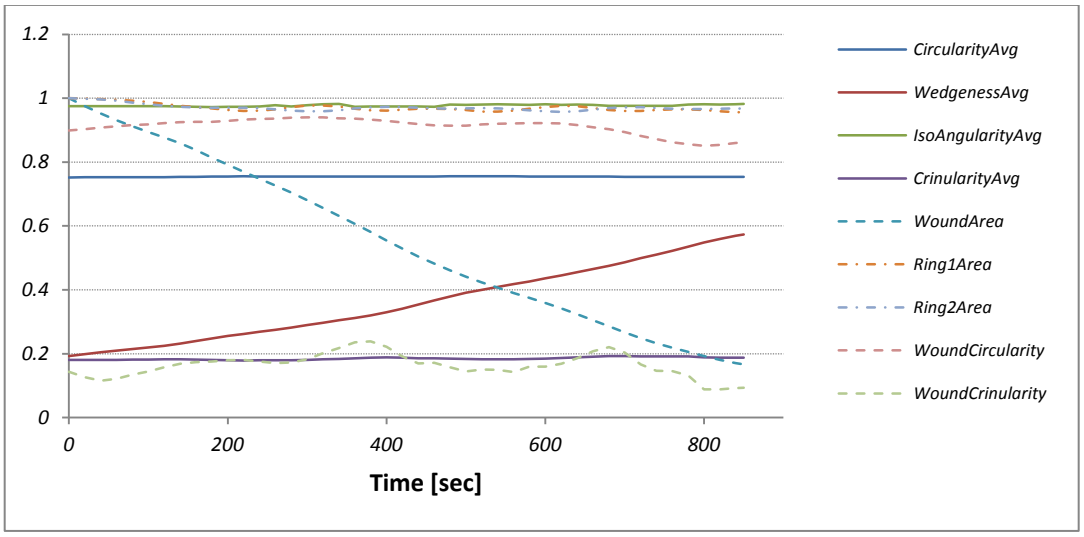

Figure 4.34 – Geometric parameters for a model tissue driven by velocity BC, edge tensions and pressure-based contraction

In both cases, the area loss in ring 1 cells was not sufficient enough to match the experimental data. The inability to lose fluid in ring 1 cells suggests that there were other forces that played an integral part in the healing process.

4.5 Apical Tension as a Driving Force

The increase in wound size increases the force imbalance between the apical tension and far-field stress. As a result, the amnioserosa cells that are exposed to larger wounds tend to show a higher loss in area. The reduction of the area is less severe in the case of a point wound in comparison to a bigger wound, such as a circular or line wound. Figure 4.35 shows the initial and final geometry of a point wound and circular wound.

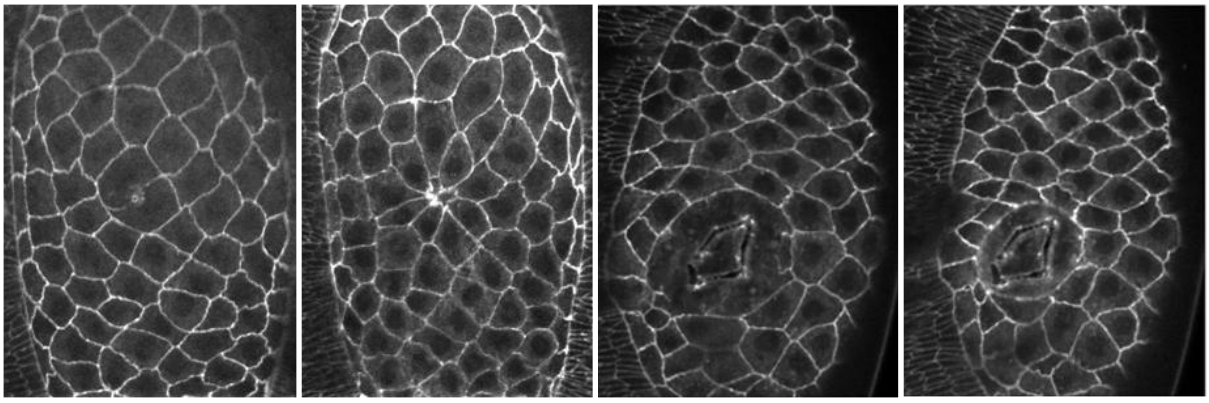

a) b) c) d)

Figure 4.35 – a) The first frame of the Point Wound experimental data. b) The last frame of the Point Wound experimental data. c) The first frame of Circular Wound 1 experimental data. d) The last frame of the Circular Wound 1 experimental data.

Comparing the two experiments revealed that ring 1 cells reduced in their area more severely for the circular wound. In addition, a noticeable amount of fluid was lost in ring 2 cells for the circular wound. Through digitizing the images, the area profiles of point and circular wounds were obtained and are shown in Figure 4.36.

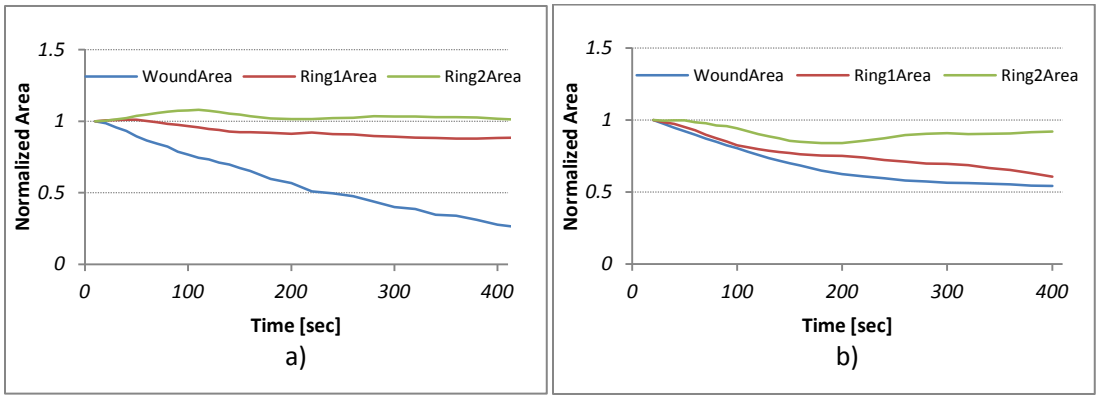

Figure 4.36 – a) Area profiles for Point Wound experimental data. b) Area profiles for Circular Wound 1 experimental data.

The circular wound took a longer time to heal than the point wound, and a higher loss in volume was observed in ring 1 and ring 2 cells in the circular wound. Hence, the Circular Wound 1 experiment was used for conducting apical force analysis.

4.5.1 Experimental Data Results and Apical Tension Parameter Determination

As the area of ring 1 and ring 2 cells decreased, the cells maintained its characteristic shapes (see Figure 4.35, c) and d)). The application of apical tension force requires an apical permeability constant to allow the area of the cells to decrease. Without the use apical permeability, the volume constraint on the cells prevents the cells from losing their volume. The parametric results for Circular Wound 1 experiment are shown in Figure 4.37.

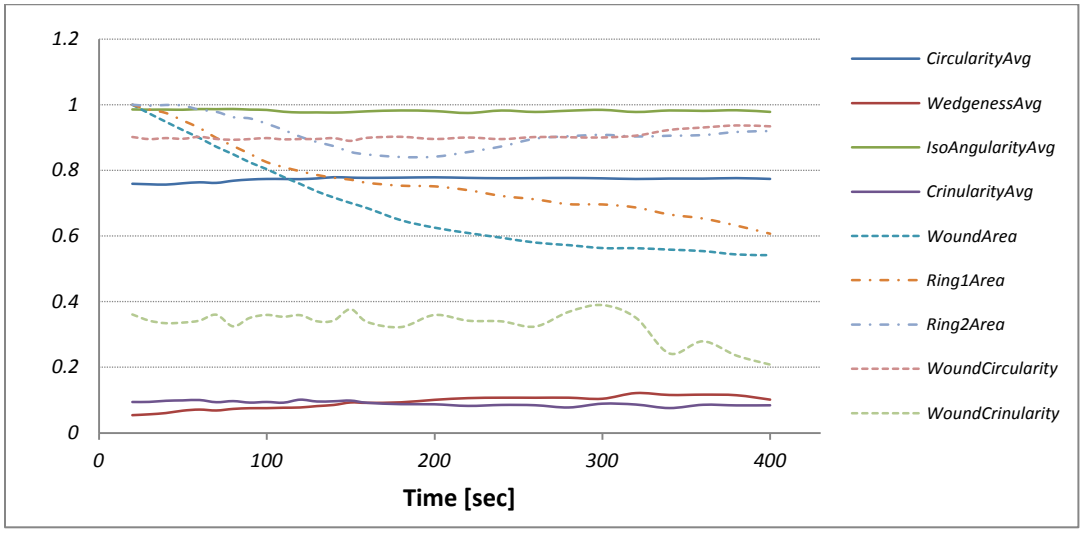

Figure 4.37 – Geometric parameters for Circular Wound 1 experimental data

The parametric measures were obtained over the duration of 400 seconds. Comparing the results between the point wound and circular wound experiment, shown in Table 4.1 and 4.4, respectively, revealed that the circular wound experiment had a larger area loss for ring 1 and ring 2 cells.

Table 4.4 – Geometric parameter results for Circular Wound 1

Parametric Measure	Initial	Final	Percent Change
Circularity Average	*0.7595*	*0.7740*	*1.9*
Wedgeness Average	*0.0543*	*0.1012*	*86.4*
Isoangularity Average	*0.9862*	*0.9784*	*-0.8*
Crinularity Average	*0.0945*	*0.0843*	*-10.8*
Wound Area	*1.000*	*0.5417*	*-45.8*
Ring 1 Area	*1.000*	*0.6075*	*-39.3*
Ring 2 Area	*1.000*	*0.9197*	*-8.0*
Wound Circularity	*0.9015*	*0.9342*	*3.6*
Wound Crinularity	*0.3612*	*0.2081*	*-42.4*

The wedgeness of ring 1 cells for the circular wound experiment had a moderate increase compared to the point wound experiment. Likewise, the circularity of the wound only increased by 3.6 percent for the circular wound, while it decreased by 25.2 percent for the point wound. Other parametric measures did not show a significant change.

Through an iterative process, the apical tension and permeability that yielded the same volume loss for ring 2 cells were obtained. The simulation was conducted for 400 seconds with an apical tension and permeability of 0.1*dyna/pixel*^{2} and 0.0024, respectively. The simulation and parametric measure results are shown in Figure 4.38 and Figure 4.39, respectively.

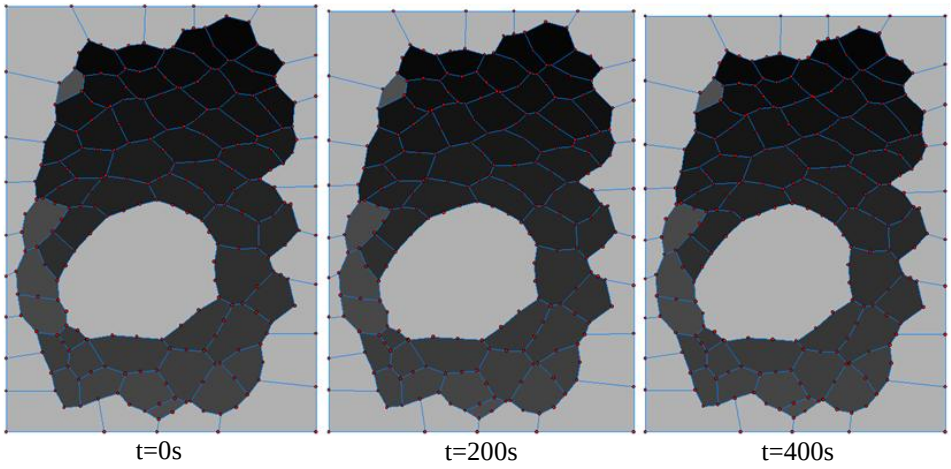

Figure 4.38 – Apical tension simulation

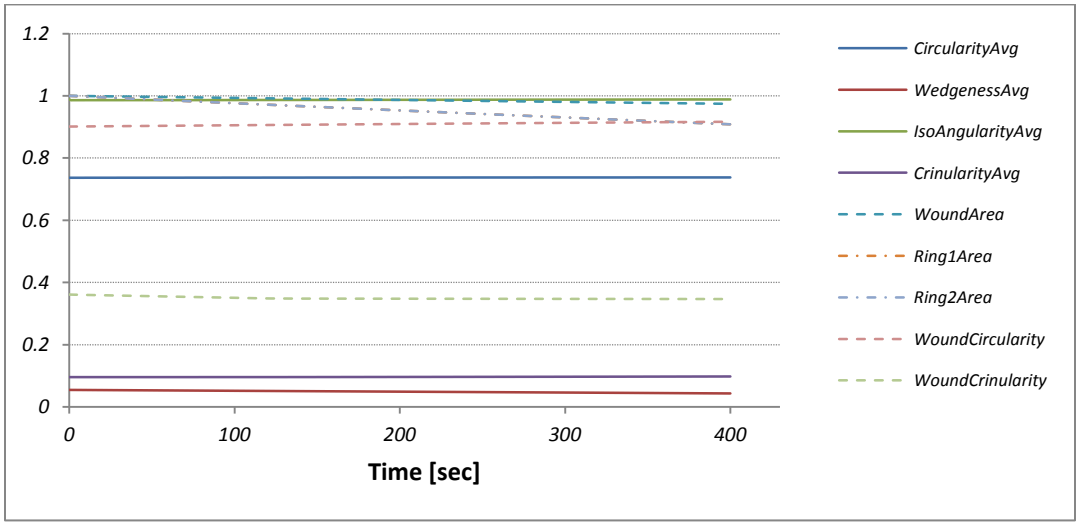

Figure 4.39 – Geometric parameters for a model tissue driven by apical tension

The simulation showed that the area of the entire patch was easily reduced using an apical tension. While reducing the area of the cells, its effect on other parametric measures was minimal. However, the apical tension did not prove to be a driving force for wound closure.

In the experimental data, the area of ring 1 cells decreased less than ring 2 cells, with losses being approximately 40% and 10% of their initial area, respectively. To achieve the same percentage area loss, the apical tension for ring 1 cells was required to be five times higher than ring 2 cells. Previous simulations demonstrated that the area of ring 1 cells could also be reduced by allowing cells to permeate fluid to neighbouring cells (refer to §4.1.4). To determine whether biasing the apical tension according to different cell types could drive wound closure, the apical tension in ring 1 cells was increased by five times. Unfortunately, the wound decreased by only three percent, suggesting that the apical tension was not a driving force, but rather a contributing factor to the attributes of the cell patch. Figure 4.40 shows the parametric results when ring 1 cells were biased towards having a higher area tension.

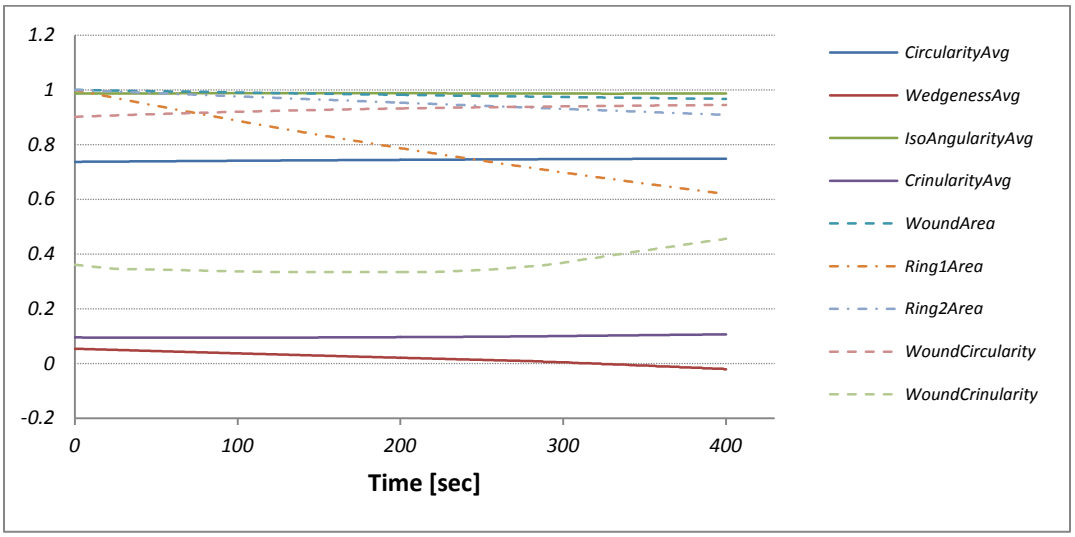

Figure 4.40 – Geometric parameters for a model tissue driven by apical tension. Ring 1 cells had an apical tension that was five times higher than ring 2 cells

4.5.2 Apical Tension with Edge Tensions and Native Dorsal Closure

Previous simulations suggested that the wound is able to close by applying a purse string around the wound or using native dorsal closure. Hence, a simulation was conducted with having a uniform apical tension in addition to a purse string around the wound using permeable cells. The simulation is shown in Figure 4.41 and the parametric measure results are shown in Figure 4.42. The forward simulation was conducted with the following parameters:

Edge tension around wound = 0.15dyne
Cell-to-Cell Permeability = 0.44
Apical Tension = 0.1dyne/pixel^2
Apical Permeability = 0.0024

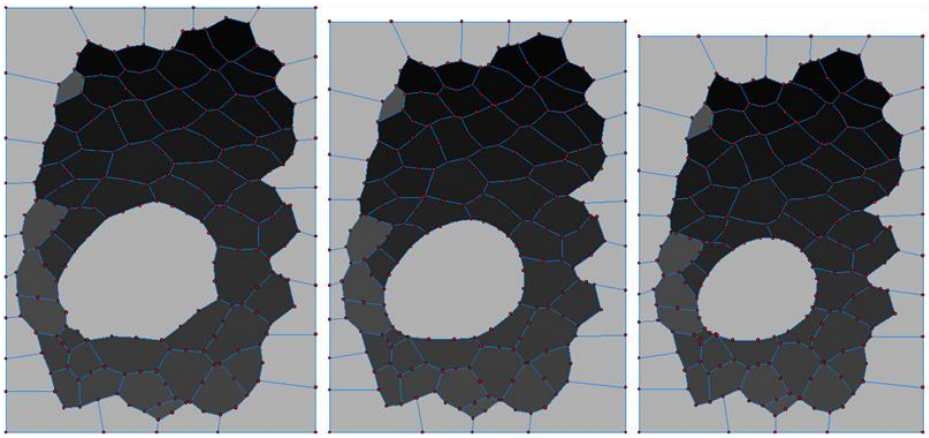

Figure 4.41 – Apical tension with purse string around the wound

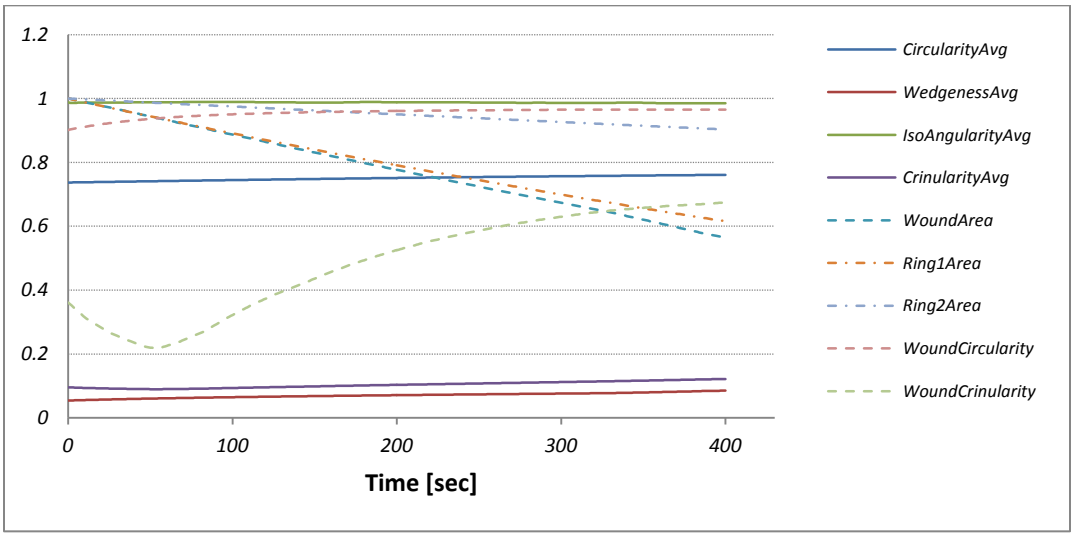

Figure 4.42 – Geometric parameters for a model tissue driven by apical tension and a purse string around the wound

The overall outcome of the simulation was similar to the experimental data. The main difference was in the wound crinularity, where it initially decreased, then increased; this was a recursive trend for cells rounding up (refer to §4.1.3). The combined effects of cell-to-cell and apical permeability allowed ring 1 cells to lose more volume than ring 2 cells. Although it was possible to lose more volume by applying a higher apical tension, an isotropic apical tension was used in conjunction with cell-to-cell permeability.

Knowing that the native dorsal closure was another possible driving force to wound healing, a simulation was conducted using native dorsal closure and apical tension. A forward simulation was conducted with a velocity boundary condition of -0.075 and -0.095*pixel/sec* for the x and y component, respectively. The simulation is shown in Figure 4.43 and the parameters measures are shown in Figure 4.44.

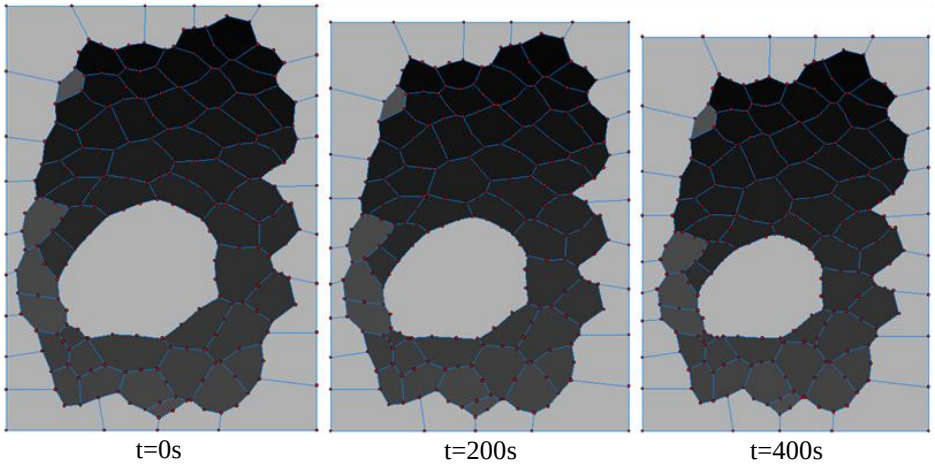

Figure 4.43 – Apical tension with native dorsal closure

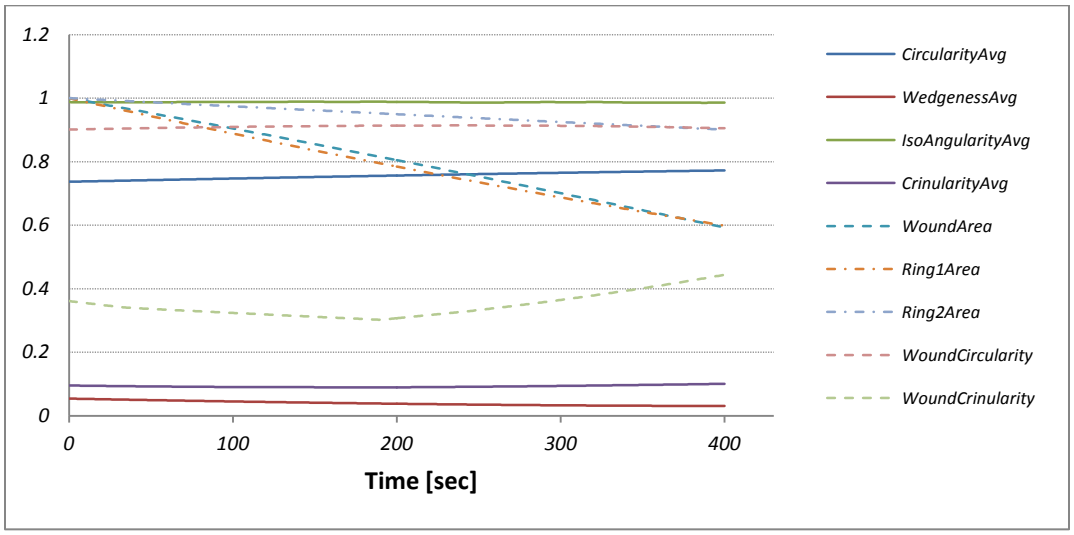

Figure 4.44 – Geometric parameters for a model tissue driven by apical tension and native dorsal closure

The results were similar to the previous simulation while the main differences were observed in the wound circularity and crinularity. The use of native dorsal closure prolonged the crinularity profile of the wound, decreasing half way into the simulation and then increasing. When comparing the simulation to the experimental data, the characteristics of the wound cell and the cell wedgeness were different (Figure 4.44 and Figure 4.37).

When a purse string was applied around the wound in addition to having native dorsal closure, a collaborative contribution to the parametric measures from both forces was observed. The purse string around the wound increased the circularity of the wound cell, while the velocity boundary condition reduced the crinularity of the wound. The parametric measures of the simulation are shown in Figure 4.45.

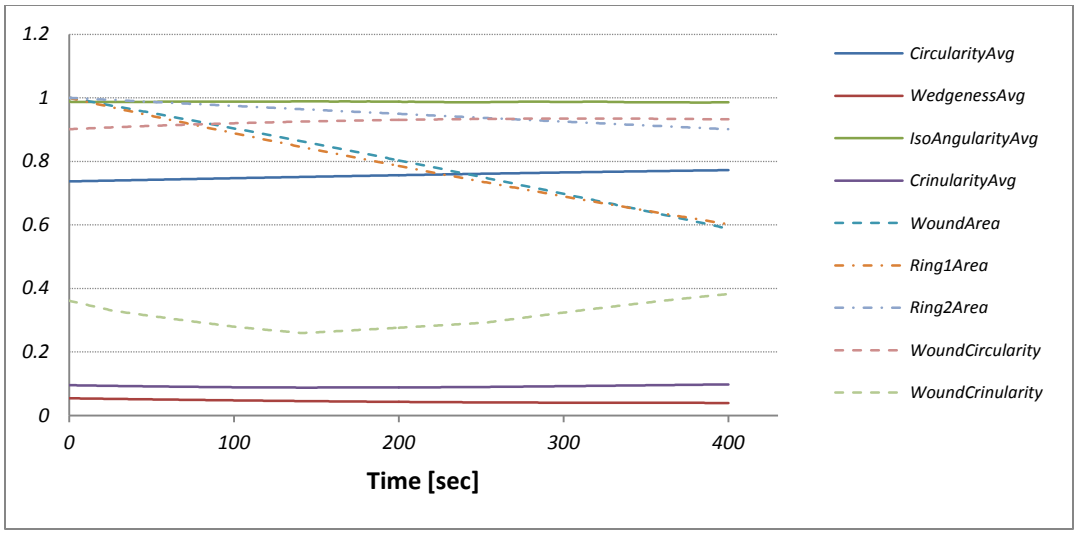

Figure 4.45 – Geometric parameters for a model tissue driven by apical tension, native dorsal closure and a purse string around the wound

There were differences in the rate the wound and ring 1 areas decreased, but observing the overall trend of the simulation with image sequences revealed similarities to the experimental data (Figure 4.37).

4.5.3 Apical Tension with Contractions

The simulation conducted with an apical tension and a purse string around the wound yielded similar results to the experimental data but was not able to capture the characteristics at a local level. To better capture the global and local behavior of the wound healing process, a forward simulation was conducted with the pressure-based local area contractions. The simulation was conducted for 400 seconds and the patch and parametric measure results are shown in Figure 4.46 and Figure 4.47, respectively. The following control parameters were used for the forward simulation:

Edge tension around wound = 0.75dyne
Volume Pressure = 10dyne/pixel^2
Apical Tension = 0.1 dyne/pixel^2
Velocity BC in x = 0.075pixel/sec
Velocity BC in y = 0.095pixel/sec
Contraction Rate = 0.05%
Contraction Strength = 0.5dyne/pixel^2
Contraction Duration = 100sec

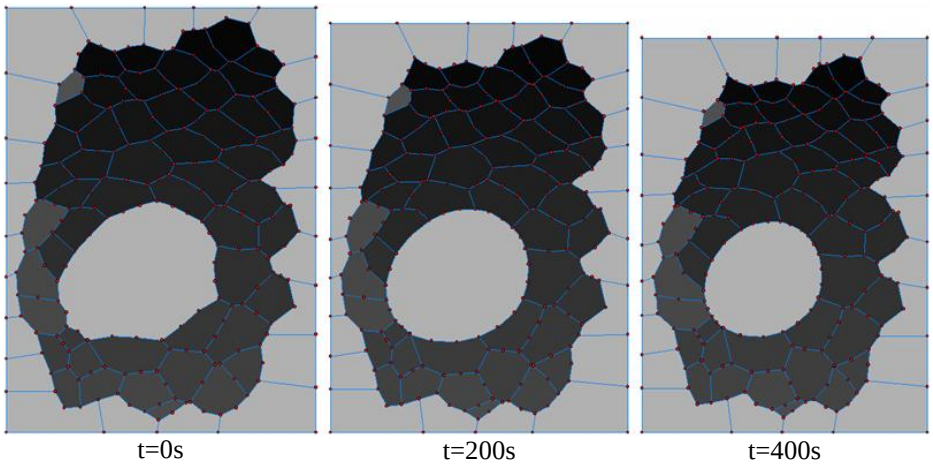

Figure 4.46 – Apical tension with native dorsal closure, edge tensions, and pressure-based contraction

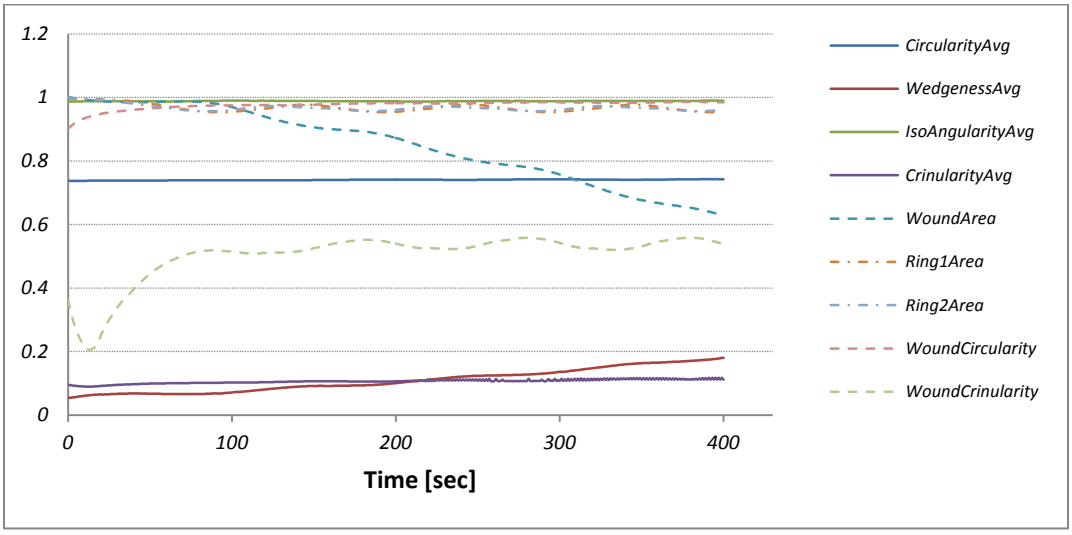

Figure 4.47 – Geometric parameters for a model tissue driven by apical tension, native dorsal closure, edge tensions, and pressure-based contraction

It was difficult to achieve results resembling the experimental data. Applying a purse string around the wound increased the circularity and crinularity of the wound. In addition, the ring 1 and ring 2 area profiles were not reflective of the experimental data because their loss in volume was minimal. Although the cells were permeable, the volume pressure of the cells had a dominant effect on the overall size of the cells, suggesting that the cells are reducible by increasing the apical tension. A simulation was conducted with an apical tension of 0.35 and 0.1$dyne/pixel^2$ for ring 1 and ring 2 cells, respectively, resulting in the final area of the ring 1 and ring 2 cells to be similar to the experimental data. The simulation is shown in Figure 4.48.

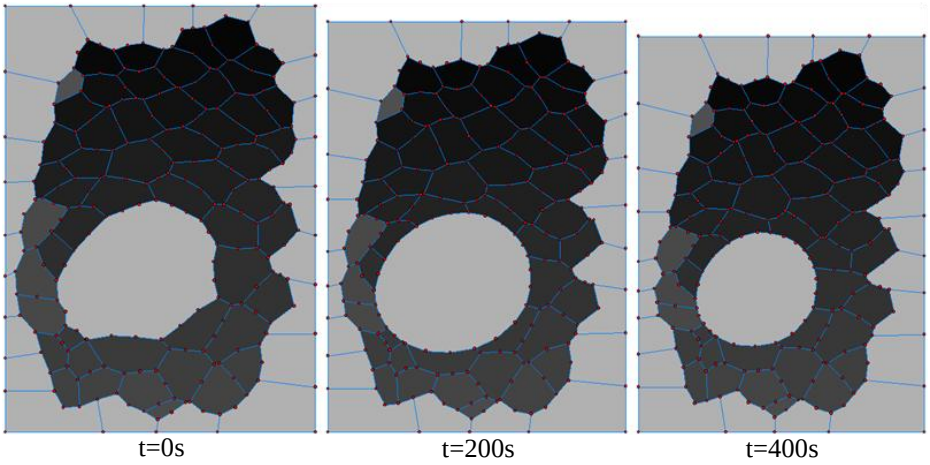

Figure 4.48 – High apical tension with native dorsal closure, edge tensions, and pressure-based local area contraction

The final configuration of the patch closely reflected the experimental data. Although the wound shape was circular, all other shapes in the patch were similar to the experimental data. Unfortunately, the parametric measures shown in Figure 4.49 did not resemble the experimental data.

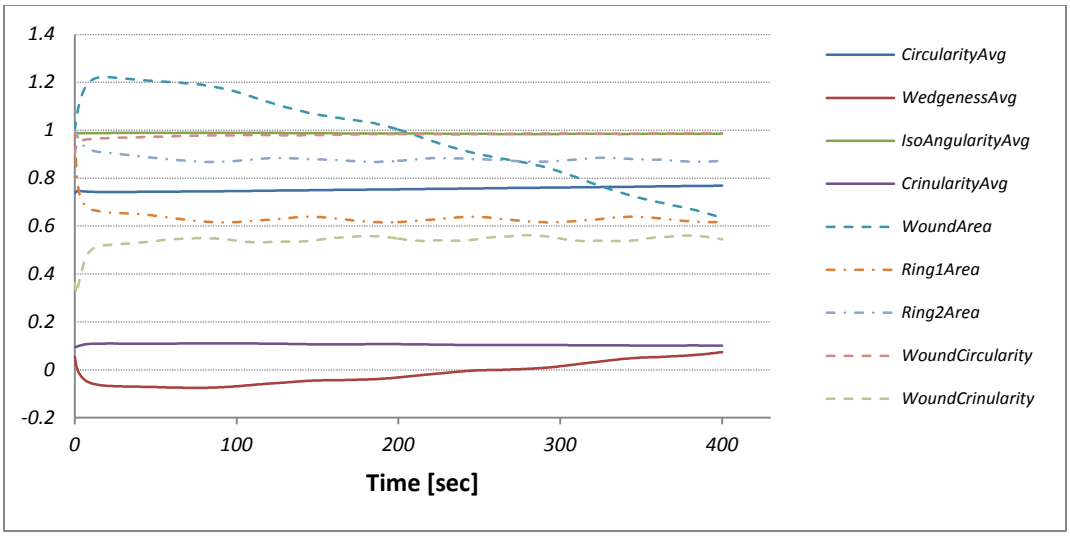

Figure 4.49 – Geometric parameters for a model tissue driven by high apical tension, native dorsal closure, edge tensions, and pressure-based contraction

Despite the final values of the parametric results being reflective of the experimental data, the process in which lesion closure was achieved was different. The area of the cells for the wound, ring 1 and ring 2 spiked to their respective values during the first few seconds of the simulation. Likewise, other parametric measures that depended on the area changes of cells spiked during the first few seconds into the simulation. The spikes in the parametric curves were a result of an anisotropic apical tension applied to the cell patch. This suggests that the apical tensions were increasing gradually as healing progressed.

4.5.4 Varying Apical Tension

The apical tension played an integral part to wound closure and it was by far the most effective way to reduce the area of the cells that were further away from the wound. Generally speaking, the leading edges of the patch moved at a constant pace (see Figure 3.13). However, for a given time frame, there were deviations from the linear fitted curve. Likewise, a pixilated analysis of the patch revealed that the boundary of the patch moved at an inconstant pace. Two points near the boundary of the patch for the Circular Wound 1 experiment were tracked and the displacement time history is shown in Figure 4.50.

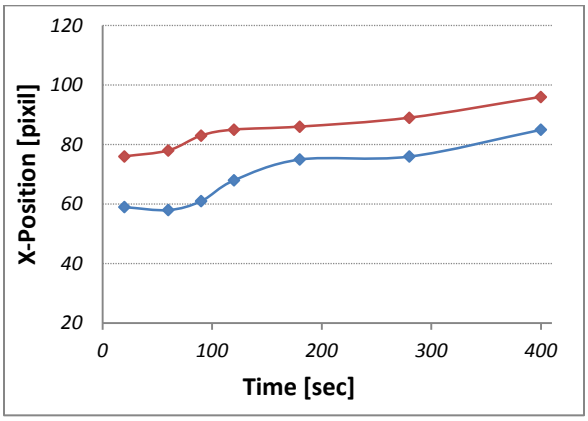

Figure 4.50 – Circular Wound 1 boundary displacement over time

The simulation was partitioned into two sections with 150*sec* being the reference point. A forward simulation was conducted with the velocity boundary condition of the patch being accurate to the experimental data. Through an iterative process, the control parameters were refined to reflect the experimental data, and the parameters used for the simulations are summarized in Table 4.5 and the parametric measure results are shown in Figure 4.51.

Table 4.5 – Parameters used for two step Circular Wound 1 simulation

Forces and Constraints	**Time [sec]**	
	0 to 150	**150 to 400**
Edge Tension in Patch [dyne]	*0.01*	*0.01*
Purse String around Wound [dyne]	*0.0*	*0.03*
Cell-to-Cell Permeability	*0.14*	*0.14*
Apical Tension [dyne/pixel^2]	*0.32*	*0.14*
Apical Permeability	*0.0024*	*0.0024*
Velocity Boundary Condition – VX [pixel/sec]	*-0.26*	*-0.08*
Velocity Boundary Condition – VY [pixel/sec]	*-0.19*	*-0.1*

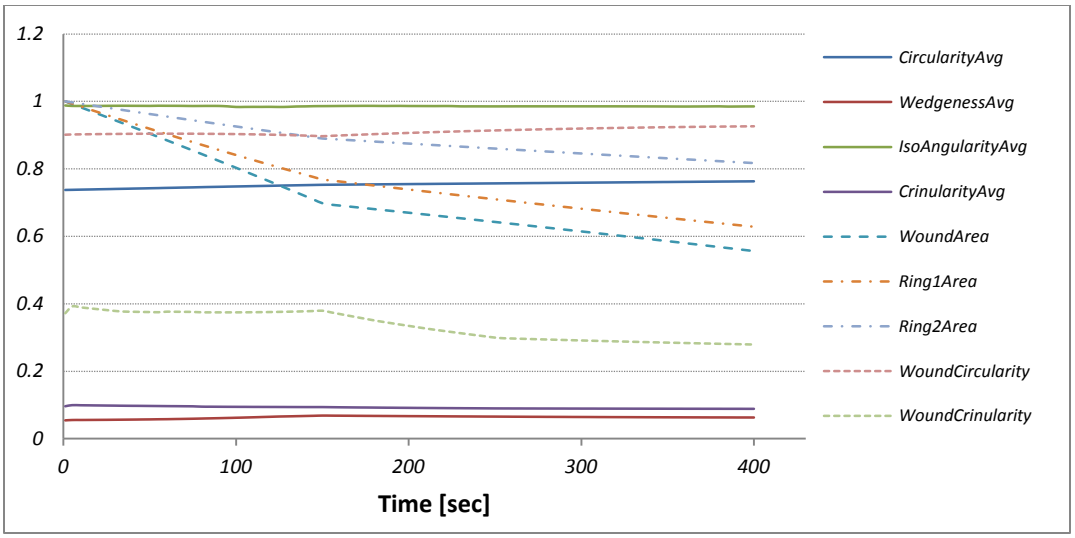

Figure 4.51 – Geometric parameters for a model tissue driven by varying apical tensions

Conducting the forward simulation in two stages captured the parametric measures more accurately than previous simulations. The characteristics of the wound cell resembled the experimental data, and although the final value of the wedgeness and the area of ring 2 cells were slightly lower than in the experimental data, the overall trend was reflective of the experimental data. Between the two steps, the velocity of the boundaries, apical tensions and purse string surrounding the wound were changed. The simulation demonstrated how a varying apical tension better reflected the experimental data. All things considered, the results conducted thus far indicated that the apical tension, native dorsal closure and purse string around the wound were the driving forces to wound healing.

4.6 Other Wound Healing Experiments

Section 4.5 showed that three main factors contributed to lesion closure: boundary motion, apical tension, and purse string tension. If these driving forces were reflective of the live experiments, perhaps it would be possible to replicate other types of wound healing experiments. In this section, three additional wound healing experiments were studied: Circular Wound 2, Line Wound 1 and Line Wound 2.

4.6.1 Circular Wound 2

The Circular Wound 2 experiment was similar to the Circular Wound 1 experiment. A circular shaped wound was initiated in the amnioserosa cells during the dorsal closure stage of embryo development. The wound cell was reduced and a significant amount of cell movements and shape changes were observed

during the healing progress, as shown in Figure 4.52. Through digitizing the image sequence, the parametric measures were obtained and are shown in Figure 4.53 for the duration of the process analyzed.

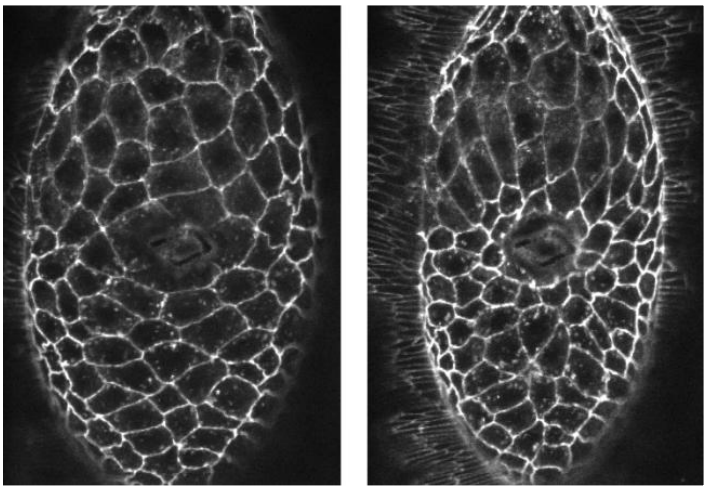

Figure 4.52 – Circular Wound 2 experiment

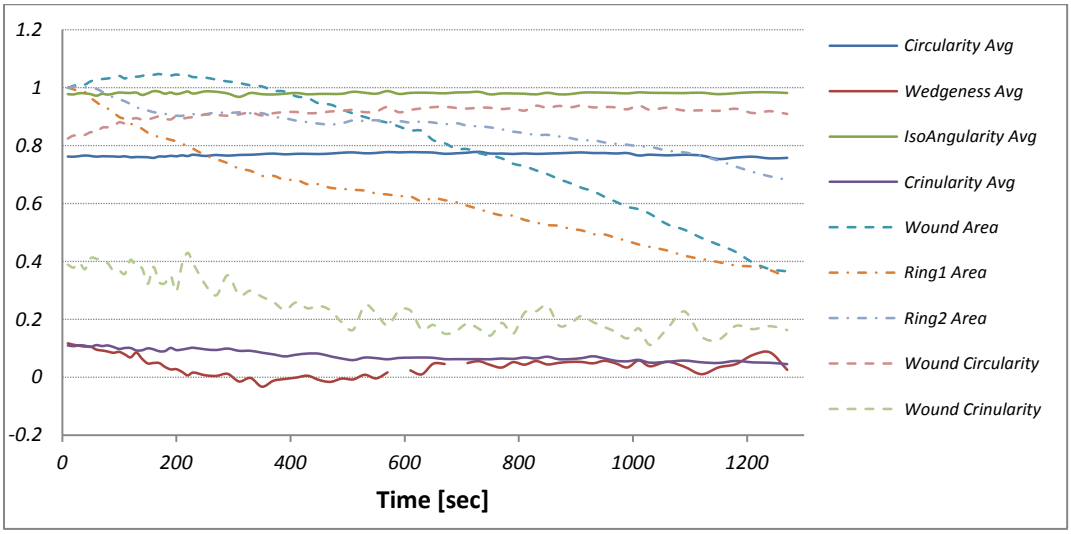

Figure 4.53 – Geometric parameters for Circular Wound 2 experimental data

The parametric measures showed that the area profile of the wound, ring 1 and ring 2 were not decreasing at a constant linear rate, suggesting that the apical tension was varying throughout the healing process. A closer analysis of the experimental data revealed the boundaries of the patch closing in at a constant pace. Through adjusting the magnitude of the apical tension, it was possible to obtain parametric results similar to the experimental data. Table 4.6 summarizes the control parameters used for the simulation and the parametric measure results are shown in Figure 4.54.

Table 4.6 – Parameters used for Circular Wound 2 simulation

Forces and Constraints	Time [sec]	
	0 to 200	200 to 1200
Edge Tension in Patch [dyne]	*0.01*	*0.01*
Purse String around Wound [dyne]	*0.0*	*0.0*
Cell-to-Cell Permeability	*0.14*	*0.14*
Apical Tension [dyne/pixel^2]	*0.13*	*0.108*
Apical Permeability	*0.0024*	*0.0024*
Velocity Boundary Condition – VX [pixel/sec]	*-0.072*	*-0.072*
Velocity Boundary Condition – VY [pixel/sec]	*-0.045*	*-0.045*

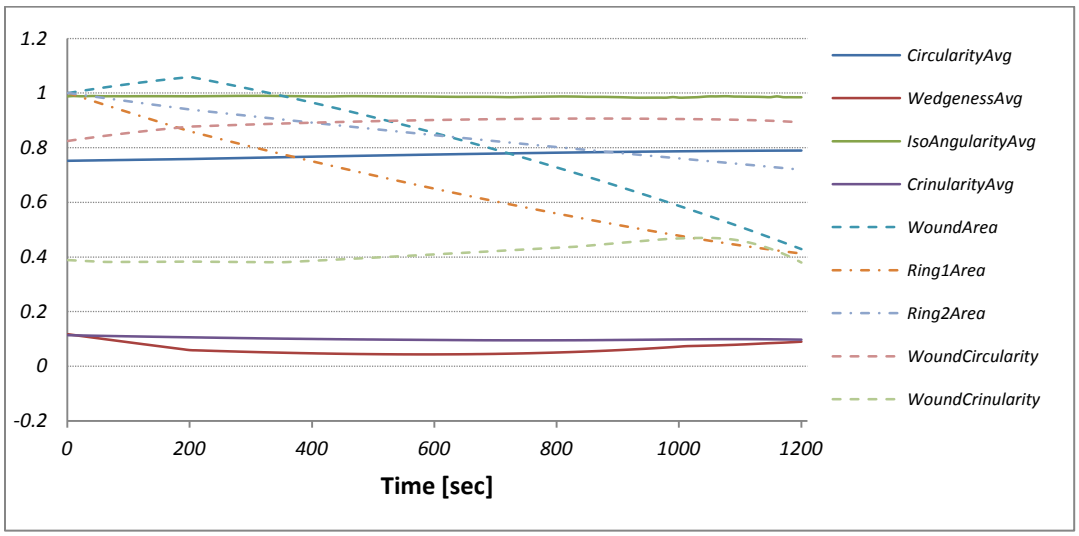

Figure 4.54 – Geometric parameters for a Circular Wound 2 model tissue driven by varying apical tensions and native dorsal closure

Through only adjusting the magnitude of the apical tension, it was possible to obtain results that reflected the experimental data. The Circular Wound 2 forward simulation demonstrated that an apical tension and native dorsal closure was sufficient to drive lesion closure.

4.6.2 Line Wound 1

The Line Wound 1 experiment was similar to the circular wound experiment in terms of the size of their wound. However, the shape of the wound was long and applied over a length of three to four cells. The initial and final configuration of the healing process is shown in Figure 4.55 and the parametric measures of the experimental data are shown in Figure 4.56.

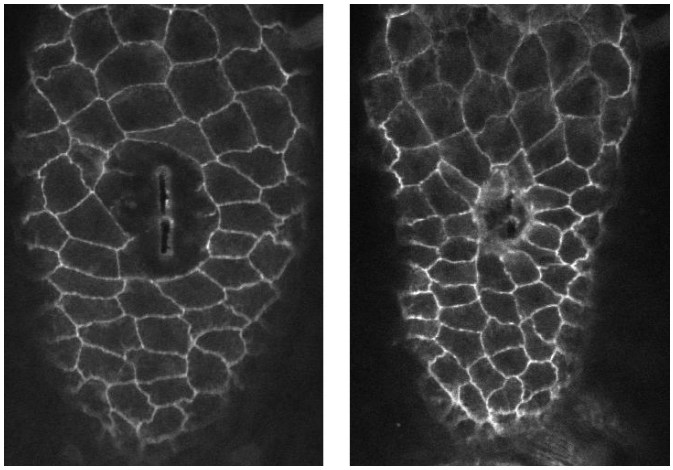

Figure 4.55 – Line Wound 1 experimental data experiment

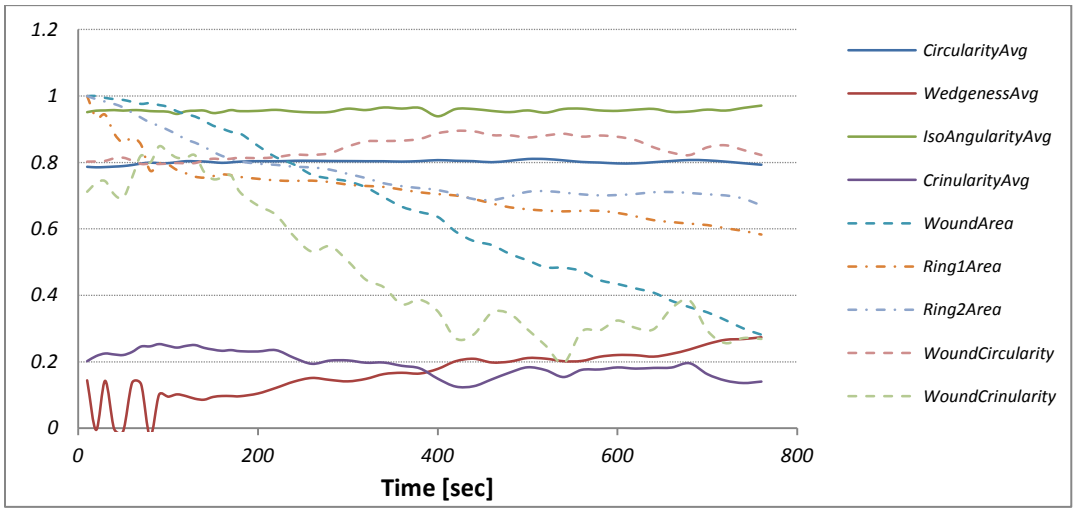

Figure 4.56 – Geometric parameters for Line Wound 1 experimental data

The parametric measures revealed that the area profile of ring 1 and ring 2 cells decreased at a similar pace. In addition, the wedgeness of the cells increased more than the circular wound experiments, suggesting that there may be a higher purse string around the wound. Analyzing the borders of the patch showed that the boundaries did not close in at a constant pace (see Figure 4.57).

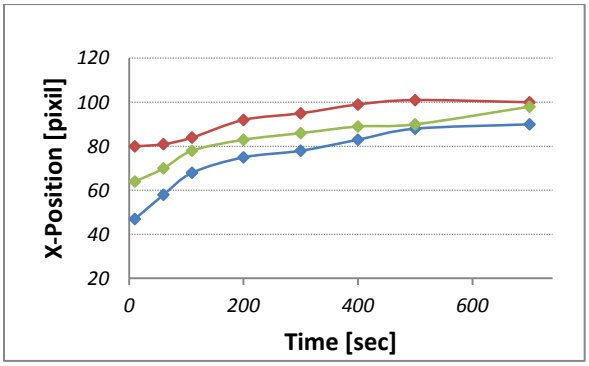

Figure 4.57 – Line Wound 1 boundary displacement over time

A vast range of forward simulations were conducted to determine the driving forces that were able to resemble the experimental data. Table 4.7 summarizes the control parameters used for the simulation and the parametric measure results are shown in Figure 4.58.

Table 4.7 – Parameters used for Line Wound 1 simulation

Forces and Constraints	Time [sec]	
	0 to 200	200 to 750
Edge Tension in Patch [dyne]	*0.01*	*0.01*
Purse String around Wound [dyne]	*0.03*	*0.03*
Cell-to-Cell Permeability	*0.051*	*0.051*
Apical Tension [dyne/pixel^2]	*0.31*	*0.11*
Apical Permeability	*0.0035*	*0.0035*
Velocity Boundary Condition – VX [pixel/sec]	*-0.23*	*-0.092*
Velocity Boundary Condition – VY [pixel/sec]	*-0.16*	*-0.072*

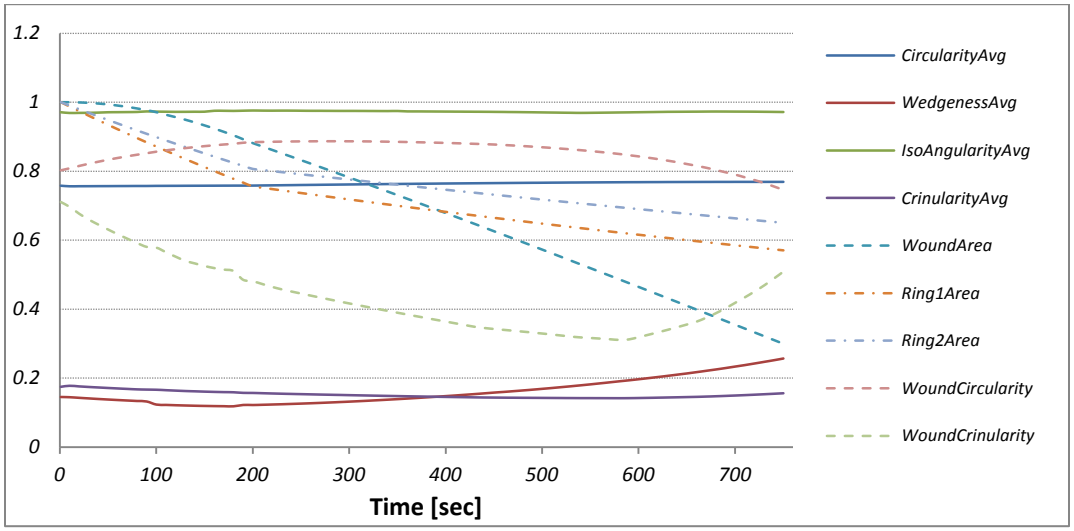

Figure 4.58 – Geometric parameters for a Line Wound 1 model tissue driven by varying apical tensions, native dorsal closure and a purse string around the wound

When an apical tension, native dorsal closure and a purse string around the wound were used as driving forces, the simulation closely reflected the experimental data. As expected, a purse string around the wound was required to increase the wedgeness of the cells, while the apical tensions and closing boundary conditions were important for modeling the slope of the parametric measures.

4.6.3 Line Wound 2

The Line Wound 2 experiment initiated wounds in four cells in a linear form. The initial and final configuration of the healing process is shown in Figure 4.59 and the parametric measure results of the experimental data are shown in Figure 4.60.

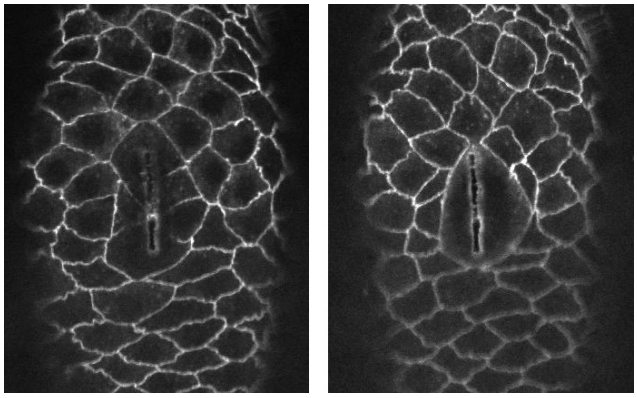

Figure 4.59 – Line Wound 2 experimental data experiment

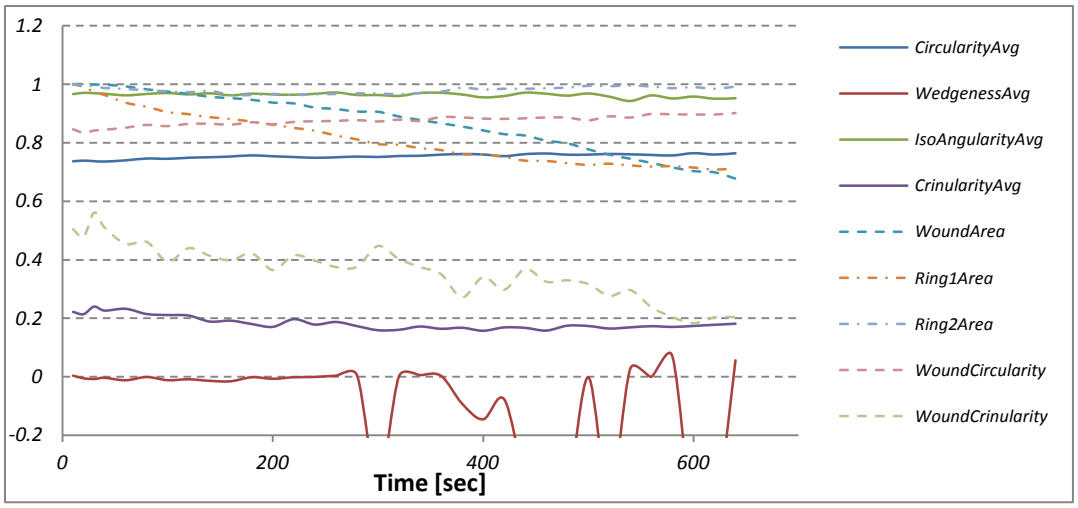

Figure 4.60 – Geometric parameters for Line Wound 2 experimental data

The ring 2 cells lost a small amount of volume during the healing process, suggesting that the gradient between the far-field stress and apical tension may have been small. The wedgeness was not a reliable quantitative measure for comparing results. Further analysis revealed that one of the cell edges was very short in length, resulting from a digitization error. Consequently, the calculation of the wedgeness, based on Eq. (3.2) was highly sensitive to the ratio of the edge lengths. In the simulation, a constant velocity boundary condition was used, based on the analysis conducted on the patch boundaries. Table 4.8 summarizes the control parameters used for the simulation and the parametric measure results are shown in Figure 4.61.

Table 4.8 – Parameters used for Line Wound 2 simulation

Forces and Constraints	**Time [sec]**	
	0 to 200	**200 to 750**
Edge Tension in Patch [dyne]	*0.01*	*0.01*
Purse String around Wound [dyne]	*0*	*0*
Cell-to-Cell Permeability	*0.06*	*0.06*
Apical Tension [dyne/pixel^2]	*0.34*	*0.27*
Apical Permeability	*0.0002*	*0.0002*
Velocity Boundary Condition – VX [pixel/sec]	*-0.035*	*-0.035*
Velocity Boundary Condition – VY [pixel/sec]	*-0.015*	*-0.015*

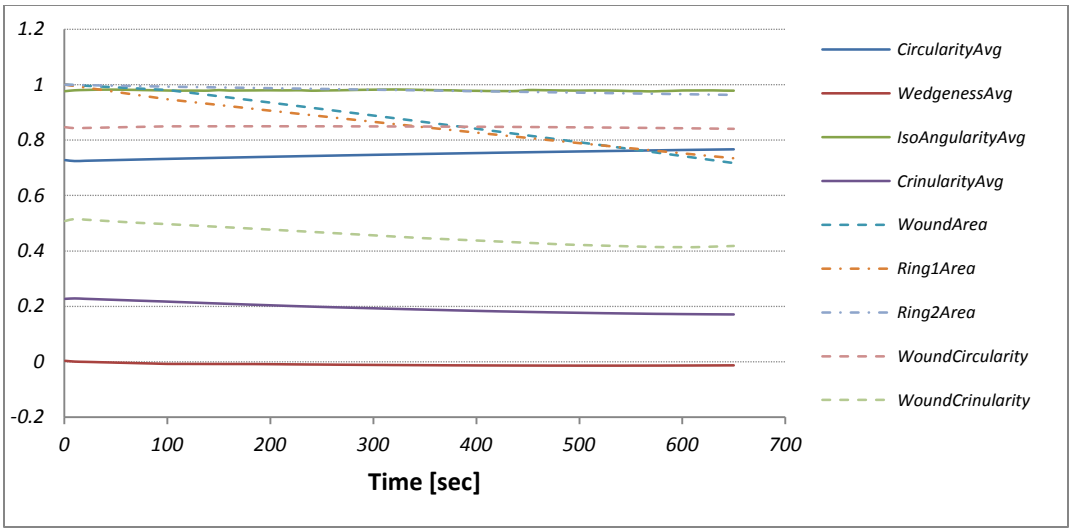

Figure 4.61 – Geometric parameters for a Line Wound 2 model tissue driven by varying apical tensions and native dorsal closure

When the velocity boundary condition and apical tensions were used as driving forces, the simulation resembled the experimental data results. The wedgeness of the cells showed little change in the experimental data, not requiring a purse string around the wound for the simulation.

When considering the simulations conducted in this chapter, the result revealed that there were three main driving forces responsible for wound healing: far-field boundary motion, apical tension, and purse string tension around the wound. Although a purse string was not required for simulating Circular Wound 2 and Line Wound 2 experiments, other simulations showed that the presence of a purse string was an integral part of capturing the characteristics of the healing process. Furthermore, the simulation result suggests that the apical tensions were changing, rather than remaining constant, throughout the healing process.

4.7 Summary

In summary, the simulations demonstrated that interfacial tensions had a tendency to roundup the cells. Observing the individual cell edges of the experimental data revealed cells having jagged edges, suggesting that the edge tensions were less than in our initial models. When a high purse string was applied around the wound, the wound was able to close (see §4.1.3). Applying a purse string around the wound forced the wound to become circular and it increased the wedgeness of the cells bordering the wound. The ring 1 cells in the experimental data had a wedged shape; hence, a purse string around the wound was deemed a viable driving force.

Two different contraction models were developed and implemented to evaluate their contribution to wound healing (see §4.2). The nodal-based contraction model proved to be an unreliable model. It caused the shape of the cells to change in irregular ways, whereas the pressure-based contraction model yielded results resembling the experimental data. As part of the contraction model, the volume pressure constraint was used to allow the cells to expand after they contracted. Consequently, the volume pressure prevented the cells from losing their volume, despite the use of cell-to-cell permeability; the volume changes in cells were dominated by pressure rather than the cell-to-cell permeability. The simulations showed that the pressure-based cell contraction was not a driving force, but rather, contributed to the attributes of the cells' behavior (see §4.2.5).

Simulated stretching of the lateral epidermis confirmed that it resists dorsal closure and wound healing (see §4.3.1). Ablation experiments revealed that the far-field stress existed throughout the healing process. Despite the resisting presence of the far-field stress, wound healing could be accomplished by applying a sufficiently high purse string around the wound (see §4.3.2). For an applied far-field stress of $0.001 dyne/pixel^2$, the purse string around the wound had to be increased by 50% to achieve the same amount of wound closure as compared to a scenario without a far-field stress. Although it is possible to achieve lesion closure through applying a higher purse string around the wound, the wound cell rounded up and insufficient volume was lost in ring 1 cells.

Driving the edges of the patch proved to be more than sufficient to drive lesion closure (see §4.4). It yielded results similar to when a purse string was applied around the wound cell, except the wound shape was jagged. The wound cell also had jagged edges in the experimental data. Although the native dorsal closure was sufficient to drive wound closure, it was difficult to initiate fluid loss for ring 1 cells. However, the characteristics of the wound were achievable through proper balancing of the edge motions and a purse string around the wound.

Apical tension was not able to drive wound closure, but played a key role in the volume loss in cells (see §4.5). The Circular Wound 1 experimental data indicated a higher loss in volume for ring 1 cells than ring 2 cells. Cell-to-cell permeability may be used, or apical tensions may be increased, to induce fluid loss in cells. In either case, simulation results demonstrated that both means of fluid loss for ring 1 cells did not affect other parametric measures.

When the apical tension model was used with native dorsal closure and a purse string, it was possible to approximately replicate all parametric measures obtained from the experimental data (see §4.5.2). A closer examination of the experimental data revealed that the boundary closed in at an inconsistent pace. As a result, decomposing the simulation into two sections helped achieve results that were closely reflective of the experimental data (see §4.5.4). Analyzing other wound healing experiments by sections resulted in parametric measures closely resembling the experimental data. In all the simulations, the use of far-field motions, apical tension and purse string were sufficient to achieve lesion closure (see §4.6).

Table 4.9 and Table 4.10 summarizes the parameters that gave the best fits to the various experiments. It is clear that the parameters varied somewhat from one test to another within the same type of wound

and that they varied to about the same degree from one wound type to another. This suggests that the observed variability may be largely due to animal-to-animal differences and not to systematic differences associated with wound type or data fitting.

Table 4.9 – Summary of parameters used for simulation (early time steps)

	Wound Experiment:	**Point**	**Circular 1**	**Circular 2**	**Line 1**	**Line 2**
	Time [sec]:	0 to 200	0 to 150	0 to 200	0 to 200	0 to 200
Forces and Constraints	*Edge Tension in Patch [dyne]*	*0*	*0.01*	*0.01*	*0.01*	*0.01*
	Purse String around Wound [dyne]	*0.03*	*0*	*0*	*0.03*	*0*
	Cell-to-Cell Permeability	*10*	*0.14*	*0.14*	*0.051*	*0.06*
	Apical Tension [dyne/pixel^2]	*0*	*0.32*	*0.13*	*0.31*	*0.34*
	Apical Permeability	*0*	*0.0024*	*0.0024*	*0.0035*	*0.0002*
	Velocity Boundary Condition – VX [pixel/sec]	*-0.034*	*-0.26*	*-0.072*	*-0.23*	*-0.035*
	Velocity Boundary Condition – VY [pixel/sec]	*-0.0068*	*-0.19*	*-0.045*	*-0.16*	*-0.015*

Table 4.10 – Summary of parameters used for simulation (later time steps)

	Wound Experiment:	**Point**	**Circular 1**	**Circular 2**	**Line 1**	**Line 2**
	Time [sec]:	200 to 850	150 to 400	200 to 400	200 to 750	200 to 750
Forces and Constraints	*Edge Tension in Patch [dyne]*	*0*	*0.01*	*0.01*	*0.01*	*0.01*
	Purse String around Wound [dyne]	*0.03*	*0.03*	*0*	*0.03*	*0*
	Cell-to-Cell Permeability	*10*	*0.14*	*0.14*	*0.051*	*0.06*
	Apical Tension [dyne/pixel^2]	*0*	*0.14*	*0.108*	*0.11*	*0.27*
	Apical Permeability	*0*	*0.0024*	*0.0024*	*0.0035*	*0.0002*
	Velocity Boundary Condition – VX [pixel/sec]	*-0.034*	*-0.08*	*-0.072*	*-0.092*	*-0.035*
	Velocity Boundary Condition – VY [pixel/sec]	*-0.0068*	*-0.1*	*-0.045*	*-0.072*	*-0.015*

These findings also explain why VFM calculations based on the assumption that wound healing was driven exclusively by edge forces and intracellular pressures did not give convincing results. Indeed, it is reassuring that VFM did not produce good results when it was missing far-field stresses (or corresponding boundary motions) and apical tensions, drivers that these simulations indicate are crucial to wound closure.

Chapter 5
Conclusions and Recommendations

This study has shown the following:

1) It was possible to use cell-level models to investigate the mechanics of wound healing.
2) Of the five parametric measures developed to characterize cells, area, wedgeness and crinularity provided the best discrimination when different sets of driving forces were active. Circularity and isoangularity might be useful for comparing two individual cells, but ensemble averages changed little.
3) Interfacial tensions and intracellular pressures by themselves were not able to match the motions and parameters of experiments. This is the apparent reason that initial attempts to apply VFM failed.
4) When area tensions and far-field stresses act in combination with interfacial tensions, good agreement can be obtained.
5) The combinations of driving forces required to match multiple experiments of the same type show some variability.
6) A similar degree of variability was found between wounds having point, circle and line geometries.

One recommendation for future work is to obtain measures of the material properties of cells so that results can be reported in dimensional form. Another recommendation is to obtain better quality images and digitize the entire period of the healing process. The digitized images capture the early portions of the healing process, while the later portions were difficult to digitize due to the quality of the images. Being able to obtain the later portions of the healing process may provide insights into the contribution of the purse string formation and protrusions of any filopodia or lamellipodia. In addition, it would be beneficial to model the entire amnioserosa and perhaps its surrounding tissue.

Finally, it would be interesting to apply a version of VFM that assumed all of the kinds of driving forces identified here as being important. Would it be able to correctly determine the forces present in these tissues? If it could, it would be a highly valuable tool for mapping the forces that drive wound closure and other related morphogenetic movements.

Forward and inverse techniques for modeling morphogenetic movements possess much potential. They are not necessarily limited to a particular problem, but in principle could provide insights into many kinds of morphogenetic movements and thereby ultimately contribute to medicine and human quality of life.

References

Anon, E., Serra-Picamal, X., Hersen, P., Gauthier, N. C., Sheetz, M. P., Trepat, X., & Ladoux, B. (2012). Cell crawling mediates collective cell migration to close undamaged epithelial gaps. *Proceedings of the National Academy of Sciences of the United States of America, 109*(27), 10891-10896. doi: 10.1073/pnas.1117814109

Arrkas, N. (1994). *Biomechanics of active movement and division of cells*. Berlin ; New York: Springer-Verlag.

Belacortu, Y., & Paricio, N. (2011). Drosophila as a model of wound healing and tissue regeneration in vertebrates. *Developmental Dynamics : An Official Publication of the American Association of Anatomists, 240*(11), 2379-2404. doi: 10.1002/dvdy.22753; 10.1002/dvdy.22753

Beloussov, L. V. (1998). *The dynamic architecture of a developing organism*. Dordrecht: Kluwer Academic Publishers.

Beucher, S., & Meyer, F. (1992). Chapter 12: The morphological approach to segmentation: The watershed transformation. In E. R. Dougherty (Ed.), *Mathematical morphology in image processing* (pp. 433-481). New York: Marcel Dekker, Inc.

Brock, J., Midwinter, K., Lewis, J., & Martin, P. (1996). Healing of incisional wounds in the embryonic chick wing bud: Characterization of the actin purse-string and demonstration of a requirement for rho activation. *The Journal of Cell Biology, 135*(4), 1097-1107.

Brodland, G. W. (2002). The differential interfacial tension hypothesis (DITH): A comprehensive theory for the self-rearrangement of embryonic cells and tissues. *Journal of Biomechanical Engineering, 124*(2), 188-197.

Brodland, G. W., Chen, D. I., & Veldhuis, J. H. (2006). A cell-based constitutive model for embryonic epithelia and other planar aggregates of biological cells. *International Journal of Plasticity, 22*(6), 965-995.

Brodland, G. W., & Chen, H. H. (2000). The mechanics of cell sorting and envelopment. *Journal of Biomechanics, 33*(7), 845-851.

Brodland, G. W., Chen, X., Lee, P., & Marsden, M. (2010a). From genes to neural tube defects (NTDs): Insights from multiscale computational modeling. *HFSP Journal, 4*(3-4), 142-152. doi: 10.2976/1.3338713

Brodland, G. W., Conte, V., Cranston, P. G., Veldhuis, J., Narasimhan, S., Hutson, M. S., . . . Miodownik, M. (2010b). Video force microscopy reveals the mechanics of ventral furrow invagination in drosophila. *Proceedings of the National Academy of Sciences of the United States of America, 107*(51), 22111-22116. doi: 10.1073/pnas.1006591107

Brodland, G. W., Viens, D., & Veldhuis, J. H. (2007). A new cell-based FE model for the mechanics of embryonic epithelia. *Computer Methods in Biomechanics and Biomedical Engineering, 10*(2), 121-128.

Campos-Ortéga, J. A., & Hartenstein, V. (Eds.). (1997). *The embryonic development of drosophila melanogaster*

Chen, X., & Brodland, G. W. (2008). Multi-scale finite element modeling allows the mechanics of amphibian neurulation to be elucidated. *Physical Biology, 5*(1), 015003 (15pp).

Clausi, D. A., & Brodland, G. W. (1993). Mechanical evaluation of theories of neurulation using computer simulations. *Development, 118*, 1013-1023.

Conte, V., Ulrich, F., Baum, B., Munoz, J., Veldhuis, J. H., Brodland, G. W., & Miodownik, M. (2012). A biomechanical analysis of ventral furrow formation in the drosophila melanogaster embryo. *PloS One, 7*(4), e34473. doi: 10.1371/journal.pone.0034473

Coughlin, M. F., & Stamenovic, D. (1997). A tensegrity structure with buckling compression elements: Application to cell mechanics. *Journal of Applied Mechanics-Transactions of the Asme, 64*(3), 480-486.

Cowin, S. C., & Doty, S. B. (2006). *Tissue mechanics*. New York: Springer.

Cranston, P. G. (2009). *An inverse finite element approach for identifying forces in biological tissues.* (Master of Applied Science in Civil Engineering, University of Waterloo. Department of Civil Engineering.).

Dai, J. W., TingBeall, H. P., & Sheetz, M. P. (1997). The secretion-coupled endocytosis correlates with membrane tension changes in RBL 2H3 cells. *Journal of General Physiology, 110*(1), 1-10.

Davidson, L. A., Koehl, M. A. R., Keller, R., & Oster, G. F. (1995). How do sea-urchins invaginate - using biomechanics to distinguish between mechanisms of primary invagination. *Development, 121*(7), 2005-2018.

Davidson, L. A., Oster, G. F., Keller, R. E., & Koehl, M. A. (1999). Measurements of mechanical properties of the blastula wall reveal which hypothesized mechanisms of primary invagination are physically plausible in the sea urchin strongylocentrotus purpuratus. *Developmental Biology, 209*(2), 221-238. doi: 10.1006/dbio.1999.9249

Ethier, C. R., & Simmons, C. A. (2007). *Introductory biomechanics : From cells to organisms*. Cambridge ; New York: Cambridge University Press.

Galko, M. J., & Krasnow, M. A. (2004). Cellular and genetic analysis of wound healing in drosophila larvae. *PLoS Biology, 2*(8), E239. doi: 10.1371/journal.pbio.0020239

Goodwin, B. C., & Trainor, L. E. H. (1985). Tip and whorl morphogenesis in acetabularia by calcium-regulated strain fields. *Journal of Theoretical Biology, 117*(1, pp. 79-106), November. doi: 10.1016/S0022-5193(85)80165-X

Harris, A. K. (1976). Is cell sorting caused by differences in the work of intercellular adhesion? A critique of the steinberg hypothesis. *Journal of Theoretical Biology, 61*(2, pp. 267-285), September. doi: 10.1016/0022-5193(76)90019-9

Hutson, M. S., Brodland, G. W., Yang, J., & Viens, D. (2008). Cell sorting in three dimensions: Topology, fluctuations, and fluidlike instabilities. *Physical Review Letters, 101*(14), 148105.

Hutson, M. S., Tokutake, Y., Chang, M. S., Bloor, J. W., Venakides, S., Kiehart, D. P., & Edwards, G. S. (2003). Forces for morphogenesis investigated with laser microsurgery and quantitative modeling. *Science, 300*(5616), 145-149. doi: 10.1126/science.1079552

Hutson, M. S., Veldhuis, J. H., Ma, X., Lynch, H. E., Cranston, P. G., & Brodland, G. W. (2009). Combining laser microsurgery and finite element modeling to assess cell-level epithelial mechanics [Abstract]. *Biophysical Journal, 97*(12) 3075-3085.

Ingber, D. E. (1993). Cellular tensegrity - defining new rules of biological design that govern the cytoskeleton. *Journal of Cell Science, 104*, 613-627.

Ingber, D. E. (1997). Tensegrity: The architectural basis of cellular mechanotransduction. *Annual Review of Physiology, 59*, 575-599.

Jacinto, A., & Martin, P. (2001). Morphogenesis: Unravelling the cell biology of hole closure. *Current Biology : CB, 11*(17), R705-7.

Jacinto, A., Wood, W., Woolner, S., Hiley, C., Turner, L., Wilson, C., . . . Martin, P. (2002). Dynamic analysis of actin cable function during drosophila dorsal closure. *Current Biology, 12*(14), 1245-1250.

Kaltschmidt, J. A., Lawrence, N., Morel, V., Balayo, T., Fernández, B. G., Pelissier, A., . . . Martinez Arias, A. (2002). Planar polarity and actin dynamics in the epidermis of drosophila. *Nature Cell Biology, 4*(12), 937-944.

Kiehart, D. P., Galbraith, C. G., Edwards, K. A., Rickoll, W. L., & Montague, R. A. (2000). Multiple forces contribute to cell sheet morphogenesis for dorsal closure in drosophila. *The Journal of Cell Biology, 149*(2), 471-490.

Lay, D. C. (2003). *Linear algebra and its applications* Pearson Learning Solutions.

Leptin, M. (1999). Gastrulation in drosophila: The logic and the cellular mechanisms. *The EMBO Journal, 18*(12), 3187-3192. doi: 10.1093/emboj/18.12.3187

Logan, D. L. (2011). *First course in finite element method, si* (5th Ed ed.). Mason, OH: South-Western, Cengage Learning.

Martin, P., & Lewis, J. (1992). Actin cables and epidermal movement in embryonic wound healing.*360*, 179.

Mitchison, J. M., & Swann, M. M. (1954). The mechanical properties of the cell surface .1. the cell elastimeter. *Journal of Experimental Biology, 31*(3), 443-&.

Morris, C. E., & Homann, U. (2001). Cell surface area regulation and membrane tension. *The Journal of Membrane Biology, 179*(2), 79-102.

Nash, J. C. (1990). *Compact numerical methods for computers: Linear algebra and function minimisation* Adam Hilger.

Nuri Akkaş. (1994). *Biomechanics of active movement and division of cells* Springer-Verlag.

Odell, G. M., Oster, G., Alberch, P., & Burnside, B. (1981). The mechanical basis of morphogenesis: 1. epithelial folding and invagination. *Developmental Biology, 85*, 446-462.

Peralta, X. G., Toyama, Y., Kiehart, D. P., & Edwards, G. S. (2008). Emergent properties during dorsal closure in drosophila morphogenesis. *Physical Biology, 5*(1), 015004. doi: 10.1088/1478-3975/5/1/015004

Ramet, M., Lanot, R., Zachary, D., & Manfruelli, P. (2002). JNK signaling pathway is required for efficient wound healing in drosophila. *Developmental Biology, 241*(1), 145-156. doi: 10.1006/dbio.2001.0502

Redd, M. J., Cooper, L., Wood, W., Stramer, B., & Martin, P. (2004). Wound healing and inflammation: Embryos reveal the way to perfect repair. *Philosophical Transactions of the Royal Society of London.Series B, Biological Sciences, 359*(1445), 777-784. doi: 10.1098/rstb.2004.1466

Scuderi, A., & Letsou, A. (2005). Amnioserosa is required for dorsal closure in drosophila. *Developmental Dynamics : An Official Publication of the American Association of Anatomists, 232*(3), 791-800. doi: 10.1002/dvdy.20306

Spring, K. R., & Ericson, A. C. (1982). Epithelial cell volume modulation and regulation. *The Journal of Membrane Biology, 69*(3), 167-176.

Stark, G. D. (1977). *Spina bifida : Problems and management*. Oxford : Philadelphia: Blackwell Scientific Publications ; distributed by J. B. Lippincott.

Steinberg, M. S. (1962). On the mechanism of tissue reconstruction by dissociated cells, I: Population kinetics differential adhesiveness, and the absence of directed migration. *Zoology, 48*, 1577-1582.

Steinberg, M. S. (1970). Does differential adhesion govern self-assembly process in histogenesis? equilibrium configurations and the emergence of a hierarchy among populations of embryonic cells. *Journal of Experimental Zoology, 173*, 395-434.

Steinberg, M. S. (1978). Cell-cell recognition in multicellular assembly: Levels of specificity.*32*, 25.

Thompson, D. W. (1942). *On growth and form* (New ed ed.). Cambridge, [Cambridgeshire]: Cambridge University Press.

Townes, P., & Holtfreter, J. (1955). Directed movements and selective adhesion of embryonic amphibian cells. *Journal of Experimental Zoology, 128*(1, pp. 53-120), February. doi: 10.1002/jez.1401280105

Wang, S., Tsarouhas, V., Xylourgidis, N., Sabri, N., Tiklova, K., Nautiyal, N., . . . Samakovlis, C. (2009). The tyrosine kinase stitcher activates grainy head and epidermal wound healing in drosophila. *Nature Cell Biology, 11*(7), 890-895. doi: 10.1038/ncb1898

Wilson, H. V. (1907). On some phenomena of coalescence and regeneration in sponges. *Journal of Experimental Zoology, 5*(2, pp. 245-258), December. doi: 10.1002/jez.1400050204

Wood, W., Jacinto, A., Grose, R., Woolner, S., Gale, J., Wilson, C., & Martin, P. (2002). Wound healing recapitulates morphogenesis in drosophila embryos. *Nature Cell Biology, 4*(11), 907-912. doi: 10.1038/ncb875